Thesis presented for the degree of

DOCTOR OF PHILOSOPHY

in the Department of Chemical Engineering

UNIVERSITY OF CAPE TOWN

A Theoretical View on Deactivation of Cobalt-Based Fischer-Tropsch Catalysts

Jurie Christiaan Wessels Swart

November 2008

Abstract

This work considers deactivation mechanisms of cobalt-based Fischer Tropsch synthesis catalysts at a fundamental level. Small cobalt crystallites are used as catalysts on industrial scale to produce diesel and wax from natural gas. Nano-sized crystallites provide a maximum activity per mass of catalyst. The stability of these nano-clusters is affected by the contribution of the additional energy of surface atoms. The role of size in deactivation mechanisms such as sintering and oxidation was studied at the hand of size dependent thermodynamics. Sintering is expected to be fast for crystallites below 9.3 nm due to the reduction of the melting temperature. Only crystallites below 2.1 nm are susceptible to oxidation, thus oxidation would not have a major contribution to catalyst deactivation. Carbon is always present on the catalyst surface and can diffuse easily across the surface. When hydrogen is not present, carbon deposits can easily be formed on flat cobalt (111) surfaces. Carbon sheets were found to have a chemical interaction with the surface. The interaction strength of a sheet is determined by the number of carbon atoms in the sheet, therefore large sheets would be more difficult to remove. A quantum mechanical DFT (Density Functional Theory) approach was used to investigate these aspects and a surface energy correction was shown to be necessary for the determination of accurate quantitative surface energies.

Synopsis

The Fischer-Tropsch process provides fuel and chemicals from carbon based resources other than oil. A mixture of H_2 and CO is converted to hydrocarbons and water over a transition metal catalyst. Cobalt is an ideal catalyst for the production of diesel and paraffinic wax from natural gas derived feedstocks at remote locations. However, the relative high cost of cobalt requires a high activity and a long catalyst life time. A high catalytic activity in cobalt-based Fischer-Tropsch catalysts is typically obtained by utilization of highly dispersed cobalt on a support. This work aims to give some insight in the mechanisms governing the deactivation of cobalt-based Fischer-Tropsch catalysts with a particular focus on possible deactivation by sintering, oxidation and the formation of a carbon overlayer.

The thermodynamic behaviour of nano-sized crystallites is different from the bulk material due to the large fraction of low coordinated surface atoms present. Due to the presence of surface atoms the excess energy of the surface was estimated using DFT (Density Functional Theory). The surface energies of flat metal surfaces and metal nano-rods were calculated to determine the excess energy as a function of the coordination number of a surface atom. A linear relationship between the excess energy of surface atoms and their coordination number was established after correction of the surface energy obtained by DFT. The intrinsic surface energy error correction is necessary due to the inadequacy of the current level of DFT to predict the extension of the wave function into the vacuum. The coordination number

dependent excess energy in combination with the van Hardeveld and Hartog statistics for nano-crystallites was used to determine the size dependent surface energies for FCC-cobalt nano-crystallites.

The excess energy of surface atoms with a low coordination number contributes substantially to the chemical potential of small crystallites. Hence, a lower melting temperature will be obtained with smaller crystallites. As a consequence, sintering by coalescence of adjacent metal crystallites is significantly enhanced for smaller crystallites. Sintering via ripening via an atomic intermediate is unlikely due to the low partial pressure of atomic cobalt, whereas cobalt carbonyls are not stable under Fischer-Tropsch conditions.

At large per pass conversions, high water partial pressures are prevalent at the reactor outlet. High H_2O/H_2 ratios could lead to oxidation of metallic cobalt to CoO. Although this is not feasible for bulk cobalt under realistic Fischer-Tropsch conditions, earlier calculations (based on classical calculation of the surface energy) suggested that it might be feasible. The surface energy of CoO(100) was determined using DFT+U. The resulting energy can be calculated using a classical model, if both the contribution of the electro-static interaction and the covalent bonding within CoO is taken into account. This could have been anticipated based on the partial charge on the ions within CoO. The size dependent oxidation behaviour was investigated for the worst case scenario, i.e. with cubical crystallites of metallic cobalt and CoO. It was found that only metal crystallites with a diameter below 2.1 nm would be at risk of oxidation. This is much lower than the size of 4.5 nm previously suggested in literature. Oxidation can thus be discarded as a major deactivation mechanism, since cobalt crystallites in the Fischer-Tropsch catalysts are typically much larger.

Carbon deposition was studied on ideal FCC-Co(111) surfaces. Different carbon species on the surface showed that carbon become more stable when

clusters are formed. The cluster stability increases with cluster size. The formation of long carbon chains on the surface seems to be slightly favoured over the formation of branched structures. Large aromatic clusters, which can be formed upon combining long chains, were found to be very stable. The driving force for the formation of carbon deposits and overlayers is purely due to thermodynamics. Carbon deposits and overlayers will form, if an excess of carbon on the surface is present on the surface, especially in the absence of other adatoms such as hydrogen.

The interaction of graphene (a single sheet of carbon) with the surface was investigated using DFT. The charge analysis and DOS analysis of the adsorbed structure showed that the sheet is chemically bound to the surface. The adsorption energy was determined taking into account the evanescent nature of the wave function into the vacuum. The adsorption energy is rather low if expressed per carbon atom (ca. 4.11 *kJ/mol carbon*), but this is a substantial when considering a sheet of e.g. 70 carbon atoms (covering 35 metal atoms) which would have an adsorption energy of 280 *kJ/mol* per carbon cluster. For a cluster of this size, the mobility would be very low due to a high sliding barrier and the barrier for a concerted lifting is high. It is postulated that large carbon clusters would not be mobile and consequently block the surface.

Contents

List of Figures

List of Tables

Part I

Scope of study

Chapter 1

Introduction

1.1 The Fischer-Tropsch process

1.1.1 Context of the Fischer-Tropsch process

The Fischer-Tropsch synthesis is the conversion for synthesis gas (a mixture of H_2 and CO) from coal or natural gas derived feedstock yielding hydrocarbons [1]. The Fischer-Tropsch synthesis can be used as an alternative route to the production of gasoline, diesel, chemicals and wax from carbon sources other than crude oil [2] (see outline of the process in Figure 1.1). A schematic (see Figure 1.1) shows the possible flow schemes of a coal or natural gas derived process for the production of fuel and chemicals.

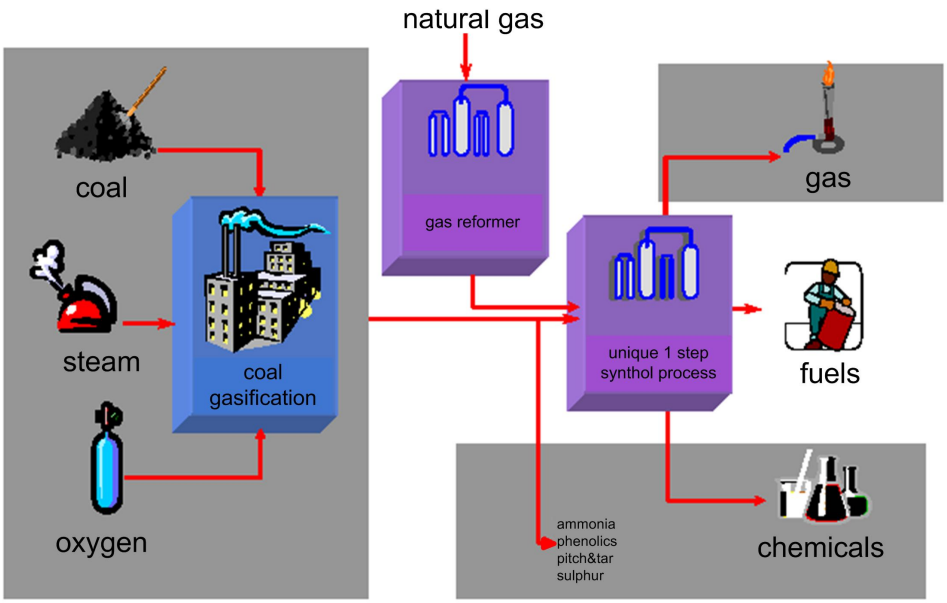

Figure 1.1: Simple flow sheet of a coal or natural gas based Fischer-Tropsch process (adapted from www.sasol.com).

For new installations, production of synthetic fuels can be economically viable at a crude oil price above 23 $/barrel [2, 3] given the availability of cheap feedstocks and catalysts. In the light of energy saving policies and CO_2 emissions, flaring of natural gas has been charged with taxes [4] and can instead be converted to easily transportable liquid hydrocarbons or wax.

Sasol has developed advanced reactor technologies for high and low temperature operation [3, 5, 6, 7]. These units can be tailored for the production of gasoline, diesel, chemicals and wax. The high temperature operation (300-350 °C) is generally characterized by the production of lighter unsaturated hydrocarbons suited for the production of gasoline and chemicals [3]. The low temperature operation (200-240 °C) on the other hand is characterized by the production of long chain hydrocarbons and wax which can be hydro-cracked to produce diesel of exceptional quality [6, 7].

The catalyst of choice is influenced by various factors related to the carbon feedstock, location, mode of operation and the desired products. These four factors are interlinked and must be considered carefully in the design of an optimal Fischer-Tropsch process.

1.1.2 Fundamental work on the Fischer-Tropsch synthesis

Since the discovery of the Fischer-Tropsch synthesis in the 1920's most of the work related to the understanding and improvement of the catalysts was based on empirical knowledge gained from trial and error experiments [1]. Improvements in the activity and selectivity originated from a vast amount of experimental work on activation procedures along with support and promoter effects. If the underlying chemistry which governs the activity of the catalyst is not understood, trial and error experiments will always be necessary. A deep understanding of the fundamentals would enable the design and improvement of catalysts at a fundamental level and consequently save time, effort and money. With the advances in theoretical models and computational power, the catalytic process can be studied fundamentally at a quantum mechanical level to gain a fundamental understanding.

Theoretical methods such as molecular mechanics, molecular dynamics and quantum mechanics traditionally provided qualitative information on the catalytic processes. Of these methods, quantum mechanics is the most

powerful since it is able to provide insight into the formation and breaking of bonds. Modern quantum software packages can even treat surfaces and surface reactions at quantum level although most of the information is still qualitative. Improved theoretical models and corrective procedures can provide quantitative information when interpreted carefully. This fundamental understanding of the chemistry involved in catalytic reactions for a range of metals and reactions can be used to design optimal catalysts. The ability to predict catalyst activity based on chemical composition, molecular structure and morphology forms the basis of theoretical research in catalysis [8].

1.1.3 The catalytic cycle and elementary steps

The Fischer-Tropsch reaction can be generalized as

$$2H_2 + CO \rightleftharpoons (-CH_2-) + H_2O. \tag{1.1}$$

On a molar basis, water is the main by-product to the Fischer-Tropsch process and for every mole CO converted, a mole of water is typically formed. The linear paraffinic hydrocarbons, olefins, branched hydrocarbons and oxygenates are readily formed depending on the catalyst and operating conditions. The reactor will always be filled with synthesis gas, water and a wide range of hydrocarbons.

In the field of homogeneous catalysis, a catalytic cycle is commonly used to describe a mechanism in terms of the intermediates formed. The catalytic cycle contains the elementary steps in which intermediates are converted to form the final product. These fundamental processes also form the basis of heterogeneous chemical reactions. The same approach can be used in heterogeneous catalysis, but is usually more complicated since multiple parallel pathways can exist to form the same product. A mechanism for the Fischer-Tropsch process on Ru was proposed using a catalytic cycle [9]. These

elementary steps consist of the following processes: adsorption onto the surface, decomposition of adsorbed molecules, diffusion of adsorbed species across the surface, recombination and finally desorption. The Sabatier principle (see [8]) states that the rate of a catalytic reaction is maximized at an optimum interaction strength between adsorbed species and the surface. This means that too strong or too weak adsorption of reactants would reduce the rate of the reaction. The cyclic nature of catalytic reactions is important since the continuous process would not be possible if one of the intermediates in such a cycle can not be formed or converted.

The Fischer-Tropsch synthesis is unique in that the monomers H_2 and CO are used to produce hydrocarbon molecules with any number of carbon atoms. The hydrocarbon products contain a selection of saturated, unsaturated, branched and oxygenated hydrocarbons. The selectivities to the different product types are controlled by the catalyst metal, catalyst promoters and operating conditions to name a few [1]. Since a wide range of products are produced from the same starting molecules, the mechanism must include intermediates common for different products. Due to the complexity and variety of the Fischer-Tropsch products a fairly intricate network of reaction pathways can be imagined. The probability of one pathway being preferred over another would affect the selectivity of the process. The elementary steps such as adsorption, diffusion and recombination can be studied in detail using quantum mechanical methods such as DFT (Density Functional Theory). Consequently the relative energy profile for different reaction pathways can be calculated to gain insight into the mechanistic pathways and activation energies. This information can then be used to understand the parameters controlling selectivity.

Hydrogen adsorption on clean surfaces can be calculated routinely as done for Fe [10] and Ru [11]. Hydrogen adsorption is fairly weak and is not generally considered to be one of the limiting steps of the Fischer-Tropsch

cycle. Simple models based on the metal d-band properties and work function were proposed to describe the strength of interaction between hydrogen and different metals [12].

CO adsorption is significantly stronger than hydrogen adsorption. The electronic interactions at play during adsorption and dissociation are quite well understood at a fundamental level [13]. Similar to hydrogen adsorption, d-band models were also proposed to describe the adsorption interaction of CO with metal surfaces [14]. The adsorption and dissociation of CO have been studied extensively using DFT on various transition state metals [15, 16] although this specific interaction pushes the limits of the underlying theory of DFT calculations (see Chapter 2).

The formation of C–H and C–C bonds is understood fairly well at a qualitative level [17, 18]. These aspects have also been covered extensively from a DFT perspective [9, 19]. Although a lot of accurate information is available to calculate relative energies, some work on developing the models is still needed before the calculated energies are accurate enough to derive credible *ab-initio* rate constants. Nevertheless a lot can be learned from current DFT calculations about the aspects which affect activity, selectivity and stability of catalysts.

A Fischer-Tropsch catalyst requires a surface which can break a CO bond and create C–C and C–H bonds. Some of the transition state metals which show Fischer-Tropsch activity are Fe, Co, Ni and Ru [1, 20]. Van Santen and Neurock [8] suggested that metals which form strong metal carbon bonds will have a high selectivity toward long-chain hydrocarbons. This can be seen from the increasing wax selectivities for Ni-, Co- and Ru-based catalysts. In the case of iron, the metal carbon bond is very strong resulting in the formation of carbides at Fischer-Tropsch conditions. The Sabatier principle states that the maximum rate can be achieved for an optimal interaction between the surface and intermediates. Co- and Ru-based catalysts seem to

be ideal for the production of paraffinic wax since these metals have high chain growth probabilities compared to Ni-based catalysts [1].

1.2 Cobalt as a Fischer-Tropsch catalyst

Various transition state metals show catalytic activity for the Fischer-Tropsch synthesis [20] of which Ni, Fe, Co and Ru-based catalysts are the best studied [1]. The relatively high cost of Ru to other metals, along with the limited availability, rules out the use of Ru-based catalysts for operation on a commercial scale [5]. Ni-based catalysts produce methane with too high a selectivity for a viable commercial installation [5].

Given the high cost of syngas production [21], it is important to use the syngas as efficiently as possible by making use of recycle loops. The optimum hydrocarbon production is typically found for H_2/CO ratios close to usage ratio. If the fresh feed syngas has a H_2/CO ratio below the usage ratio, the recycle loop will become hydrogen poor which can be detrimental to the catalyst. In the case of cobalt catalysts, the theoretical usage ratio is close to 2 due to the production of paraffinic wax. For iron-based catalysts, the usage ratio is lower due to additional H_2 formation from the water gas shift reaction. Methane derived feedstocks typically have a large H_2/CO ratio, while coal derived feedstocks are hydrogen-poor and require hydrogen addition. For a coal derived Fischer-Tropsch process, iron would typically be the preferred catalyst, while cobalt would be preferred for natural gas derived feedstocks.

Water is one of the main products of the Fischer-Tropsch synthesis and consequently the H_2O/H_2 ratio increases along the length of the reactor as hydrogen is consumed and water formed. When considering the thermodynamics of oxidation, large H_2O/H_2 ratios may result in the metal being oxidized. At H_2O/H_2 ratios prevalent of reactor exit conditions, bulk cobalt is not likely to oxidize [22]. For iron-based catalysts Fe_3O_4 is usually found

in the spent catalysts, suggesting that iron-based catalysts are not stable against oxidation at large H_2O/H_2 ratios [23]. Consequently a higher per pass conversion can be achieved for cobalt-based catalyst since a the bulk catalyst is resistant to oxidation at outlet H_2O/H_2 ratios.

Furthermore, cobalt-based catalysts have been shown to have no water inhibition term in the rate expression [5, 6, 24]. For iron-based catalysts, the rate is reduced at high partial pressures of water [5]. The Fischer-Tropsch activity and low risk of oxidation at the outlet conditions allows economical operation at large per pass conversions for cobalt-based catalysts [6, 25].

Iron-based catalysts have been used successfully since 1950 for high temperature operation at Sasol [5] and are ideal for the production of gasoline and chemicals [3]. High wax and diesel selectivities can be obtained when using a cobalt-based catalyst [4, 25]. A high quality straight run diesel and diesel cracked from cobalt-based Fischer-Tropsch wax can be produced where there are very tight constraints on diesel quality or as blending stock to upgrade lower quality diesel [5]. When the selectivity consideration for the production of wax and diesel is a key factor, the cobalt-based catalyst can provide these selectivities.

Catalyst breakage and subsequent deactivation of Fe-based catalysts require continuous catalyst replacement [3, 5]. The short catalyst lifespan is not ideal for operation at remote locations where the cost of catalyst supply and disposal would be significant.

Given these considerations cobalt-based catalysts are preferred for the production of fuel from natural gas at remote locations.

1.3 Catalyst activity

Previously some of the elementary steps required for the Fischer-Tropsch synthesis to take place were highlighted. Each of these elementary steps requires a specific environment with suitable geometric and electronic prop-

erties to facilitate bond breaking and bond formation between C, O and H species on the surface. Although different metals have the same crystal structure, a difference in the number of valence electrons results in different energies associated with bond breaking and bond formation on a similar geometry [19, 15]. A possible explanation for this effect was given by Hammer [26] where the activity for CO dissociation was related to the center of the *d*-band and the Fermi level. The Fermi level is the solid state metallic version of the HOMO (Highest Occupied Molecular Orbital) which can interact with the LUMO (Lowest Unoccupied Molecular Orbital) of an adsorbing molecule [18]. The adsorption strength of a molecule on the surface is determined by the interaction of electrons from the adsorbing molecule with the electrons of the surface. The electronic states and filling of the orbitals will determine whether and how the adsorbing molecule will interact with the surface. The electronic environment on the metal surface affects the magnitude of the energy barriers for the elementary steps such as bond breaking and formation.

On a given metal such as Ru [9, 27], Co [28, 29], Pt [30], Rh and Pd [19], the activation energies for elementary steps have been shown to depend on the local geometry. The elementary steps on a given metal surface can take place over different geometric pathways. For CO dissociation on a close packed surface the energetic cost for breaking the bond is higher when the oxygen atom moves over the top of a metal than over the bridge site [28]. Consequently the activation energy for the CO dissociation over the bridge site should be faster than dissociation over the top site. On a stepped or corrugated surface, however, the geometry is different compared to that of a flat surface. Atoms on stepped or corrugated surfaces have a lower coordination and more broken bonds than flat surface atoms. The adsorbed molecules will bind stronger to surface atoms with a low coordination than surface atoms with a high coordination since surface atoms with a low co-

ordination have more broken bonds which have to be saturated. This is demonstrated by the CO dissociation energy at these low coordination step sites which is lower than on the higher coordination flat surface sites [28].

Therefore the geometric environment or ensemble of surface atoms form a site for an elementary step to take place. Different sites (with a combination of high or low coordination surface atoms) thus have different abilities to enable an elementary step to take place. Ge [28] suggested that CO dissociation would be spontaneous over the Co($10\bar{1}2$) and Co($11\bar{2}4$) surfaces, while the Co(0001) and Co($11\bar{2}0$) surfaces would have an endothermic barrier relative to gas phase CO.

The elementary steps such as C–C and C–H coupling do not necessarily require the same site as CO dissociation to take place. Since the metal-carbon and metal-hydrogen interactions are different, the C–C and C–H coupling would prefer different geometries. The relative ease of C–C and C–H coupling would affect the selectivities observed for Fischer-Tropsch products over various metals.

As stated by the Sabatier principle, an optimum interaction is desired. This statement suggests that a balance is required between all the elementary steps. If C–H coupling is much more preferred than C–C coupling, methane formation would be preferred over chain growth. It is well known that at Fischer-Tropsch conditions Ni-based catalysts produce methane with high selectivities, while cobalt-based catalysts are more selective toward heavy hydrocarbons and wax [1]. The ideal catalyst therefore requires the availability of the correct number of sites, which have optimum interactions with intermediate species.

1.3.1 Structural aspects affecting the intrinsic activity

The intrinsic activity of a catalyst is the ability of the surface to catalyse the reaction without any mass transfer limitations. The observed intrinsic

activity can usually be measured as the reaction rate per number of surface atoms. The way in which the surface atoms are geometrically arranged will determine whether active sites for different elementary steps are available. The actual intrinsic activity is thus the maximum catalytic potential of the surface. Changes in the surface geometry resulting from bulk phase changes or surface reconstruction will affect this intrinsic activity potential of the catalyst. Until recently most computational work only focused on ideal flat surfaces. Lately the focus has shifted to investigate the effects of steps and low coordinated surface atoms as well [9, 19, 28, 29].

The observed intrinsic activity will be affected by changes in the chemical environment and by availability of the lowest energy pathways. The availability of the lowest energy pathways can be influenced by coverage effects from adsorbed molecules. Some pathways can be blocked by too high a coverage of reaction intermediates or competitive adsorption of gas molecules not taking part in the reaction. Poisoning of the surface where strongly adsorbing immobile species stick to the surface can also prevent the elementary steps from taking place.

If the species populating the surface do not affect the surrounding chemical environment on the surface, the actual intrinsic activity potential will not be affected. In the presence of highly electronegative surface species like sulfur, the electronic properties of neighbouring surface atoms will be affected and the actual intrinsic potential will be reduced (or enhanced in the case of chemical promoters) [31].

1.3.2 Surface reconstruction

Changes in the geometry due to surface reconstruction change the chemical environment and thus also the ability to catalyse the elementary steps. Surface relaxation or reconstruction can occur on a clean surface or as a result of strongly adsorbing species [32]. Atomic scale restructuring was found on

HCP cobalt when placing the clean surface in a syngas environment [33]. This STM work suggests that the flat surface is transformed to a surface with many islands. The reason for this is currently not well understood.

Recent work on cobalt [34] suggests that low coverages of adsorbed carbon can reconstruct the close packed FCC(111) to a more open FCC(100) surface. The explanation is that the strong adsorption of carbon stabilizes the surface energy of the FCC(100) surface more than the FCC(111) surface. These surfaces can reconstruct even further to the so called "clock-reconstruction". This reconstruction is fast since the atomic displacements are short and the reconstruction is thermodynamically favoured. Since alkyl species do not induce the surface reconstruction [34], hydrogenation of the adsorbed carbon in the reconstructed surface will result in a reconstruction of the modified surface to the original state. The actual catalyst surface therefore does not have to be a stationary surface and transient changes in the surface structure are possible.

There is evidence in the Fischer-Tropsch literature that the intrinsic activity for Fe [35, 36] and Co [21, 37] based catalysts change over time. This construction of the "Fischer-Tropsch regime" is a result of changes in the surface structure, geometry and consequently the chemical environment on the surface. Since these processes are very intricate and difficult to probe experimentally even under model conditions, it is currently not very well understood. For oxide systems, however, (DFT) *ab-initio* thermodynamics has proved to be a useful tool in unraveling the surface structure as a function of the gas phase composition, temperature and pressure [38, 39, 40, 41].

The effects of surface reconstruction on the intrinsic activity have not been studied in detail but will eventually be necessary for a complete understanding of the Fischer-Tropsch synthesis.

1.3.3 Bulk phase changes

The intrinsic activity is a function of the exposed surface and is related to the bulk phase unless significant surface reconstruction takes place. Different crystal structures would expose unique lowest energy surfaces. As mentioned earlier, cobalt can either be found in a FCC or HCP phase depending on the size and temperature. The FCC(111) and HCP(0001) surfaces are the same to a depth of two layers. Other surface cuts differ significantly and therefore have different intrinsic activities. This is an example of a bulk phase change where the chemical composition stays the same but the crystal structure changes.

In a bulk phase change, a metal can also be transformed to a metal oxide, carbide, nitride and sulfide to name a few types. These interstitial phases have a significant effect on the catalytic properties of the catalyst since the surface geometries and the electronic properties at the surface change. Typically, metal bonding is not considered to be ionic since there is no charge transfer between the metal atoms in the crystal structure. For oxide phases, however, charge transfer can take place from the metal to the oxygen, resulting in an effective charge being formed. The ionic component of the bonding must thus be included as well. This change in electronic properties at the surface for metal and oxide surfaces has a significant effect on the catalytic ability of the surface.

The formation of carbides affects the bulk crystal structure and consequently the activity of the surface. Carbide phases are not considered to be ionic, but nevertheless would have an effect on the surface electronic properties as can be seen from the difference in work function of carbides [42] and metals [43]. The activity of cobalt carbide was found to be very low, suggesting that the carbide phase is not active for the Fischer-Tropsch synthesis [44].

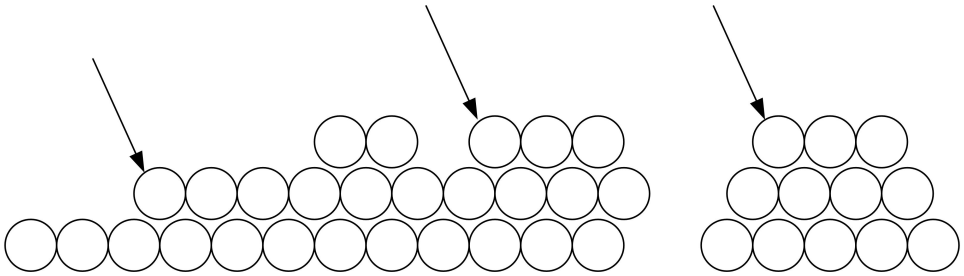

Figure 1.2: Low coordination surface atoms as can be found for large surfaces at surface steps (left arrow) or defects (middle arrow) and small crystallites (right arrow).

1.3.4 Small crystallites

For small crystallites in the nanometer range, the crystallite properties are much more sensitive to the surface than for large crystallites. Due to the increase in dispersion and curvature with a decrease in size, the ratio of edge to flat surface atoms increases. The Van Hardeveld and Hartog statistics [45] provide the number of atoms with a given coordination as a function of the size of idealized crystallites. The number of exposed metal surface atoms is controlled by the crystal structure and the size of the crystal. FCC, HCP and BCC crystals can expose different low energy surfaces [45]. Large crystallites can expose low coordinated atoms at step-surfaces or defects, while small crystallites expose these atoms at ridges between surface faces (see Figure 1.2). This will affect the activity of very small crystallites in the nanometer range.

Another aspect unique to very small crystallites is the change in Fermi level or HOMO (Highest Occupied Molecular Orbital) [46, 47]. The Fermi level is expected to increase with a decrease in size [48] and consequently affects the activity of small crystallites. The center of the *d*-band and the Fermi level is an indication of the HOMO and in turn will affect the chemical properties of the surface [26].

Iglesia showed that the turnover frequency (TOF) does not change with

an increase in dispersion up to 0.11 [49] in agreement with results of Ho *et al.* [50] which suggested that the TOF stays constant up to a dispersion of 0.20. Later work showed that the activity of the metal decreases for crystallites below 5-8 nm [51, 52, 53]. The reason for this loss in activity for very small crystallites is currently not well understood, but might be related to a shift in the Fermi level relative to the centre of the d-band [12, 47].

1.4 Deactivation of Fischer-Tropsch catalysts

Due to the high cost of cobalt, it is important to attain high catalyst activity as well as a long catalyst lifespan [5]. It is therefore crucial to understand the processes at play and the different mechanisms of catalyst deactivation. From an economical and operational point of view, catalyst deactivation should be avoided. If deactivation can not be avoided it should be controlled as far as possible.

Deactivation mechanisms are usually categorized based on the nature of the processes such as mechanical, chemical or thermal effects [54, 55]. The mechanical effects consist of catalyst breakage and fouling, while thermal effects are mainly related to sintering. The chemical effects are related to competitive adsorption, poisoning, phase changes and formation of volatile compounds.

Deactivation is a reduction in the activity per mass of catalyst, change in selectivity or both. A good understanding of the deactivation processes is necessary to establish under which conditions deactivation is facile and understand how activity and selectivity will be affected. The deactivation processes can be classified more fundamentally in terms of how the catalytic function is retarded. Deactivation can be a result of a change in the intrinsic activity of the catalyst, diminished accessibility to the sites and simply just a reduction in surface area or the number of active surface sites.

1.4.1 Change in intrinsic activity

The intrinsic activity is influenced by bulk phase changes, surface reconstruction, size and the population of chemical species on the surface as discussed in the previous section. It is important to realize that a change in the intrinsic activity will be likely to affect the selectivity as well as the activity since the lowest energy pathway is changed. Different pathways will favour different intermediates and consequently also different products. A change in selectivity therefore could be an indication of a change in the intrinsic activity of the catalyst.

1.4.2 Accessibility of active sites

Reduced accessibility of the active sites can have various origins such as a high coverage, competitive adsorption and blockage of the active metal centres.

At high surface coverages, surface species occupy the active sites and do not allow enough space for the elementary steps to take place. The CO dissociation mechanism on iron was suggested to occur in a two step process where the C–O dissociates in the first step after which the surface oxygen diffuses to a neighbouring site [56]. At large surface coverages the second step would not be possible, resulting in a higher dissociation energy due to a blocking of the surface.

Competitive adsorption occurs when gas phase molecules which are inert to the Fischer-Tropsch reaction adsorb on the surface and prevent the reaction intermediates from accessing the sites. Since the adsorption strength for these molecules is usually in the same range as the reactive species, the sites become available upon desorption. This effect usually appears as an inhibition term in a Langmuir-Hinshelwood type rate expression.

Blockage can occur either when gas or liquid phase molecules can not reach the surface, or when adsorbed surface species can not use or reach

the active sites. Strongly adsorbing molecules would block sites in a similar way as molecules guilty of competitive adsorption. These strongly adsorbed unreactive surface species do not desorb from the surface and prevent accessibility to the active site for a substantial amount of time. Usually very small quantities can result in a poisoning effect.

Access of the gas phase molecules to the metal sites is reduced when the surface is blocked by waxy hydrocarbons [49, 57]. Any diffusion of molecules to and from the surface would be reduced as a consequence of the surrounding liquid layer. This will be seen experimentally as a reduced rate but the intrinsic activity of the surface is not necessarily affected.

The formation of carbon overlayers has been reported for various transition state metals such as Fe [5, 58], Co [59, 60] and Ni [61]. These carbon deposits are usually formed in layered graphite structures on the surface [62, 63] and it has been suggested that they are responsible for deactivation [5, 61]. The formation of carbon overlayers is highly dependent on the operating conditions and can occur over short or long time spans.

Blockage of the surface can also occur as a result of support creep, where the active metal is encapsulated by the support due to a strong metal-support interaction. This is a slow process which is not well documented for realistic systems.

1.4.3 Losing active sites

The catalyst activity declines when the number of exposed surface atoms and consequently the number of active sites is reduced. This either occurs due to loss of active metal in the products or due to a change in dispersion. Loss of active metal into the product can have negative effects on downstream activities from the reactor and should be avoided and controlled as far as possible.

If volatile species are formed, an easy pathway exists for the active metal

to leave the reactor. The volatile species are typically in the form of oxides, carbonyls [1] or any other stable volatile compound. The formation of metal carbonyls is possible at high CO partial pressures and would also result in a loss of active catalytic metal.

Mechanical breakage or attrition of the catalyst results in the formation of solid fines which are removed from the reactor with the reaction products [55].

A simple decrease in the number of active sites should not affect the intrinsic activity or the intrinsic selectivity. The activity per unit area should remain the same since the intrinsic activity does not change.

Sintering causes a reduction in the number of surface atoms due to a decrease in dispersion where the dispersion is the ratio of the number of atoms located at the surface of a crystal to the total number of atoms in the crystal. Consequently the number of active sites decreases, resulting in a lower observed activity (per mass of active metal) but not necessarily a lower intrinsic activity (per number of surface atoms).

1.4.4 Thermodynamic considerations for small crystallites

The catalyst activity can be maximized by using highly dispersed catalysts [21]. A high dispersion (above 0.1) is usually obtained for metal crystallites below 14 nm based on the statistics of Van Hardeveld and Hartog [45] (see Figure 1.3). These dispersions can be easily achieved with nano-crystallites which are usually deposited on an insulating support [49].

Due to the high dispersions achieved for nano-sized catalysts, surface properties are important in determining the stability of nano-sized crystallites [64, 65]. The surface energy contribution to the total energy and chemical potential affects the thermodynamics of the nano-crystallites. These effects are present for all materials but can usually be ignored for bulk materials or large crystallites. The effects of the size dependent properties on

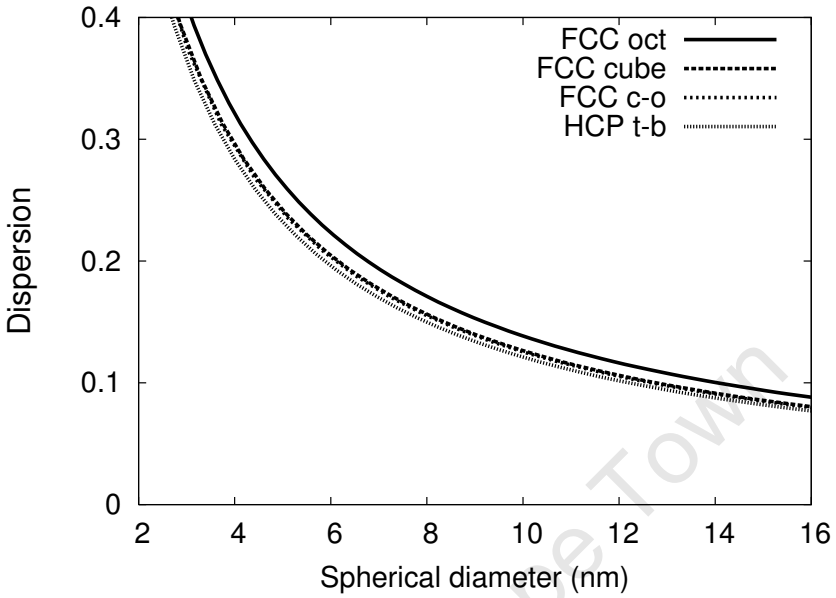

Figure 1.3: Dispersion for FCC and HCP crystals according to the Van Hardeveld and Hartog statistics [45]. The dispersions are given for FCC cube, FCC octahedron (oct), FCC cubo-octahedron (c-o) and an HCP truncated-bipyramid (t-b).

deactivation will form the basis for discussion on the various deactivation mechanisms.

Bulk cobalt is known to exist in either the FCC structure (Face Centered Cubic) or HCP structure (Hexagonal Close Packed) [66]. The HCP structure consists of close packed layers with an ABAB configuration, while the FCC structure consist of close packed layers with an ABCABC configuration. For bulk cobalt, the HCP-FCC cobalt phase transition is at 420 °C [67, 68], suggesting that the HCP-cobalt phase is the most stable phase at Fischer-Tropsch operating temperatures of 200-240 °C.

It was suggested that for small crystallites (below 80-100 nm) FCC-cobalt is more stable than HCP-cobalt (at temperatures below 420 °C) [69, 70]. This can be explained by the lower surface energy of the FCC crystals relative to the HCP crystals for the same size in the range where the surface

energy contribution to the total energy of the crystallite is important.

Analysis of small crystallites of HCP-cobalt in a silica matrix showed that the HCP phase can be stable up to 800 °C [71]. Kitakami *et al.* [69] showed that the HCP-cobalt can transform to FCC-cobalt between 400-450 °C for crystallites with an average diameter of 30 nm. Ram [70] suggested that for crystallites with a diameter less than 20 nm, heat treatment would not affect the crystal structure. The HCP-cobalt can transform to FCC-cobalt by shifting of the planes from ABCABC to ABABAB. A concerted plane shift is not probable due to the high energy cost and a vacancy diffusion mechanism would be more likely.

Highly dispersed catalysts are generally prepared from CoO in which the cobalt atoms are in an FCC arrangement. Reduction of CoO would produce cobalt crystallites with an FCC structure and due to the small size, direct transformation of cobalt crystallites from FCC to HCP is not likely.

It is therefore reasonable to assume that mainly the FCC phase of cobalt is present during the Fischer-Tropsch synthesis.

1.5 Getting a handle on deactivation

1.5.1 Sulfur and nitrogen related deactivation

Sulfur compounds are known to be detrimental to Fischer-Tropsch catalysts and must be avoided as far as possible [1, 25]. Sulfur compounds are sometimes present in the natural gas or coal and contact of sulfur containing compounds with the catalyst must be avoided.

Trace amounts of nitrogen containing compounds might be present in the Fischer-Tropsch feed gas, depending on the feedstocks. The way in which these molecules interact with the surface will determine whether they will play a role in deactivation.

The effects of sulfur and nitrogen containing compounds are related to

the feed gas specifications. In order to eliminate the deactivation from nitrogen and sulfur containing compounds, proper feed gas cleaning is required. The use of ZnO guard beds was proposed as one method of cleaning the feed gas [72, 73].

1.5.2 Oxidation as deactivation mechanism

One of the most debated deactivation mechanisms in cobalt-based Fischer-Tropsch synthesis is the role of oxidation [74]. As mentioned earlier, water is one of the main products in the Fischer-Tropsch process. At large conversions, the water partial pressure and the H_2O/H_2 ratio will become high. High H_2O/H_2 ratios will cause bulk oxidation [22]. Bulk oxidation of cobalt is not possible under realistic Fischer-Tropsch conditions [22].

The oxide phase is not active and oxidation has been suggested to be the cause of deactivation in small crystallites [75, 49]. The formation of the oxide phase is driven by the thermodynamics of the gas phase environment and small crystallites [76]. The size dependent analysis requires accurate size dependent surface energies of the metal and oxide phases. The information on surface energies is not readily available and was previously estimated for the conditions under which oxidation would take place [76]. It is important to quantify the window of operating conditions where oxidation is possible since the maximum activity per mass of catalyst can be obtained for catalysts with a high dispersion of the active metal.

1.5.3 The role of carbon in deactivation

One of the first steps in the Fischer-Tropsch mechanism is the dissociation of CO which leaves carbon and oxygen atoms on the surface. Carbon is thus always present and necessary for the Fischer-Tropsch process to take place. Excess carbon can have detrimental effects on the activity of the catalyst.

Small amounts of carbon result in surface reconstruction [34]. The pres-

ence of hydrogen is likely to reverse this process since CH_x species are not able to perform this surface reconstruction.

High CO partial pressures results in the formation of carbide phases of cobalt [77], but these phases are not readily formed at H_2/CO ratios typical for Fischer-Tropsch operation. The formation of carbide phases is highly unlikely and thus not considered to be responsible for deactivation.

In the case of carbon deposition, graphene or graphite layers are formed, which cover the surface [78] and prevent gas phase molecules from accessing the surface. The formation of carbon sheets has previously been thought to form only at surface defects [61] of transition state metals. Part of this thesis will focus on the likelihood of forming carbon overlayers on defect-free surfaces as well as the interaction of these layers with the surface.

1.5.4 Sintering

Sintering is usually responsible for a loss of active sites by reducing the dispersion of metal crystallites. Less active sites are available when the dispersion decreases resulting in deactivation. Sintering is generally considered to be kinetically slow at moderate temperatures [54] and usually difficult or impossible to reverse. Sintering can be enhanced by the presence of chlorine [55], oxygen and water [54], but is mainly driven by temperature. At high temperatures, the vibrational amplitudes increase to the melting point where the atoms do not remain in a crystal structure [66]. Due to the large vibrational amplitudes at high temperatures, the atoms become mobile which is characteristic of liquids. Sintering is usually related to the melting temperature via the Hüttig and Tamman temperatures. It is known that sintering by diffusion of surface atoms is possible at the Hüttig temperature (0.3 T_{melt}), while the bulk atoms can become mobile at the Tamman temperature (0.5 T_{melt}) [55]. Sintering occurs either via crystallite transport or inter-crystallite transport.

The melting temperature is known to decrease for smaller crystallites [79, 80, 81, 82]. Consequently the Hüttig and Tamman temperatures decrease, enhancing the risk of sintering in small crystallites. By using accurate size dependent surface energies, a thermodynamic model can be used to determine the size dependent melting behaviour. The crystallite sizes susceptible to sintering can thus be defined at any given temperature.

1.6 Scope of study

An excellent case exists for the use of cobalt as a Fischer-Tropsch catalyst. Due to the high cost of cobalt, a high activity along with a long catalyst life is required. This thesis will focus on gaining insight into the driving forces for deactivation mechanisms such as sintering, oxidation and carbon deposition with particular emphasis on nano-sized cobalt catalysts. These aspects have not been studied at a fundamental level for cobalt-based Fischer-Tropsch catalysts yet. This work will focus only on the deactivation mechanisms on pure cobalt, while support effects will not be considered. The catalyst will never be used without support, but valuable insights into the aspects driving deactivation can nevertheless be gained by considering pure unsupported nano-sized cobalt crystallites.

One of the most debated deactivation mechanisms of cobalt-based Fischer-Tropsch synthesis is the oxidation of small crystallites [74]. Van Steen *et al.* [76] derived a model to predict the size dependent oxidation of crystallites. The surface energies used in this model have not been verified and the prediction of the surface energy of CoO will be one of the main focus areas of this work.

An accurate prediction of the size dependent oxidation of cobalt requires accurate metal surface energies. The size dependent melting of the metal can thus be calculated to understand the sintering behaviour of metal nanocrystallites.

Previous work [61] suggested that carbon deposition would only nucleate at surface defects such as steps. Since very small crystallites are not expected to have many step-defects, the possibility for carbon deposition on flat surfaces will also be studied.

All the surface calculations will be done for FCC-Co. This is the most stable phase for highly dispersed Co [69]. As mentioned earlier the finely dispersed catalysts are reduced from the oxide in which the metal atoms have an FCC structure. Small crystallites seem to be locked in their crystal structures [71] and the FCC crystallites are therefore not expected to transform directly to HCP crystallites.

These aspects will be studied using a DFT (Density Functional Theory) approach (see Chapter 2). DFT is based on quantum mechanics and provides an efficient way of calculating accurate energies for surfaces and adsorbed species on surfaces at a quantum mechanical level. Accurate metal and oxide surface energies are calculated in Chapters 3 and 4 to get reliable size dependent chemical potentials for small crystallites. The role of size dependent chemical potentials in deactivation mechanisms such as sintering and oxidation is discussed in Chapter 5. DFT calculations are also used to gain insight into the role of carbon deposition on cobalt-based Fischer-Tropsch synthesis (see Chapters 6 and 7).

References

[1] Anderson, R.B., in "The Fischer-Tropsch Synthesis", Academic Press, Inc., 1984.

[2] The Catalyst Review Newsletter, April 2005, 4.

[3] Steynberg, A.P., Espinoza, R.L., Jager, B., Vosloo, A.C., Appl. Catal. A: Gen. 186 (1999), 41.

[4] Schulz, H., Appl. Catal. A: Gen. 186 (1999), 3.

[5] Dry, M.E., Catal. Today 71 (2002), 227.

[6] Jager, B., Espinoza, R., Catal. Today 23 (1995), 17.

[7] Espinoza, R.L., Steynberg, A.P., Jager, B., Vosloo, A.C., Appl. Catal. A: Gen. 186 (1999), 13.

[8] Van Santen, R.A., Neurock, M., in "Molecular Heterogeneous Catalysis", Wiley-VCH Verlag GmbH & Co. KGaA, Weinheim, 2006.

[9] Ciobîcă, I.M., PhD Thesis, Technical University of Eindhoven, The Netherlands, 2002.

[10] Jiang, D.E., Carter, E.A., Surf. Sci. 547 (2003), 85.

[11] Xu, L., Xiao, H.Y., Zu, X.T., Chem. Phys. Lett. 315 (2005), 155.

[12] Varma, C.M., Wilson, A.J., Phys. Rev. B 22 (1980), 3795.

[13] Sung, S.-S., Hoffmann, R., J. Am. Chem. Soc. 107 (1985), 578.

[14] Hammer, B., Morikawa, Y., Nørskov, J.K., Phys. Rev. Lett. 76 (1996), 2141.

[15] Gajdoš, M., Eichler, A., Hafner, J., J. Phys.: Cond. Matt. 16 (2004), 1141.

[16] Abild-Pedersen, F., Andersson, M.P., Surf. Sci. 601 (2007), 1747.

[17] Zheng, C., Apeloig, Y., Hoffmann, R., J. Am. Chem. Soc. 110 (1988), 749.

[18] Hoffmann, R., "Solids and Surfaces: A chemist's view of bonding in extended structures", VCH Publishers, Inc., 1988.

[19] Liu, Z.-P., Hu, P., J. Am. Chem. Soc. 125 (2003), 1958.

[20] Vannice, M.A., J. Catal. 37 (1975), 449.

[21] Geerlings, J.J.C., Wilson, J.H., Kramer, G.J., Kuipers, H.P.C.E., Hoek, A., Huisman, H.M., Appl. Catal. A: Gen. 186 (1999), 27.

[22] Van Berge, P.J., Van de Loosdrecht, J., Barradas, S., Van der Kraan, A.M., Catal. Today 58 (2000), 321.

[23] Dry, M.E., Chapter 4, in "Catalyst Science and Technology", Springer Verlag, New York, 1981.

[24] Yates, I.C., Satterfield, C.N., Energy & Fuels 5 (1991), 168.

[25] Van Berge, P.J., Everson, R.C., Stud. Surf. Sci. Catal. 107 (1997), 207.

[26] Hammer, B., Norskov, J.K., Surf. Sci. 343 (1995), 211.

[27] Ciobîcă, I.M., Van Santen, R.A., J. Phys. Chem. 107 (2003), 3808.

[28] Ge, Q., Neurock, M., J. Phys. Chem. B 110 (2006), 15368.

[29] Cheng, J., Gong, X.-Q., Hu, P., Martin Lok, C., Ellis, P., French, S., J. Catal. 254 (2008) 285.

[30] Somorjai, G.A., Hwang, K.S., Parker, J.S., Topics in Catal. 26 (2003), 87.

[31] Curulla-Ferré, D., Govender, A., Bromfield, T.C., Niemantsverdriet, J.W., J. Phys. Chem. B 110 (2006), 13897.

[32] Somorjai, G.A., Van Hove, M.A., Acta. Cryst. B51 (1995), 502.

[33] Wilson, J., de Groot, C., J. Phys. Chem. 99 (1995), 7860.

[34] Ciobîcă, I.M., Van Santen, R.A., Van Berge, P.J., Van de Loosdrecht, J., Surf. Sci. 602 (2008), 17.

[35] Schulz, H., Schaub, G., Claeys, M., Riedel, T., Appl. Catal. A: Gen. 186 (1999), 215.

[36] Riedel, T., Schulz, H., Schaub, G., Jun, K.-W., Hwang, J.-S., Lee, K.-W., Topics in Catal. 26 (2003), 41.

[37] Schulz, H., Nie, Z., Ousmanov, F., Catalysis Today 71 (2002), 351.

[38] Wang, X.-G., Weiss, W., Shaikhutdinov, Sh.K., Ritter, M., Petersen, M., Wagner, F., Schögl, R., Scheffler, M., Phys. Rev. Lett. 81 (1998), 1038.

[39] Wang, X.-G., Chaka, A., Scheffler, M., Phys. Rev. Lett., 84 (2000), 3650.

[40] Sun, Q., Reuter, K., Scheffler, M., Phys. Rev. B 67 (2003), 205424.

[41] Reuter, K., Scheffler, M., Phys. Rev. B 65 (2001), 035406.

[42] Hugosson, H.W., Eriksson, O., Jansson, U., Ruban, A.V., Souvatzis, P., Abrikosov, I.A., Surf. Sci. 557 (2004), 243.

[43] Skriver, H.L., Rosengaard, N.M., Phys. Rev. B 46 (1992), 7157.

[44] Weller, S., Hofer, L.J.E., Anderson, A.B., J. Am. Chem. Soc. 70 (1948), 799.

[45] Van Hardeveld, R., Hartog, F., Surf. Sci. 15 (1969), 189.

[46] Efremenko, I., Sheintuch, M., Surf. Sci. 414 (1998), 148.

[47] Phala, N.S., Van Steen, E., Gold Bulletin 40 (2007), 150.

[48] Wood, D.M., Phys. Rev. Lett. 46 (1981), 749.

[49] Iglesia, E., Appl. Catal. A: Gen. 161 (1997), 59.

[50] Ho, S-W., Houalla, M., Hercules, D.M., J. Phys. Chem. 94 (1990), 6396.

[51] Barbier, A., Tuel, A., Arcon, I., Kodre, A., Martin, G.A., J. Catal. 200 (2001), 106.

[52] Bezemer, G.L., Bitter, J.H., Kuipers, H.P.C.E., Oosterbeek, H., Holewijn, J.E., Xu, X., Kapteijn, F., Van Dillen, A.J., de Jong, K.P., J. Am. Chem. Soc. 128 (2006), 3956.

[53] Martínez, A. Prieto. G., J. Catal. 245 (2007), 470.

[54] Bartholomew, C.H., Appl. Catal. A: Gen. 212 (2001), 17.

[55] Moulijn, J.A., Van Diepen, A.E., Kapteijn, F., Appl. Catal. A: Gen. 212 (2001), 3.

[56] Bromfield, T.C., Currula Ferré, D., Niemantsverdriet, J.W., Chem. Phys. Chem. 6 (2005), 254.

[57] Guisnet, M., Magnoux, P., Appl. Catal. A: Gen. 212 (2001), 83.

[58] Shroff, M.D., Kalakkad, D., Coulter, K.E., Köhler, S.D., Harrington, M.S., Jackson, N.B., Sault, A.G., Datye, A.K., J. Catal. 156 (1995), 185.

[59] Font Freide, J.J.H.M., Gamlin, T.D., Hensman, J.R., Nay, B., Sharp, C., J. Nat. Gas Chem. 13 (2004), 1.

[60] Gruver, V., Young, J., Engman, J., Robota, H.J., Prepr. Pap. Am. Chem. Soc. Div. Pet. Chem. 50 (2005), 164.

[61] Bengaard, H.S., Nørskov, J.K., Shested, J., Clausen, B.S., Nielsen, L.P., Molenbroek, A.M., Rostrup-Nielsen, J.R., J. Catal. 209 (2002), 365.

[62] Sault, A.G., Datye, A.K., J. Catal. 140 (1993), 136.

[63] Helveg, S., Lopez-Cartes, C., Shested, J., Hansen, P.L., Clausen, B.S., Rostrup-Nielsen, J.R., Abild-Pedersen, F., Nørskov, J.K., Nature 427 (2004), 426.

[64] Rusanov, A.I., Surf. Sci. Rep. 23 (1996), 173.

[65] Rusanov, A.I., Surf. Sci. Rep. 58 (2005), 111.

[66] Ashcroft, N.W., Mermin, N.D., "Solid State Physics", Thomson Learning, Inc., 1976

[67] Zhao, J-C., Notis, M.R., Scripta Metall. Mater. 32 (1995), 1671.

[68] Sato, H., Kitakami, O., Shimada, Y., Otani, Y., Fukamichi, K., J. Appl. Phys. 81 (1997), 1858.

[69] Kitakami, O., Sato, H., Shimada, Y., Sato, F., Tanaka, M., Phys. Rev. B 56 (1997), 1384.

[70] Ram, S., Mat. Sci. Eng. A 304-306 (2001), 923.

[71] Maurizio, C., Mattei, G., Canton, P., Cattaruzza, E., de Julián Fernández, C., Mazzoldi, P., D'Acapito, F., Battaglin, G., Scain, C., Vomiero, A., Mat. Sci. Eng. C 27 (2007), 193.

[72] "Catalyst Handbook", Second edition. Wolfe Pbulishing Ltd., 1970.

[73] Twigg, M.V. Eds. "Catalyst Handbook", Second edition. Wolfe Pbulishing Ltd., 1989.

[74] Van de Loosdrecht, J., Balzhinimaev, B., Dalmon, J.-A., Niemantsverdriet, J.W., Tsybulya, S.V., Saib, A.M., Van Berge, P.J., Visagie, J.L., Catal. Today 123 (2007), 293.

[75] Schanke, D., Hilmen, A.M., Bergene, E., Kinnari, K., Rytter, E., Ådanes, E., Holmen, A., Catal. Lett. 34 (1995), 269.

[76] Van Steen, E., Claeys, M., Dry, M.E., Van de Loosdrecht, J., Viljoen, E.L., Visagie, J.L., J. Phys. Chem. B 109 (2005), 3575.

[77] Weller, S., J. Am. Chem. Soc. 69 (1947), 2432.

[78] Menon, P.G., J. Mol. Catal. 59 (1990), 207.

[79] Dick, K., Dhanasekaran, T., Zhang, Z., Meisel, D., J. Am. Chem. Soc. 124 (2002), 2313.

[80] Shi, F.G., J. Mater. Res. 9 (1994), 1307.

[81] Hanszen, K.-J., Z. Phys. 157 (1960), 523.

[82] Buffat, P., Borrel, J.-P., Phys. Rev. A 13 (1976), 2287.

Part II

Methodology

Chapter 2

Methodology

In this Chapter a brief overview of quantum mechanics and DFT (Density Functional Theory) is given. This forms the basis of the computational work to follow. The various functionals which contain different levels of theory are highlighted along with their shortcomings. Possible ways of addressing these shortcomings are highlighted since this is highly relevant throughout the thesis. The general setup and methodological approach is discussed along with the analysis of various electronic properties.

2.1 Overview of Quantum Mechanics

In quantum mechanics the wave-particle behavior of electrons is described by the Schrödinger equation [1]. The Born-Oppenheimer nonrelativistic approximation for an N-electron atomic or molecular system [2], is given by standing waves in an eigenvalue formulation as

$$\hat{H}\Psi = E\Psi \tag{2.1}$$

where E is the electronic energy, Ψ is the wave function and $\hat{H}$ is the Hamiltonian operator. The trajectory of electrons is given by the wave function Ψ, which has no real physical meaning, but the square, $|\Psi|^2$, gives the electron density probability in space [1]

$$\rho^{\sigma}(\mathbf{r}) = \sum_i n_i |\Psi_i^{\sigma}(\mathbf{r})|^2. \tag{2.2}$$

The Hamiltonian operator $\hat{H}$ is used to calculate the electronic energy by taking into account the kinetic energy operator ($\hat{T}$) of the electronic wave functions and is the effective potential acting on the electrons ($\hat{V}_{eff}^{\sigma}$)

$$\hat{H} = \hat{T} + \hat{V}_{eff}^{\sigma}. \tag{2.3}$$

The effective potential contains the Coulomb electron-nuclei ($\hat{U}_{en}$) and electron-electron ($\hat{U}_{ee}$) interactions as well as the chemical potential for exchange and correlation μ_{xc}^{σ}. For magnetic systems, the potential differs for the up- and down-spin electrons ($\sigma = \uparrow \; or \; \downarrow$) resulting in different energy levels being formed. Each electron is described by a single particle wave function Ψ_i. The kinetic energy of all non-interacting electrons (n_i) in the system is given by

$$T_0 = \sum_i n_i \int \Psi_i^*(\mathbf{r}) \Big[-\frac{\hbar^2}{2m}\nabla^2 \Big] \Psi_i(\mathbf{r}) d\mathbf{r}. \tag{2.4}$$

The electronic energy (ϵ_i) can therefore be determined exactly, by solving all the one-electron differential equations by inclusion of the electron-electron and electron-nucleus electronic interactions in the potential V_{eff}^{σ} for the up and down spin electrons.

$$\Big[-\frac{\hbar^2}{2m}\nabla^2 + \hat{V}_{eff}^{\sigma}(\mathbf{r}) \Big] \Psi_i^{\sigma}(\mathbf{r}) = \epsilon_i \Psi_i^{\sigma}(\mathbf{r}). \tag{2.5}$$

For the total energy of the system, the nucleus-nucleus repulsion (U_{nn}), which is a function of the geometry only, must be added to the electronic energies.

Analytical solutions for this mathematical formulation do not exist for systems with multiple interacting electrons. The equations must therefore be solved iteratively at a significant computational cost. When the many-body effects between electrons are taken into account, the shape of the wave functions and therefore electron density differ, further increasing computational cost. The study of realistic systems can become computationally too expensive when using this formulation for the calculation of electronic energies of realistic systems. A more efficient formulation of the quantum mechanical problem would enable the calculation of total energies of realistic systems at a quantum mechanical level.

2.2 Formulation of DFT

Density Functional Theory (DFT) is based on the principle that the electronic energy of any system can be determined from the electron density distribution in the ground state [2]. The minimum energy is at the electronic ground state with the correct electron density distribution in space [3]. Therefore the following differential can be written:

$$\left.\frac{\partial E(\rho^\sigma)}{\partial \rho^\sigma}\right|_{\rho^\sigma=\rho_0^\sigma} = 0. \tag{2.6}$$

This theorem was formulated by Hohenberg and Kohn [4] and Kohn and Sham [5] and is an exact representation of quantum mechanics since the electron density is a fundamental quantum mechanical property. The electron density distribution can be described by a much simpler mathematical function and is therefore much easier to solve, while maintaining the exact quantum mechanical formulation. Any operation on the wave function should also be valid for the electronic density. A Hamiltonian as shown in equation 2.3 can be used to determine the energies based on electron density rather than the actual wave function and give correct results.

The fundamental quantities in DFT are the electron density and the corresponding total energy. The one-electron energies are not explicitly calculated, but are very useful in the determination of the properties for materials under consideration. The work function and band-gaps are important properties when comparing the calculated systems with measurable experimental properties.

The one-electron energies of effective electrons have been introduced in the derivation of Kohn-Sham equations as Lagrange multipliers. The Kohn-Sham equations have the form of an eigenvalue problem in which each wave function has an associated eigenvalue ε_i with an occupation number of n_i. Janak's theorem [6] provides a relationship between the total energy (E) and

these eigenvalues where ε_i is the change in total energy with each electron n_i with occupation number of level i

$$\varepsilon_i = \frac{\partial E}{\partial n_i}. \tag{2.7}$$

The total energy for any system can then be formulated exact as a function of the spin dependent density (ρ^σ), with the energy contribution from the: kinetic energy operator (T), Coulomb interaction potential operator (U for nucleus-nucleus, nucleus-electron and electron-electron interactions) and the spin dependent exchange-correlation potential operator (E^σ_{xc})

$$E(\rho^\sigma) = T(\rho^\sigma) + U(\rho^\sigma) + E^\sigma_{xc}(\rho^\sigma). \tag{2.8}$$

The expression for determining the exact kinetic energy from the wave functions is known (equation 2.4), and for any given electron distribution, the Coulomb energy between the electrons and nuclei can be determined using the Coulomb expression. The exchange and correlation effects are more difficult to describe due to the dependence on density and the orbital nature of the atoms involved.

2.3 Exchange-correlation functionals

The exchange and correlation interactions are more difficult to determine than the Coulomb interactions due to the nontrivial nature of these interactions which can be written in exact form as an exchange-correlation potential (μ^σ_{xc})

$$\mu^\sigma_{xc} = \frac{\partial E^\sigma_{xc}(\rho^\sigma)}{\partial \rho^\sigma}. \tag{2.9}$$

The exchange interaction is a result of the Pauli principle, while the correlation effects are qualitatively understood from Hund rules for multiplicity of electrons in orbitals. The Van der Waals interactions is a result of the

long range dipole interactions. The interaction between the dipoles can be permanently induced or fluctuating and are important in weakly bonding systems.

The Pauli principle states that electrons in the same quantum state (of orbital, energy level and spin) tend to avoid each other. This would result in an exchange hole around an electron. The correlation energy involves the pairing of electrons with opposite spin and is an order of magnitude smaller than the exchange energy. These interactions are very important in describing the properties of realistic systems.

For nonmagnetic systems the potential for up- and down-spin electrons is orthogonal. The resulting wave functions have equal energies [1]. In the case of magnetic systems, high spin states are more favorable and the electron energy levels for up- and down-spin are not equal. The exchange-correlation potential is therefore different for the up- and down-spin electrons resulting in an energy splitting between up- and down-spin electronic states. A useful discussion on the details of magnetization is given by Landrum and Dronskowski [7]. The lowest energy levels would always be filled according to the Aufbau principle and high spin states would therefore be favoured if the overall electronic energy is decreased. The mathematical description of these interactions is not straightforward. Consequently, the exchange-correlation potential is the main source of uncertainty in DFT calculations.

The exchange correlation energy, $E_{xc}^{\sigma}(\rho^{\sigma})$, is calculated by rearranging equation 2.9 and integrating over all space. In the development of exchange-correlation potentials, the analogy of "Jacob's ladder" (see Figure 2.1) is used to classify the level of theory incorporated in the functionals [8, 9]. The ladder is denoted as follows: LDA, GGA, meta-GGA, hyper or hybrid-GGA and generalized random phase approximation. The complexity is increased for each rung and in principle, the accuracy should also increase higher up in the ladder. In order to provide an exact functional for ex-

change and correlation suitable for any environment, empirical parameters must be avoided [9]. The different rungs in the ladder symbolize a higher level of theory and more constrains being satisfied. Along with this, greater computational time is required. The first three rungs are based on density derived properties and provide the optimum accuracy to computational expense. The higher rungs include the calculation of exact exchange and exact correlation which require a significant increase in computational cost. Semi-empirical functionals such as B3LYP [10] have also been shown to give good results for its "training sets". Care should be taken when using these potentials outside the "training set" from which they were designed.

2.3.1 LDA

In the first rung, μ_{xc}^{σ} is determined from the electron density distribution only and is called the LDA (Localised Density Approximation) or LSDA (Local Spin Density Approximation) approach

$$E_{xc}^{LSDA}(\rho^{\sigma}) = \int d^3\mathbf{r}\ \rho^{\sigma}(\mathbf{r})\mu_{xc}^{\mathrm{LSDA}}(\rho^{\sigma}) \tag{2.10}$$

This approach is a useful starting point for systems where the deviation from the uniform electron density limit is small. The LDA is exact for the uniform density limit [9]. The energies for various densities was determined by using kinetic Monte-Carlo methods to solve the Schrödinger equation as reported by Ceperley and Alder [11]. This exact correlation data was parameterized by Perdew and Zunger [12] as well as Vosko *et al.* [13]. The LDA approach has been shown to give reasonable results for most solid state systems and properties. The use of LDA results in overbinding and thus shorter bond lengths compared to experiment [14].

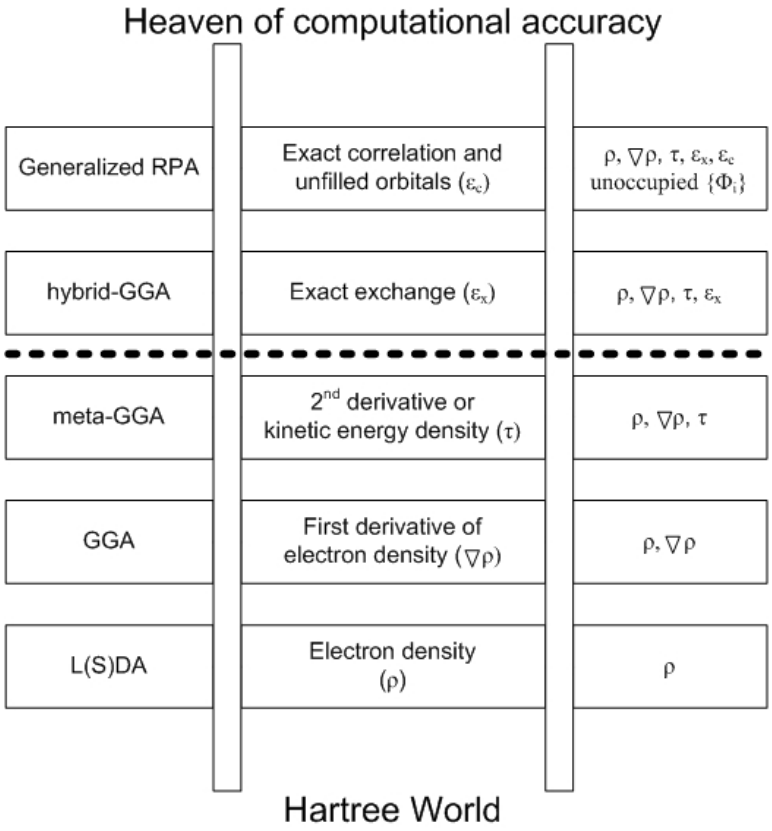

Figure 2.1: Jacob's ladder in the classification of exchange correlation functionals (adapted from Perdew *et al.* [9]). The exchange correlation potentials below the dotted line can be determined from electron density related properties only. Above the dotted line, exact properties related to the orbitals and filling of orbital states are also included. The names for the rung describing the level of theory is given on the left. The additional complexity included in the exchange correlation potential is given in the middle. All the quantum properties required for the specific level of theory can be found on the right hand side.

2.3.2 GGA

Later work suggests that the non-local effects of the electron density gradient should be included as well [15, 16]. The non-local effects result from the shape of the density profile and the inclusion of the non-local effects can be done by taking the first derivative of the density into account. These

functionals are denoted GGA (Generalized Gradient Approximation)

$$E_{xc}^{GGA}(\rho^{\sigma}) = \int d^3\mathbf{r}\ \rho^{\sigma}(\mathbf{r})\mu_{xc}^{\mathrm{GGA}}(\rho^{\sigma}, \nabla\rho^{\sigma}) \tag{2.11}$$

The PW91-GGA approach gives a much better description of realistic systems especially when magnetism is involved [16]. These functionals are still not a complete exact description of all the interactions, but allow the calculation of properties and energy with good accuracy at reasonable computational efficiency. The PBE functional is an exact functional within the GGA formulation and has a similar performance for most properties of metals as the PW91 potential [17]. Further revisions to the PBE were made such as the revPBE [18] and the RPBE [19] to correct errors in correlation interactions for small molecules and adsorption on surfaces. These functionals (rev-PBE and RPBE), however, satisfy less exact constraints [9] and should be used with care. It is therefore important to check that the exchange-correlation functional describes the measurable properties sufficiently [8].

2.3.3 meta-GGA

Some of the more advanced functionals are also being introduced such as the meta-GGA [20, 21], which include higher order functions of the electron density in the formulation.

$$E_{xc}^{mGGA}(\rho^{\sigma}) = \int d^3\mathbf{r}\ \rho^{\sigma}(\mathbf{r})\mu_{xc}^{mGGA}(\rho^{\sigma}, \nabla\rho^{\sigma}, \nabla^2\rho^{\sigma} \text{ or } \tau^{\sigma}) \tag{2.12}$$

The higher order additions can either be in the form of the Laplacian (second derivative) of the density $\nabla^2\rho^{\sigma}(\mathbf{r})$ [20], as for the PKZB functional, or by using the Kohn-Sham orbital kinetic energy density (τ^{σ}), as for the TPSS functional [21]. The kinetic energy density (shown below) is derived from the second order Taylor expansion of the exact-exchange pair density

at small inter electronic distances [22, 23, 24].

$$\tau^{\sigma}(\mathbf{r}) = \frac{\mathbf{1}}{\mathbf{2}} \sum_{\mathbf{i}}^{\text{occ.}} |\nabla^{\mathbf{2}} \mathbf{\Psi}_{\mathbf{i}}^{\sigma}(\mathbf{r})|^{\mathbf{2}} \tag{2.13}$$

The use of meta-GGA functionals have not yet been reported extensively but initial tests show that this formulation improves the atomization and surface energies [9]. Up to the third rung, the computational cost does not increase substantially since the exchange correlation is based on the electron density distribution and derivatives thereof only.

2.3.4 Hybrid methods

Higher rungs of Jacob's ladder introduce aspects which are computationally much more expensive. The fourth rung consists of the hybrid methods, which are being developed to include exact exchange energy density ε_x^{σ} [25, 26].

$$E_{xc}^{hGGA}(\rho^{\sigma}) = \int d^3\mathbf{r}\ \rho^{\sigma}(\mathbf{r}) \mu_{xc}^{hGGA}(\rho^{\sigma}, \nabla\rho^{\sigma}, \nabla^2\rho^{\sigma} \text{ or } \tau^{\sigma}, \varepsilon_x^{\sigma}) \tag{2.14}$$

Exact exchange corrects for the long range non-local effects resulting from the exchange interactions which are not treated properly by the DFT exchange. The GGA gives a good description of short range and local exchange, but the long range non-local part which does not depend on the density, can only be treated properly when using exact exchange [9]. Exact exchange can be calculated using a HF (Hartree-Fock) approach which is very expensive for metals, especially magnetic systems. The current hybrid methods require empirical parameters to relate the ratio of exact exchange and DFT exchange. One of the most common hybrid functionals is the B3LYP functional [27] but other more exact functionals have also been proposed such as the TPSSh [26] and PBE0 [28, 29].

2.3.5 Exact correlation

In the fifth rung of Jacob's ladder, all the Kohn-Sham orbitals are used, therefore the occupied as well as the unoccupied orbitals are included in the determination of the exchange correlation potential. The RPA (Random Phase Approximation) can be used to calculate exact long range correlation. The RPA does not predict the correct short range correlation but this can be corrected by using the GGA correlation [30, 31]. This RPA+ approach is computationally very expensive and not suitable for practical systems yet [9].

Currently the functionals beyond the meta-GGA require significant additional computational cost, in most cases for small improvements in accuracy and are currently not tractable.

2.4 Limitations of the GGA approach

As discussed in the previous sections, the LDA and GGA potentials do not include the necessary ingredients to describe all systems accurately. In many cases reasonable results are obtained at LDA and GGA levels due to cancellation of errors. It is therefore important to be aware of the cases and systems where the LDA and GGA approaches fail in describing the materials, molecules and surfaces properly. The main categories where the GGA approach fails to give a good description is where the role of electronic self-interaction plays a significant role [12], where a large deviation from uniform electron gas exists [32]. Furthermore, Van der Waals interactions [64] can not be described at all at GGA level.

2.4.1 Strong correlation interactions

Since DFT is a quantum mechanical method, it is important that the correct electronic states are calculated. Therefore electrons should be calculated in

the correct configuration with the correct interactions. For some systems it is also important to predict the correct energy levels of the unfilled orbitals. An incorrect description of the levels of the empty orbitals would result in incorrect or no band gap for some insulators [33, 34], or incorrect interactions for molecules such as CO [35] where the filling of the empty orbitals affect the adsorption strength and dissociation [36, 37, 38].

This error is a result of orbital dependent correlation effects which are not included on the first three rungs of DFT. In the case of CO, the singlet-triplet excitation is not described properly [36], while for the Mott insulators the excitation of the d-electrons are not described properly [34]. In the LDA or GGA based DFT approach the energies for the excited states are calculated based on the ground state electron population of orbitals. Therefore the Coulomb repulsion between correlating electrons in the excited states are not accounted for properly [39, 40]. Anisimov *et al.* [41, 42] suggested that the strong correlation effects can be accounted for by using a Hubbard Hamiltonian, which correct the errors from strong correlation effects by adding a Coulomb repulsion term for filled and unfilled orbitals. This approach is generally referred to as DFT+U and has been shown to improve the LDA and GGA calculations for systems where the band gap is a result of strong correlation effects [42].

Some hybrid functionals such as the B3LYP potential was shown to provide reasonable estimates of the band gaps [43, 44, 45]. Work on CO warned against the use of hybrid methods for CO adsorption since the hybrid functionals do not give good results for all systems [46].

2.4.2 Intrinsic surface error correction

The LDA and GGA functionals currently in use work well for systems where their deviations from the idealized uniform electron gas are small. At a metal surface the Kohn-Sham wave functions undergo a transition from

propagating to evanescent character [47, 48]. The bulk electron density therefore decays exponentially into the vacuum. Surface slabs therefore do not fall in the "safe" region of the uniform electron gas [32, 49].

The LDA and GGA potentials are not able to describe exponential decay of the electron density accurately [48]. The exponential decay is a result of the orbital nature of the electron density distribution which is not included in the LDA and GGA potentials [20]. The use of meta-GGA can provide some improvement to this limitation since the higher order derivatives of the density resulting from the orbital nature are included in the exchange correlation potential [21].

A correction scheme based on electron densities was suggested to improve the results for surface energies when using LDA or GGA potentials [32, 48]. The intrinsic surface error correction is mapped on the density using a two parameter exponential decay model [48] and exact correlation for a jellium surface [50]. The correction was designed for the specific flavour of GGA or LDA and must be used to obtain accurate results [51]. These functionals typically only describe the valence electrons, since these electrons are not very localised compared to core electrons. This empirical correction requires the electron density as input (cobalt has an electron density of 0.84 $Å^{-3}$). The typical bulk cobalt electron density requires a minimum correction [52] of 0.22, 0.75 and 0.57 J/m^2 for LDA, PW91 and PBE potentials respectively. This correction is significant since the typical calculated surface energies for cobalt is in the range of 2.02 - 2.49 J/m^2 [53].

2.4.3 The Van der Waals interactions

Another limiting case where the use of LDA and GGA potentials is problematic, arises in systems where Van der Waals interactions are important [8]. The Van der Waals interactions are a result of charge interactions from transient polarization of the electron gas. The Van der Waals interactions

consist of long range non-local interactions between electrons even if there is no orbital overlap [54]. The lack of inclusion of Van der Waals interactions would result in too long bonding distances and weak binding energies. The inclusion of Van der Waals interactions is important for rare-gas systems [55, 56], layered structures such as graphite, BN and MoS_2 [63] and interactions of some gas phase molecules such as Xe with metal surfaces [57].

LDA potentials have been shown to give reasonable results for systems where Van der Waals bonding is important, such as the rare-gas adsorption on a metal surface [57] and the inter-sheet binding in graphite [58]. In these Van der Waals bonded systems there is competition between the Pauli repulsion [57, 59] and Van der Waals (London) attraction. Since the long range and non-local exchange-correlation effects are not calculated properly within LDA and GGA [58, 60, 61, 62], these potentials should not be used when the energies and interactions are determined controlled by Van der Waals interactions.

The short and long range London interactions can be dealt with by using potentials of higher rungs in the Jacob's ladder scheme where exact exchange is included [55, 56], but these calculations would require a high computational cost. The description of long range non-local Van der Waals interactions is still one of the major shortcomings of potentials on the first three rungs in DFT [63, 64, 65, 66]. There is a current effort to develop DFT methods to describe the London type Van der Waals interactions seamlessly using DFT [67, 63, 64, 65, 66, 68, 69], but these methods are not yet mature. Some effort was also dedicated to the design of a semi-empirical interaction potential scheme [58, 70] but in this approach the empirical parameters would be required for every new system.

2.5 Calculational setup

For a general overview on the application of DFT calculations for solids and surfaces, see the review by Mattsson *et al.* [8]. The DFT calculations were performed with the plane wave code VASP (Vienna Ab-Initio Simulation Package) [71, 72, 73, 74, 75]. The calculations for all systems were performed with spin polarization to obtain the magnetic state if it exists.

The electron-ion interactions are described by either ultrasoft pseudopotentials [76, 77] where the core electrons are replaced by a smooth potential or PAW [78, 79] which are essentially all electron potentials. The PAW potentials allow for the easy projection of electrons onto atomic orbitals which is useful for determination of magnetization located on an atom in a crystal structure.

Electron-electron interactions were described by PW91-GGA potentials as generated within VASP [16, 77]. These GGA potentials were used for ultrasoft-psedudopotential and PAW calculations. For some systems tests were also performed using ultrasoft LDA potentials which are based on data from Ceperley and Alder [11] which was parameterized by Perdew and Zunger [12].

Plane waves are used for the representation of the wave functions and the maximum energy of the plane waves included in the calculation is specified by the cut-off energy. A k-point sampling of the electron density was performed using the scheme proposed by Monkhorst and Pack [80]. Along with this k-point grid, a smearing of the band occupancy at the Fermi level is used to improve convergence. The SCF convergence is slow for metals where the band energy levels are very close together, resulting oscillation of the occupancies. Two smearing methods were used to improve the speed of convergence for metallic systems; the Gaussian smearing and the Methfessel-Paxton [81] smearing scheme. For the Gaussian smearing, a Gaussian type function is used to describe the partial filling of bands at the Fermi level

with a certain smearing value σ^{occ}. The resulting band occupancies can be between zero and one for polarized systems. In the Methfessel-Paxton scheme, a set of Hermitian polynomials are used to describe the band filling at the Fermi level. This can result in occupancies smaller than zero and greater than one, which has no physical meaning. The error due to smearing can however be approximated accurately and therefore very accurate results can be obtained with a suitable choice of σ^{occ} which is specific to the system studied. Since different systems were studied, different parameters were used in the electronic setup. The electronic setup parameters will be discussed for each specific system.

For surface systems periodic slabs are cut along a bulk plane and separated by a vacuum spacing which avoids the interaction of surfaces through the vacuum. This vacuum spacing has to be checked along with the slab thickness to ensure that errors do not arise as a result of the geometry.

2.6 Calculation of properties in DFT

2.6.1 Bulk properties

As a result of the approximations made in the DFT formulation and implementation, it is important to check the validity of the results. This is usually done by comparing the experimentally observed and calculated properties of the bulk material. These checks are used to ensure that the electronic potentials can describe the system accurately. For these calculations, a converged k-point grid, cut-off and smearing were used to ensure that the errors result from inaccuracies of the electronic potentials and not due to lack of convergence and numerical techniques.

The calculated bulk properties which can be compared with experimental properties are the lattice parameter, the bulk modulus, magnetization and the energy band structure. The calculated energies of atomization, bond

formation and surface energies can be used to verify the ability of the model to describe the system. The lattice parameter gives an indication whether the inter-atomic potentials are described correctly and whether the theory is able to predict the correct geometry of the system. The bulk modulus is the second derivative of the energy with respect to volume and is therefore an indication of the ability to describe the forces between the ions correctly. The magnetization can be used to check whether the correct electronic states can be predicted by the theory, while the band-gap is an additional electronic property which can be used to measure the ability of the theory to describe the system in the case of an insulator.

2.6.2 Surface energy

The generation of the surface also results in the loss of periodicity of the crystal structure. The surface energy is an increase in energy for a surface atom due to broken bonds for an atom with a coordination lower than in the bulk crystal. In this work, a surface atom differs from a bulk atom only by having a lower coordination than a bulk atom. The surface energy E_{surf} (in *kJ/mol surface atoms* or *eV/surface atom*) is the excess energy which results from broken bonds at the surface. The surface energy for a slab, rod or cube can be defined by taking the difference in energy from the finite system (E_{finite}) and the bulk energy (E_{bulk}) with the same number of atoms (N) divided by the number of surface atoms (N_{surf}).

$$E_{surface} = \frac{E_{finite} - N \times E_{bulk}}{N_{surf}} \tag{2.15}$$

This definition is exact and holds for any geometry such as a cube, rod or slab. For flat surface slabs, the surface energy can be defined per surface atom or surface area (A). The factor 2 is used in the denominator since a surface slab exposes two surfaces, one on either side of the slab.

$$E_{surface} = \frac{E_{finite} - N \times E_{bulk}}{2A} \tag{2.16}$$

The surface energy can then be calculated by using a DFT approach where the surface energy per atom (E_{surf}) is calculated as

$$E_{surf} = \frac{E_{slab} - nE_{bulk}}{n_s} \tag{2.17}$$

in terms of the semi-infinite surface (or rod) E_{slab} and the equivalent bulk energy per atom E_{bulk}. The total number of atoms in the surface slab is n and n_s is the number of atoms with a coordination lower than that of bulk atoms. For the flat surface slabs, the surface energy (γ) can also be written per unit surface area where a surface slab contains two surfaces with an area A on each side of the slab

$$\gamma = \frac{E_{slab} - nE_{bulk}}{2A}. \tag{2.18}$$

For the metal surfaces, the slabs were set up such that the inverse centre symmetry could be used to reduce the computational cost, while keeping the quality of results. Since a finite number of layers were used, the variance of the surface energy with the slab thickness was also checked to ensure that the surface energies were converged with slab thickness. Due to the fact that a periodic unit cell is used for all DFT calculations, a surface can only be formed if there is enough vacuum spacing between different slabs as the unit cell extends to infinity. The vacuum spacing was optimized for the different systems to ensure that no interaction between different surface slabs through the vacuum exists.

2.6.3 Charge analysis

A charge analysis was performed for some systems using the Bader analysis [82, 83]. In the Bader analysis, the electron density distribution is used

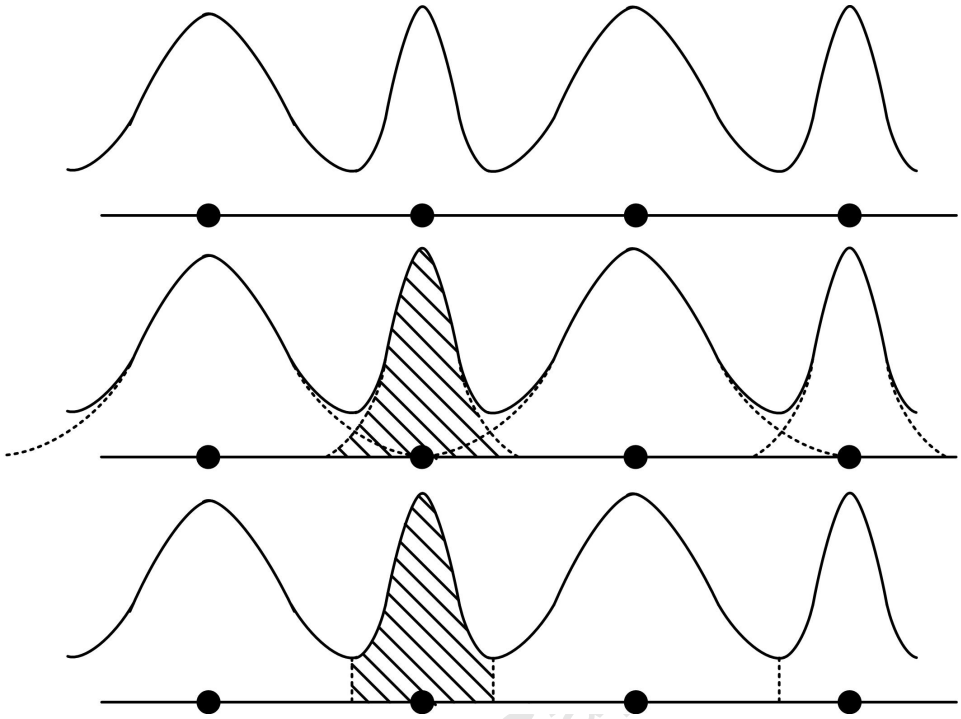

Figure 2.2: Illustration of the Mulliken (middle) and Bader (bottom) partitioning of a 1D charge distribution (top).

to generate surfaces through the regions where the electron density is at a minimum. These zero-flux surfaces are then used to assign a volume to each atom and the electron density within this Bader volume gives the effective charge.

Other definitions for charge determination exist, such as the Mulliken analysis, which require the projection of electrons onto orbitals by fitting exponential functions to the charge density distribution (see Figure 2.2 for illustration).

The absolute charge from the Bader method will differ from the absolute charge found by fitting exponential decay functions to electron density with a Mulliken analysis. There is no clear link between the relationship of the magnitude of Mulliken and Bader charge analysis.

With the Bader method the charge can unambiguously be assigned to an ion based on minimum points in the electron density distribution. The Bader analysis provides a useful method of assigning charge to an atom, enabling the determination of charge transfer in any system. The DFT calculation provides a charge grid within the unit cell allowing for the charges to be integrated numerically. The quality of the grid determines the accuracy to which charges can be calculated.

2.6.4 Density of States

For some systems the total DOS (Density Of States) analysis was used to explore certain aspects involving the energy levels. The DOS analysis is a tool similar to the orbital energy diagrams in chemistry for discrete atoms and molecules. For a periodic system, there are many more atoms and therefore also many more energy levels. An electronic level for an orbital of a molecular system becomes a band for an infinite system (see book by Hoffmann [84]).

The DOS plot indicates the number of electrons at this energy level as well as the highest filled (Fermi) level at 0 eV unless otherwise indicated. These bands can therefore be partially filled (metals) or completely filled (insulator). A Fermi-level E_f is given as output in the VASP calculations. The vacuum potential arising form the use of plane waves in a periodic cell is not accounted for. The VASP Fermi-level must thus be subtracted from the vacuum potential(μ_{vac}) to obtain the work function W_f relative to a vacuum with zero potential:

$$W_f = \mu_{vac} - E_f. \tag{2.19}$$

The partial DOS was calculated by projecting the wave functions onto spherical harmonics to obtain the s, p and d character of the electrons. The PAW

potentials allow a simple projection of the plane waves on to the various atomic sites. The DOS for each orbital was calculated but only reported for the orbitals where significant changes are observed.

2.6.5 Vibrational analysis

A partial Hessian vibrational analysis [85] was performed on the carbon atoms to investigate the effect of adsorption on the graphene sheets and establish whether the adsorption sites found are true minima. Due to the large mass of cobalt relative to carbon, the vibrations of cobalt-atoms can be neglected. The vibrational analysis was performed using a perturbation of 0.005292 Å in the x, y and z directions of the unit cell and electronic calculation setup as described for the system. The zero-point energy was also calculated as in equation 2.20 to include the vibrational contribution to the adsorption energy at 0 K. In this equation, $\hbar$ is the Planck constant, c the speed of light, N_a the Avogadro number and λ the wave number in cm^{-1}.

$$ZPVE = \frac{\hbar c N_a}{2} \sum \lambda_i \tag{2.20}$$

2.7 Summary

The DFT approach is essentially an exact formulation of quantum mechanics but uses the electron density distribution instead of wave functions to calculate the total energy. This reduces the computational expense, while remaining exact in formulation. The total energy has three components: kinetic energy, electrostatic energy and exchange-correlation energy. The description of exact exchange-correlation interactions is currently not tractable for large systems since exact exchange must be calculated using the Hartree-Fock approach. Exchange-correlation interactions can be approximated within the

LDA and GGA formulations. Good qualitative results can be obtained for most systems at very reasonable computational cost. Quantitative information requires corrective measures such as the intrinsic surface energy correction or the DFT+U approach. The plane wave software VASP provides a very efficient implementation to describe solids and surfaces.

References

[1] Atkins, P.W., "Physical Chemistry", Sixth edition, Oxford University Press, 1998.

[2] Parr, R.G., Yang, W., in "Density Functional Theory of Atoms and Molecules", Oxford Science Publications, 1989.

[3] Horn, K., Scheffler, M., Eds. in "Handbook of Surface Science: Electronic Structure", Volume 2, Elsevier, 2000.

[4] Hohenberg, P., Kohn, W., Phys. Rev. 136 (1964), B864.

[5] Kohn, W., Sham, L.J., Phys. Rev. 140 (1965), A1133.

[6] Janak, J.F., Phys. Rev. B 18 (1978), 7165.

[7] Landrum, G.A., Dronskowski, R., Angew. Chem. Int. Ed. 39 (2000), 1560.

[8] Mattsson, A.E., Schultz, P.A., Desjarlais, M.P., Mattsson, T.R., Leung, K., Mod. Simul. Mater. Sci. Eng. 13 (2005), R1.

[9] Perdew, J.P., Ruzsinszky, A., Tao, J., Staroverov, V.N., Scuseria, G.E., Csonka, G.I., J. Chem. Phys. 123 (2005), 062201.

[10] Stephens,P.J., Devlin, F.J., Chabalowski, C.F., Frisch, M.J., J. Phys. Chem. 98 (1994), 11623.

[11] Ceperley, D.M., Alder, B.J., Phys. Rev. Lett. 45 (1980), 566.

[12] Perdew, J.P., Zunger, A., Phys. Rev. B 23 (1981), 5048.

[13] Vosko, S.H., Wilk, L., Nusair, M., Can. J. Phys. 58 (1980), 1200.

[14] Vydrov, O.A., Scuseria, G.E., Perdew, J.P., Ruzsinszky, A., Csonka, G.I., J. Phys. Chem. 124 (2006), 094108.

[15] Perdew, J.P., Phys. Rev. B 33 (1986), 8822.

[16] Perdew, J.P., Chevary, J.A., Vosko, S.H., Jackson, K.A., Pederson, M.R., Singh, D.J., Fiolhais, C., Phys. Rev. B 46 (1992), 6671.

[17] Perdew, J.P., Burke, K., Ernzerhof, M., Phys. Rev. Lett. 77 (1996), 3865.

[18] Zhang, Y., Yang, W., Phys. Rev. Lett. 80 (1998), 890.

[19] Hammer, B., Hassen, L.B., Nørskov, J.K., Phys. Rev. B 59 (1999), 7413.

[20] Perdew, J.P., Kurth, S., Zupan, A., Blaha, P., Phys. Rev. Lett. 82 (1999), 2544.

[21] Tao, J., Perdew, J.P., Staroverov, V.N., Scuseria, G.E., Phys. Rev. Lett. 91 (2003), 146401.

[22] Becke, A.D., Int. J. Quant. Chem. 23 (1983), 1915.

[23] Becke, A.D., J. Chem. Phys. 85 (1986), 1784.

[24] Becke, A.D., J. Chem. Phys. 109 (1998), 2092.

[25] Jaramillo, J., Scuseria, G.E., Ernzerhof, M., J. Chem. Phys. 118 (2003), 1068.

[26] Staroverov, V.N., Scuseria, G.E., Tao, J., Perdew, J.P., J. Chem. Phys. 119 (2003), 12129.

[27] Becke, A., J. Chem. Phys. 98 (1993), 5648.

[28] Ernzerhof, M., Scuseria, G.E., J. Chem. Phys. 110 (1999), 5029.

[29] Adamo, C., Barone, V., J. Chem. Phys. 110 (1999), 6158.

[30] Kurth, S., Perdew, J.P., Phys. Rev. B 59 (1999), 10461.

[31] Yan, Z., Perdew, J.P., Kurth, S., Phys. Rev. B 61 (2000), 16430.

[32] Kohn, W., Mattsson, A.E., Phys. Rev. Lett. 81 (1998), 3487.

[33] Brandow, B.H., Adv. Phys. 26 (1977), 651.

[34] Zaanen, J., Sawatzky, G.A., Allen, J.W., Phys. Rev. Lett 55 (1985), 418.

[35] Feibelman, P.J., Hammer, B., Nørskov, J.K., Wagner, F., Scheffler, M., Stumpf, R., Watwe, R., Dumesic, J., J. Phys. Chem. B 105 (2001), 4018.

[36] Mason, S.E., Grinberg, I., Rappe, A.M., Phys. Rev. B 69 (2004), 161401(R).

[37] Grinberg, I., Yourdshahyan, Y., Rappe, A.M., J. Chem. Phys. 117 (2002), 2264.

[38] Kresse, G., Gil, A., Sautet, P., Phys. Rev. B 68 (2003), 073401.

[39] Terakura, K., Oguchi, T., Williams, A.R., Kübler, J., Phys. Rev. B 30 (1984), 4734.

[40] Sawatzky, G.A., Allen, J.W., Phys. Rev. Lett. 53 (1984), 2339.

[41] Anisimov, V.I., Korotin, M.A., Kurmaev, E.Z., J. Phys.: Cond. Matt. 2 (1990), 3973.

[42] Anisimov, V.I., Zaanen, J., Andersen, O.K., Phys. Rev. B 44 (1991), 943.

[43] Bredow, T., Gerson, A,R., Phys. Rev. B 61 (2000), 5194.

[44] Feng, X., Phys. Rev. B 69 (2004), 155107.

[45] Tran, F., Blaha, P. Schwarz, K.,Novák, P., Phys. Rev. B 74 (2006), 155108.

[46] Stroppa, A., Termentzidis, K., Paier, J., Kresse, G., Hafner, J., Phys. Rev. B 76 (2007), 195440.

[47] Kohn, W. Sham, L.J., Phys. Rev. 137 (1965), 1697.

[48] Mattsson, A.E., Kohn, W., J. Chem. Phys. 115 (2001), 3441.

[49] Langreth, D.C., Perdew, J.P., Phys. Rev. B 15 (1977), 2884.

[50] Mattsson, T.R., Mattsson, A.E., Phys. Rev. B 66 (2002), 214110.

[51] Mattsson, A.E., Armiento, R., Schultz, P.A., Mattsson, T.R., Phys. Rev. B 73 (2006), 195123.

[52] Mattsson, A.E., Jennison, D.R., Surf. Sci. 520 (2002), L611.

[53] Swart, J.C.W., Van Helden, P., Van Steen, E., J. Phys. Chem. C 111 (2007), 4998.

[54] Kohn, W., Meir, Y., Makarov, D.E., Phys. Rev. Lett. 80 (1998), 4153.

[55] Tao, J., Perdew, J.P., J. Chem. Phys. 122 (2005), 114102.

[56] Gerber, I.C., Ángyán, J.G., J. Chem. Phys. 126 (2007), 44103.

[57] Da Silva, J.L.F., Stampfl, C., Scheffler, M., Phys. Rev. Lett. 90 (2003), 066104.

[58] Hasegawa, M., Nisidate, K., Phys. Rev. B 70 (2004), 205431.

[59] Brenan, R.O., J. Chem. Phys. 20 (1952), 40.

[60] Anderson, Y., Langreth, D.C., Lunqvist, B.I., Phys. Rev. Lett. 76 (1996), 102.

[61] Charlier, J.C., Gonze, X., Michenaud, J.P., Europhys. Lett. 28 (1994), 403.

[62] DiVincenzo, D.P., Mele, E.J., Holzarth, N.A.W., Phys. Rev. B 27 (1983), 2458.

[63] Rydberg, H., Dion, M., Jacobson, N., Scrö der, E., Hyldgaard, P., Simak, S.I., Langreth, D.C., Lundqvist, B.I., Phys. Rev. Lett. 91 (2003), 126402.

[64] Dion, M., Rydberg, H., Schröder, E., Langreth , D.C., Lundqvist, B.I., Phys. Rev. Lett. 92 (2004), 246402.

[65] Rydberg, H., Lundqvist, B.I., Langreth, D.C., Dion, M., Phys. Rev. B 62 (2000), 6997.

[66] Langreth, D.C., Dion, M., Rydberg, H., Schröder, E., Hylgaard, P., Lundqvist, B.I., J. Quantum Chem. 101 (2005), 599.

[67] Dobson, J.F., Wang, J., Phys. Rev. Lett. 82 (1999), 2123.

[68] Hult, E., Rydberg, H., Lindqvist, B.I., Langreth, D.C., Phys. Rev. B 59 (1999), 4708.

[69] von Lilienfield, O.A., Tavernelli, I., Rothlisberger, U., Sebastiani, D., Phys. Rev. Lett. 93 (2004), 153004.

[70] Wu. Q., Yang, W., J. Chem. Phys. 116 (2002), 515.

[71] Hafner, J., Comp. Phys. Comm. 177 (2007), 6.

[72] Kresse, G., Hafner, J., Phys. Rev. B 47 (1993), 558.

[73] Kresse, G., Hafner, J., Phys. Rev. B 49 (1994), 14251.

[74] Kresse, G., Furthmuller, J., Comput. Mat. Sci. 6 (1996), 6.

[75] Kresse, G., Furthmuller, J., Phys. Rev. B 54 (1996), 11169.

[76] Vanderbilt, D., Phys. Rev. B 41 (1990), 7892.

[77] Kresse, G., Hafner, J., J. Phys.: Cond. Matt. 6 (1994), 8245.

[78] Blöchl, P.E., Phys. Rev. B 50 (1994), 17953.

[79] Kresse, G., Joubert, J., Phys. Rev. B 59 (1999), 1758.

[80] Monkhorst, H.J., Pack, J.D., Phys. Rev. B 13 (1976), 5188.

[81] Methfessel, M., Paxton, A.T., Phys. Rev. B 40 (1989), 3516.

[82] Henkelman, G., Arnaldsson, A., Jónsson, H., Comput. Mater. Sci. 36 (2006), 254.

[83] Sanville, E., Kenny, S.D., Smith, R., Henkelman G., J. Comp. Chem. 28 (2007), 899.

[84] Hoffman, R., in "Solids and Surfaces: A Chemist's View of Bonding in Extended Structures" VCH Publishers, Inc., 1988.

[85] Li, H., Jensen, J.H., Theor. Chem. Acc. 107 (2002), 211.

Part III

Size Dependent Deactivation

Chapter 3

Size Dependent Metal Surface Energy

3.1 Determination of size dependent metal surface energies

The active metal in cobalt-based Fischer-Tropsch synthesis is deposited as nano-sized crystallites on a support. The nano-sized crystallites provide a high dispersion and therefore a greater fraction of metal atoms are exposed at the surface. Surface atoms differ from bulk atoms by having a lower coordination resulting from less nearest neighbours compared with bulk atoms (see Table 3.1).

In the case of nano-sized clusters, surface metal atoms with a coordination lower than that of typical bulk surfaces are exposed [1]. The fraction of atoms on the surface increases with a decrease in crystallite size. Consequently the larger fraction of low coordinated atoms affects the physical properties such as magnetization [2], Fermi-level [3, 4], surface energies [5] and morphology [6, 7].

Due to the reduced coordination of surface atoms relative to bulk atoms, surface atoms are destabilized with a resulting higher chemical potential of the condensed phase. The thermodynamic formulation of the total chemical potential must be modified for highly dispersed systems to include the effect of the surface energy which results from the reduced coordination. The thermodynamic expressions used for the determination of the size dependent stability are derived in Appendix A.2. In order to be able to determine the size dependent stability, the surface energy is an important parameter required to describe the chemical potential of highly dispersed material.

Lu and Jiang [8] suggested that the surface energy decreases with a decrease in size, but experimental results of Nanda *et al.* [5] on the other hand suggests that the surface energy is higher for small crystallites. When using a simple broken bond model [9], surfaces with a lower coordination have larger surface energies [10]. An increase in surface energy for more open

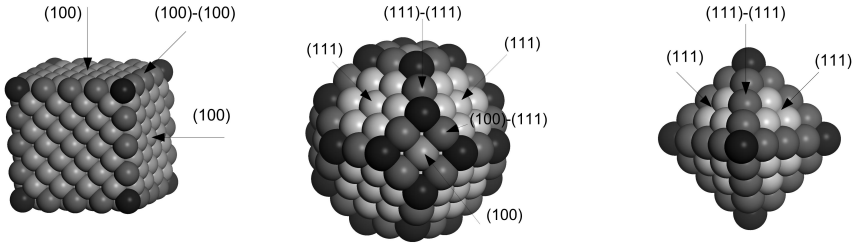

Figure 3.1: Cube, cubo-octahedron and tetrahedron metal clusters with the low coordinated ridge atoms in a darker color.

surfaces was shown for arbitrary surface cuts [11] and low coordinated systems [12] using simple inter-atomic models. The increase of surface energy for more open surfaces was suggested by more accurate DFT slab calculations [7, 13, 14].

The Van Hardeveld and Hartog statistics [1] show that the relative number of low coordinated surface atoms to total number surface atoms increase for smaller crystallites. Consequently the surface energy should increase for smaller crystallites. In order to obtain the size dependent surface energies, the increase in surface energy must be quantified for small crystallites. The surface energies of flat surfaces can easily be calculated for flat surface slabs. The surface energies of low coordinated atoms located at ridges and ridge junctions can not be calculated from flat slabs. An elegant way of determining the energy of these low-coordinated ridge atoms (see Figure 3.1) is by using a nano-rod approach. This approach ensures that only selected types of surface atoms exist based on coordination. The number of nearest neighbours for atoms in various geometries of an FCC crystal is shown in Table 3.1. Another advantage of the nano-rod approach is the computational efficiency of plane-wave DFT to be used to calculate the energies of the nano-rod systems with a high accuracy.

In the determination of the size dependent surface energies, an accurate broken bond model proves to be useful along with the Van Hardeveld and Hartog statistics [1] to derive a size dependent surface energy for crystallites

Table 3.1: Coordination of various atoms in an FCC crystal and surfaces.

Location	Morphology	Nearest Neighbours
Bulk		12
(111)	slab	9
(100)	slab	8
(110)	slab	7
(111)-(111)	tetrahedron	5
(111)-(111)	octahedron	7
(111)-(100)	octahedron	7
(100)-(100)	cube	5
Dimer		1
Atom		0

in the lower nanometer size range. Since a broken-bond model is an empirical approach, accurate data for parameterization is required which can be obtained from DFT calculations [7, 13, 14]. These studies just considered the energies for surface atoms with a coordination as low as seven for the FCC(110) surface in which atoms with a coordination of 11 are also exposed. In the case of nano-crystals the energy of ridge atoms with a coordination as low as five is required. Previous studies based on LDA and GGA formulations for the exchange-correlation interactions are known to have an intrinsic surface energy error (see Chapter 2). The correction of the intrinsic surface energy error will be addressed in this study along with the calculation of surface energy contribution for the low coordinated surface atoms.

3.2 Methodology

Spin polarized DFT calculations were performed using a plane-wave DFT approach as implemented in VASP (see Chapter 2). PW91-GGA calculations with ultrasoft pseudopotentials gave good results for bulk properties [15]. A cut-off energy of 400 eV was used for all calculations along

with a Methfessel-Paxton [16] smearing with $\sigma = 0.1\ eV$. All geometric relaxation of all atoms were performed by minimizing the energy to within $0.1 \times 10^{-3}\ eV$ and the forces to within 0.02 $eV/atom$.

For the bulk calculations, the total energies were converged to within 2 $meV/atom$ when using a k-point grid of $13 \times 13 \times 13$. A cubic FCC unit cell containing four cobalt atoms was used for the bulk calculations. The lattice parameter was optimized by doing single point calculations at various values for the lattice parameter. The bulk equilibrium (lowest energy) lattice parameter was used in all remaining calculations.

Surface calculations were performed using the periodic slab model (see Figures 3.2 and 3.3). In this model a surface is created from a cut in the bulk geometry where the surfaces are separated by a certain vacuum spacing. In this chapter a vacuum spacing of five layers (8.75-10 Å) was used, which resulted in converged results for the surface energy. The slab thickness was varied to ensure a converged surface energy. For this cell a k-point grid of $13 \times 13 \times 1$ was used with required 28 irreducible k-points for the calculation. The surfaces studied were the close packed FCC-Co(111) and the more open FCC-Co(100) surface.

The nano-rods were created to calculate the surface energy contribution of low-coordination surface atoms at the ridges (see Figures 3.4 and 3.5). An extra vacuum dimension was added for the rod systems. For the surface slabs, the metal is infinite in two dimensions with a vacuum separation in one dimension. In the rod unit cells, however, the metal is infinite in only one dimension with vacuum in two dimensions. A variety of rod dimensions can be created from an FCC crystal using this approach of which the square rods and a hexagonal rod will be investigated. The hexagonal rod is shown in Figure 3.4 where all the surface atoms have a coordination of seven. The square rod geometry (see Figure 3.5) exposes flat FCC(100) surfaces connected by (100)-(100) ridge atoms with a coordination number of five.

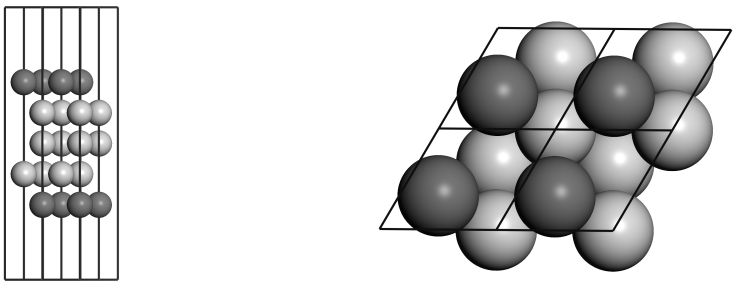

Figure 3.2: Side and top view of the surface unit cell with a thickness of 5 layers for the FCC(111) surface.

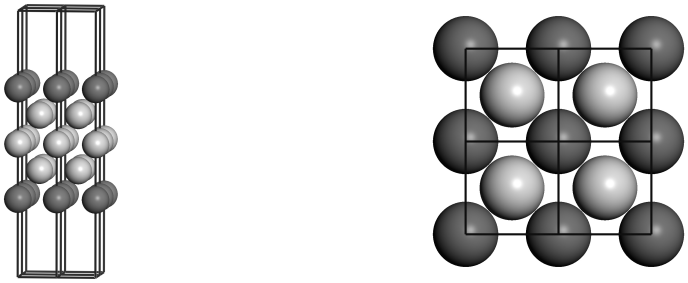

Figure 3.3: Side and top view of the surface unit cell with a thickness of 5 layers for the FCC(100) surface.

In such a rod three types of atoms can be found, of which bulk atoms have a coordination of 12, FCC(100) surface atoms a coordination of eight and the ridge atoms with a coordination of five. The ratio of surface to ridge atoms can be varied by changing the size of the rod resulting in more FCC(100) surface atoms. Square rods with thicknesses from 3 – 8 atomic layers were studied with a 5-layer rod showed in Figure 3.5. In the infinite dimension only one unit cell length was used. This unit cell required a k-point grid of $1 \times 1 \times 13$ to ensure accurate energies along with a vacuum separation between rods of five layers ($8.75 - 10$ Å). The number of atoms with various coordinations are given in Table 3.2.

The total surface energy (excess energy) per surface atom (kJ/mol) of the rod (E_{rod}^{excess}) was determined from the total rod energy (E_{rod}) and the bulk energy (E_{bulk}) as shown below. A surface atom is distinguished from a bulk atom by nearest neighbour coordination only. The number of surface

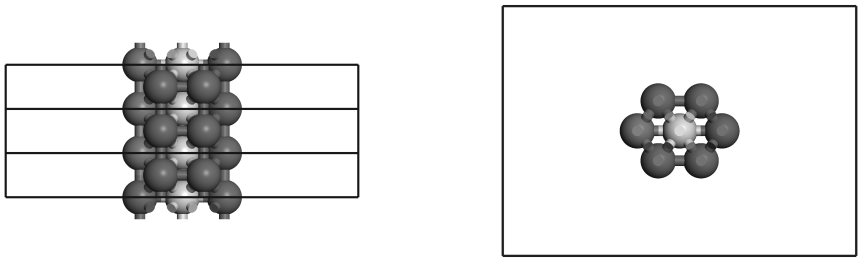

Figure 3.4: Side and top view of the hexagonal rod with one bulk and six surface atoms with a coordination of seven.

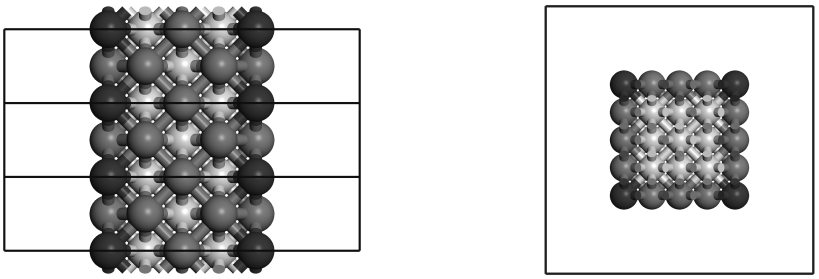

Figure 3.5: Side and top view of the square rod unit cell with a width of 5 atoms.

atoms is given by N_{surf}, while the total number of atoms in the unit cell is N_{tot}.

$$E_{rod}^{excess} = \frac{E_{rod} - N_{tot}E_{bulk}}{N_{surf}} \tag{3.1}$$

This surface energy can be written in terms of contributions from the number of FCC(100) surface atoms ($N_{C=8}$) and the ridge atoms ($N_{C=5}$) and their respective energies $E_{flat-surf}$ and E_{ridge}.

$$E_{rod}^{excess} = N_{C=8}E_{flat-surf} + N_{C=5}E_{ridge} \tag{3.2}$$

Since the surface energy of the FCC(100) surface atoms is known, the energy contribution of the ridge atom to the total surface energy can be determined as shown below. It is assumed that the surface energy of the FCC(100) surface atoms is similar for the surface slabs and on the (100)

Table 3.2: Number of atoms of each coordination for square FCC rods of various sizes. The size of the rod is given in terms of the number of atoms in the width of the rod.

Size	width in atoms	N_{tot}	$N_{C=12}$	$N_{C=8}$	$N_{C=4}$
$3 \times 3 \times 1$	3	9	1	4	4
$4 \times 4 \times 1$	4	16	4	8	4
$5 \times 5 \times 1$	5	25	9	12	4
$6 \times 6 \times 1$	6	36	25	16	4
$7 \times 7 \times 1$	7	49	36	20	4
$8 \times 8 \times 1$	8	64	49	24	4

faces of the rod.

$$E_{C=5} = \frac{E_{rod} - N_{C=8}E_{flat-surf} - N_{tot}E_{bulk}}{N_{C=5}} \tag{3.3}$$

Similarly, for the hexagonal rod, the energy of the FCC(111-111) and FCC(111-100) ridge atoms with a coordination of seven was determined. The surface energy for the hexagonal rod can be determined as follows.

$$E_{C=7} = \frac{E_{rod} - N_{tot}E_{bulk}}{N_{C=7}} \tag{3.4}$$

Surface energies are among the properties which can not be described accurately with the LDA or GGA exchange-correlation potentials (see Chapter 2), due to an inaccurate description of the exponential decay of the electron density into the vacuum [17]. A correction scheme was proposed to improve the calculated surface energies based on the electron density [18, 19, 20] and the surface area. All corrections were implemented based on the bulk electron density of cobalt (0.84 Å^{-3}) with a resulting correction of the PW91 [20] surface energy of 0.75 J/m^2 (0.468 $eV/Å^2$). The intrinsic surface energy error correction is added to the calculated slab energy from which the surface energy is then calculated.

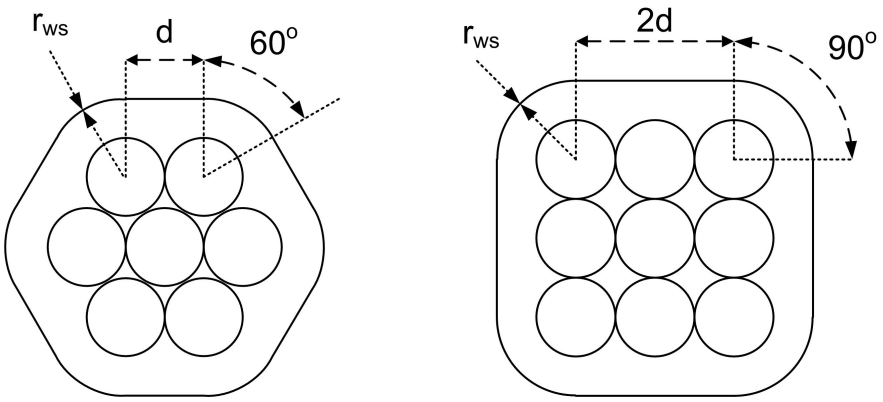

Figure 3.6: Illustration of the determination of the surface area of the square and hexagonal rods to which the intrinsic surface energy error correction is applied. The shortest nearest neighbour distance is d, while r_{WS} is the Wigner-Seitz radius of cobalt.

This correction is also required for the rod structures. The surface "area" over which the correction should be applied should be defined carefully for the rods since the surface is not just simply a flat area but the area that encloses the rod. The total area was calculated from the sum of the "flat" and "spherical" contribution. The "flat" surface area of the (100) faces is calculated between the centres of the ridge atoms for different ridges. The "spherical" areas around the ridge atoms are calculated by using the curved cylindrical area that would connect the "flat" areas with a Wigner-Seitz radius of cobalt ($r_{WS} = 1.38$ Å). Similarly for the hexagonal rod, the total area was calculated from the sum of the "flat" area between the ridge atoms and the "spherical" area around the ridge atoms. The determination of the surface area is demonstrated in Figure 3.6 where d is the shortest interatomic distance.

These energies are used to derive the contribution of the various coordinated atoms to the total surface energy.

Table 3.3: Calculated surface energies in J/m^2 ($eV/atom$) for the flat FCC-Co(111) and FCC-Co(100) surfaces.

Surface	Unrelaxed	Relaxed	γ_{corr} [a]	Exp. [b]
(111)	2.06 (0.70)	2.02 (0.68)	2.77 (0.93)	2.51
(100)	2.49 (0.97)	2.46 (0.95)	3.19 (1.27)	2.51

[a] Correction based on bulk cobalt electron density for PW91 functional [20]

[b] Experimental value estimated from liquid drop experiments at melting temperature and extrapolated to 0 K [25]

3.3 Results

The periodic DFT approach provided good results for the measurable bulk properties of Co. The lattice parameter was found to be 3.535 Å which is in good agreement with the experimental value of 3.550 Å [21]. Values of 3.580 Å [7] and 3.494 Å [22] have been reported previously. A bulk modulus of 196.1 GPa was found which compares well with the experimental value of 191.0 GPa [23]. The calculated magnetic moment of 1.66 μ_B agrees well with the experimental value of 1.70 μ_B [24]. Based on the measurable properties for bulk FCC-cobalt the US-GGA approach gives a good description of the basic properties of Cobalt.

The surface energies were calculated using the slab model for the FCC-Co(111) and FCC-Co(100) surfaces (see Table 3.3) and compare well with the experimental estimates of the surface energy. Surface energies reported for the HCP-Co(0001) surface, which is analogous to the FCC-Co(111) surface, gave energies of 2.77 J/m^2 [7] and 3.18 J/m^2 [14].

The surface energies for cobalt showed very little sensitivity to the thickness of the slab [15] suggesting that the Co–Co interactions are mainly governed by the nearest neighbour interactions and that long range interactions do not play a major role in the surface energies.

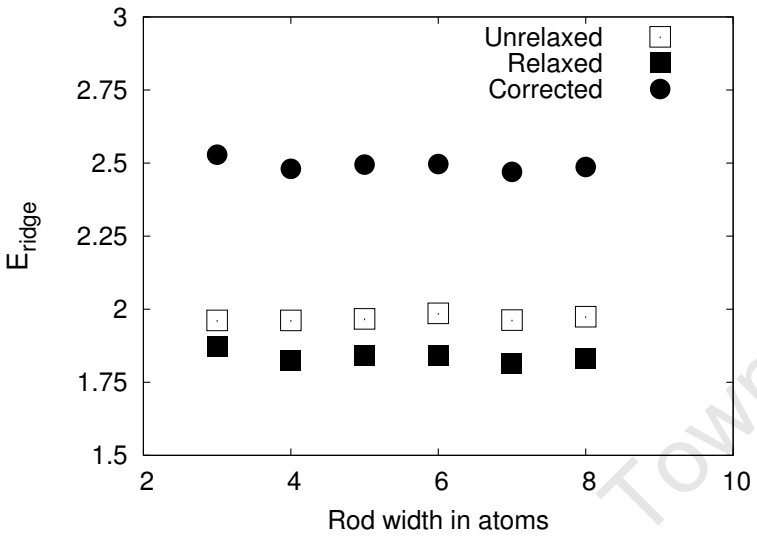

Figure 3.7: Surface energies ($eV/atom$) of the ridge atoms with a coordination of five as calculated from rods of various thicknesses. The ridge energies corrected for the intrinsic surface energy error is given for the relaxed rods.

The FCC-Co(111) and FCC-Co(100) surfaces showed minor relaxations which resulted in minimal lowering of the surface energy (see Table 3.3). This was the result of the relaxation surface stress by minimizing the forces between the atoms which result from the reduced coordination of atoms at the surface.

The rods were used to calculate the surface energy contribution of ridge atoms with a low coordination. Since the surface energy of the FCC-Co(100) surface is know from the slab calculations, the energy for the ridge atoms can now be calculated. In order to check that converged energies were obtained, rods of various sizes were calculated. This resulted in changes to the relative number of bulk, FCC-Co(100) and ridge atoms. The change in the rod width gives an indication of the robustness of the approach to calculate the surface energies of the ridge atoms with a coordination of five. It can be seen from Figure 3.7 that the energy for the ridge atoms do not change significantly with the rod width with variation of less than 2 kJ/mol (20 $meV/atom$).

The relaxation of the rod surface resulted in the contraction of the surface atoms toward the centre of the rod. This is to strengthen the interaction with the remaining neighbours due to the destabilization resulting form the broken bonds. The ridge atoms have a greater destabilization due to more broken bonds and would consequently try to gain stabilization from interaction with remaining neighbouring atoms.

The rod structures were found to have slightly greater magnetization compared to the bulk and flat surface slabs. This enhanced magnetization scales with the number of ridge atoms and suggest that the ridge atoms have a magnetization of 2.2 – 2.3 $\mu_B/atom$ compared to the 1.60 $\mu_B/atom$ calculated for bulk atoms. The surface atoms for the slab systems did not show an enhanced magnetization. This means that the atoms with a lower coordination have more unpaired electrons. Enhanced magnetization have been reported previously for nanoclusters of Rh [2, 26]. Relaxation of the rod did show a reduction in the magnetization suggesting that a greater interaction with nearest neighbours quench the magnetization.

The surface energy of a hexagonal rod was calculated since surface atoms with a coordination number of seven are exposed. A hexagonal rod was used which contain seven atoms in a unit cell of which one is a bulk atom with a coordination of 12. The surface atoms are all ridge atoms with a coordination of seven with four FCC(111-100) ridge atoms and two FCC(111-111) ridge atoms that would be found in a cubo-octahedron. The corrected surface energy of surface atoms with a coordination number of seven (as found in a hexagonal rod) was found to be 1.75 $eV/atom$.

3.4 Size dependent surface energy calculations of cobalt crystallites

The information on surface energies from the slab and rod calculations is used to determine the size dependent surface energies of idealized nano-sized clusters described by the Van Hardeveld and Hartog statistics [1]. In the bulk metal, cobalt atoms have 12 nearest neighbours and no surface energy contribution. The coordination dependent energies from DFT calculations are plotted against the number of broken bonds. The experimental cohesion energy is used for the atom with 12 broken bonds compared to the bulk metal (see Figure 3.8). The cohesion energy is the energy difference between a single atom and a bulk atom. Methfessel *et al.* [13] warned against the use of the DFT calculated cohesion energy due to the sensitivity of the cohesion energy to the energy of the atom, especially for magnetic material. The experimental cohesion energy of cobalt (4.4 $eV/atom$ or 425 kJ/mol) was used in this analysis.

The corrected surface energies of DFT calculations were plotted against the number of broken bonds. These surface energies are shown to be a linear function of the number broken bonds. The surface energies for atoms with 3, 4, 5 and 7 broken bonds were calculated from flat surfaces and nano-rods. A straight line with a slope of 0.3574 can be fitted through the corrected data with $R^2 = 0.9948$. This gives a bulk cohesion energy of 4.29 eV (414 kJ/mol). This value is within 3 % of the experimental cohesion energy. The coordination dependent surface energy (in $eV/atom$) is given as shown below where C is the coordination number of the surface atom.

$$E_C^{excess}(eV/atom) = 0.3574\ C \tag{3.5}$$

The surface energies for low coordinated surface atoms for which no DFT information was available, were calculated from this correlation. Since the

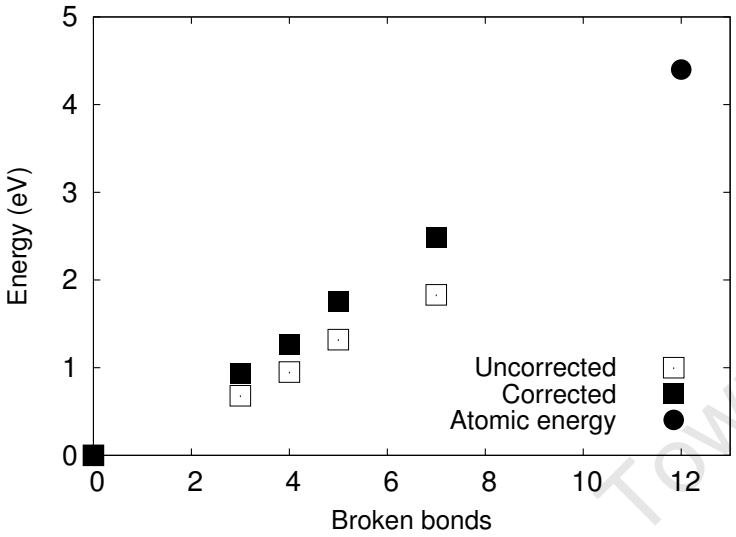

Figure 3.8: Surface energies as a function of the number of broken bonds showing. The surface energies corrected for the intrinsic surface energy error show a linear relationship with the number of broken bonds.

number of these atoms are small, the error should be minimal.

For a simple broken bond model, all the bonds are treated to have an equal strength [9]. The current evidence for the corrected surface energy supports the theory that a linear relationship exists between the coordination number and the surface energy contribution of the surface atom. This is not unreasonable since for a FCC crystal, any atom has 12 nearest neighbours. Since all 12 nearest neighbours have the same distance, chemical intuition suggests that the bonds should have the same strength. These results are contradictory to previously published work on surface energies and broken bond models which suggest that the broken bonds have a square root dependency on the coordination [13, 27, 28].

Methfessel *et al.* [13] suggested the relationship between surface energy contribution and coordination to be described by a square root fit of the coordination, based on DFT-LDA calculations of the atoms as well as the (111), (100) and (110) surfaces. These surfaces have coordinations of 9,

8 and 7 respectively for the surface atoms, while the (100) surface also has surface atoms with a coordination of 11 in the second layer. Their results for surface energies (not corrected for intrinsic surface energy error) fitted better with a square root type dependency. Our results for the uncorrected surface energies of the FCC(111) and FCC(100) surfaces and the cohesion energy fits better with a square root type dependency, but the picture changes when applying the intrinsic surface energy error correction to account for the exchange correlation interaction of the exponentially decaying electron densities. The intrinsic surface energy error correction on the rods showed that the intrinsic surface energy error becomes greater for surface atoms with a lower coordination. Consequently it is very important to apply the intrinsic surface energy error correction when calculating the surface energies of any surface using GGA potentials.

Spanjaard and Desjonqueres [27, 28] suggested this square root dependency of the coordination is based on the bonding energy given by the second moment of the tight binding approach. The relationship of the overlap integral and the bandwidth is a general feature of the tight binding method. The tight binding approach has some limitations as discussed by Ashcroft and Mermin [21]. One of the limitations is that the highest bands in metals are broad since the spatial ranges are comparable to the lattice parameter and the tight binding approximation is then of doubtful validity. The tight binding approximation might fail for systems with partially filled bands which is typical for transition state metals. The tight binding approach does not take important electron-electron interactions into account which is crucial in the calculation of electronic levels in magnetic materials. The tight binding method is thus not a reliable tool for understanding the behaviour of metal surface atoms.

The surface energies calculated from DFT methods are all calculated at 0 K. At higher temperatures, the vibrational contribution to the surface

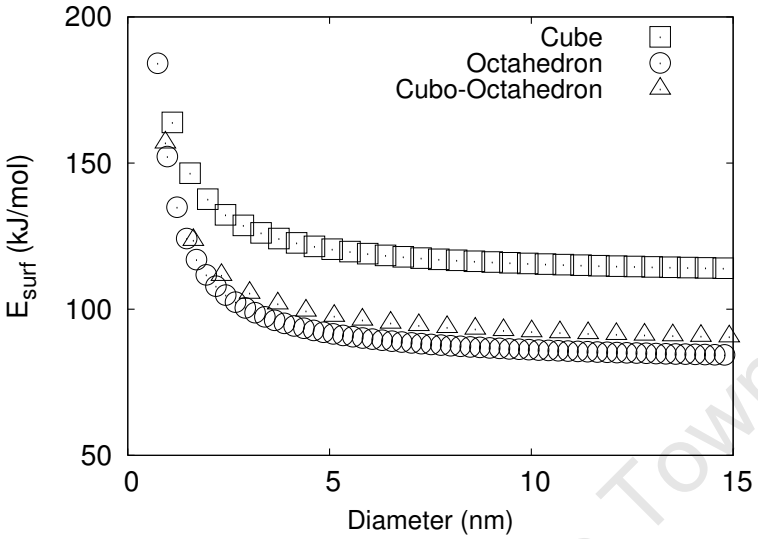

Figure 3.9: Size dependent surface energies for different shapes of nanocrystals. The surface energies at 500 K are given by the broken bond model and Van Hardeveld-Hartog statistics.

energy would increase and affect the entropy which would then reduce the surface energy. Overbury [29] suggested an empirical equation to be used for determining temperature dependent surface energies

$$\gamma = \gamma^0 \left(1 - \frac{T}{T_C}\right)^{1+R} \tag{3.6}$$

with an R value for Cu and Ag of 0.22. This method can be used to determine the surface energies at the temperatures of interest.

The surface energies for atoms with coordinations not calculated from the DFT analysis were estimated using the broken bond model. The surface energies along with the Van Hardeveld-Hartog statistics were used to determine the size dependent surface energies. The surface energies for the different crystals are given at a temperature of 500 K.

3.5 Conclusions

The metal rods can be used for the determination of surface energy for low coordinated surface atoms which are likely to be exposed on small crystallites in the nanometer size range. The uncorrected surface energies agree well with previously published work but in this case the surface energies were corrected for the intrinsic surface energy error which inherent in LDA and GGA level calculations.

The surface energies for low coordinated atoms on the ridges of nano-crystallites were calculated. The nano-rod approach provides an efficient way of calculating the energies of these systems by using plane waves and maintaining a geometry similar to that of the actual crystallite. Minor relaxations were observed for the low coordinated atoms along with an increase in magnetization per ridge atom.

The careful analysis of the coordination dependent surface energies showed that the relation between the coordination and the surface energy is virtually linear. This is contradictory to previously reported trends which suggested a square root dependency of the surface energy. These calculations did not include the intrinsic surface energy error correction. The surface energies corrected for the intrinsic surface energy error and temperature are used in the determination of the size dependent chemical potential of crystallites in the nanometer size range.

References

[1] Van Hardeveld, R., Hartog, F., Surf. Sci. 15 (1969), 189.

[2] Chen, J.P., Sorensen, C.M., Klabunde, K.J., Hadjipanayis, G.C., Phys. Rev. B 51 (1995), 11527.

[3] Wood, D.M., Phys. Rev. Lett. 46 (1981), 749.

[4] Liu, S.-R. Zhai, H.-J., Wang, L.-S., Phys. Rev. B 64 (2001), 153402.

[5] Nanda, K.K., Maisels, A., Kruis, F.E., Fissan, H., Stappert, S., Phys. Rev. Lett. 91 (2003), 16102.

[6] Kitakami, O., Sato, H., Shimada, Y., Sato, F., Tanaka, M., Phys. Rev. B 56 (1997), 1384.

[7] Vitos, L., Ruban, A.V., Skriver, H.L., Kollár, J., Surf. Sci. 411 (1998), 186.

[8] Lu, H.M., Jiang, Q., J. Phys. Chem. B 108 (2004), 5617.

[9] Romanowski, W., Surf. Sci. 18 (1969), 373.

[10] Cyrot-Lackmann, F., Surf. Sci. 15 (1969), 535.

[11] Wang, S.G., Tian, E.K., Lung, C.W., J. Phys. Chem. Solids 61 (2000), 1295.

[12] Robertson, I.J., Heine, V., Payne, M.C., Phys. Rev. Lett. 70 (1993), 1944.

[13] Methfessel, M., Hennig, D., Scheffler, M., Phys. Rev. B 46 (1992), 4816.

[14] Skriver, H.L., Rosengaard, N.M., Phys. Rev. B 46 (1992), 7157.

[15] Swart, J.C.W., Van Helden, P., Van Steen, E., J. Phys. Chem. C 111 (2007), 4998.

[16] Methfessel, M., Paxton, A.T., Phys. Rev. B 40 (1989), 3516.

[17] Mattsson, A.E., Kohn, W., J. Chem. Phys. 115 (2001), 3441.

[18] Mattsson, T.R., Mattsson, A.E., Phys. Rev. B 66 (2002), 214110.

[19] Mattsson, A.E., Jennison, D.R., Surf. Sci. 520 (2002), L611.

[20] Mattsson, A.E., Armiento, R., Schultz, P.A., Mattsson, T.R., Phys. Rev. B 73 (2006), 195123.

[21] Aschroft, N. W., Mermin, N. D., in "Solid State Physics", Holt, Rinehart and Winston, New York, 1976.

[22] Milman, V., Winkler, B., White, J. A., Pickard, C. J., Payne, M.C., Akhmatskaya, E. V., Nobes, R. H., Int. J. Quant. Chem. 77 (2000), 895.

[23] Mehl, M. J., Papaconstantopoulos, D. A., Phys. Rev. B 54 (1996), 4519.

[24] West, A. R., "Basic Solid State Chemistry", 2nd ed., Wiley & Sons Ltd., New York, 1999.

[25] Tyson, W.R., Miller, W.A., Surf. Sci. 62 (1977), 267.

[26] Reddy, B.V., Khanna, S.N., Dunlap, B.I., Phys. Rev. Lett. 70 (1993), 3323.

[27] Spanjaard, D., Desjonquères, M.C., Phys. Rev. B 30 (1984), 4822.

[28] Desjonquères, M.C., Spanjaard, D., J. Phys. C: Solid State Phys. 15 (1982), 4007.

[29] Overbury, S.A., Bertrand, P.A., Somorjai, G.A., Chem. Rev. 75 (1975), 547.

Chapter 4

Size Dependent Surface Energy of CoO

4.1 Introduction

Cobalt oxides are not considered to be active for the Fischer-Tropsch synthesis [1, 2, 3]. High water partial pressures have been reported to have an irreversible deactivating effect on supported cobalt catalysts [1]. Although bulk oxidation is not favoured thermodynamically, oxidation of the catalyst has been reported along with reduced catalyst activity at high H_2O/H_2 ratios [4]. It has been suggested that smaller crystallites might oxidize during the Fischer-Tropsch synthesis [1, 2]. The oxidation of small crystallites was explored based on a thermodynamic analysis which includes size dependent surface energies by van Steen *et al.* [5] and was shown to be consistent with measured size dependent oxidation behaviour [6].

A thermodynamic model which includes size dependent surface energies was derived by van Steen *et al.* [5] (see Appendix A.2 for derivation) which incorporates the size dependency in a diameter term for Co (d_{Co}) as well as the size dependent surface energies for cobalt ($\gamma_{Co} = f(d_{Co})$) and CoO ($\gamma_{CoO} = f(d_{CoO})$). The ratio of the size dependent surface energies ($\gamma_{CoO}/\gamma_{Co} = f(d_{Co})$) is used in the thermodynamic oxidation model. The surface energies of crystallites with the same number of cobalt atoms in the metal and oxide phases were used for different sized crystals. The thermodynamic expression for the conditions where oxidation would not occur can be written as shown by equation 4.1.

$$\mu^0_{CoO(s)} + \mu^0_{H_2(g)} - \mu^0_{Co(s)} - \mu^0_{H_2O(g)} + RTln\left(\frac{p_{H_2}}{p_{H_2O}}\right) + \\ + \frac{6\gamma_{Co}}{\rho_{Co}d_{Co}}\left(\frac{\gamma_{CoO}}{\gamma_{Co}}\left(\frac{\rho_{Co}}{\rho_{CoO}}\right)^{\frac{2}{3}} - 1\right) > 0 \qquad (4.1)$$

This formulation is thermodynamically exact and accurate size dependent surface energies are required to predict the correct size dependent oxidation behaviour. The surface energy for CoO is not known and is calculated

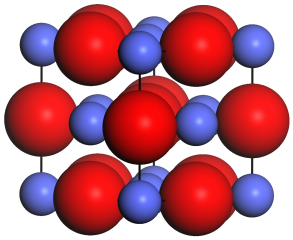

Figure 4.1: The cubic unit cell of CoO with small cobalt atoms and large oxygen atoms. The crystal consists of FCC lattices of cobalt and oxygen atoms.

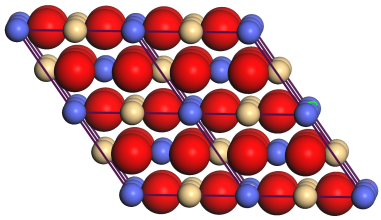

Figure 4.2: Unit cell used for the AFMII structure where the up- and down-spin cobalt atoms are the small atoms shown with different colours. Oxygen is given by large atoms.

in this Chapter. The surface energy for CoO can be compared with other ionic structures such as NaCl and MgO for which experimental surface energies have been reported [7].

Size dependent surface energies for metallic systems can be described easily using a nearest neighbour broken bond type approach as shown in Chapter 3. Bonding in ionic structures is generally considered to have a long range ionic and nearest neighbour covalent contribution. It is therefore unlikely that accurate surface energies can be calculated from a purely ionic model [5] or a purely broken bond model [8].

The electrostatic method used by van Steen *et al.* [5] determined the surface energy of CoO purely based on the electrostatic interactions. The total charge interaction was summed over all ions as given by the Coulomb expression. An estimated charge of 1.22 e, based on the heat of sublimation of CoO was used, resulting in a CoO surface energy of 0.46 J/m^2. This method is crude at best and the reliability of this energy is not known. Since the surface energy of CoO is crucial in the determination of the size dependent stability, an accurate value is required. DFT+U calculations were performed to establish an accurate surface energy for CoO.

DFT is a quantum mechanical method and reliable energies can only be calculated from the correct electronic configuration. CoO is a Mott insulator [9] with an unique type II anti-ferromagnetism (AFMII) [10] where spins are aligned along the (111) direction. Below the Néel temperature the CoO lattice distorts slightly as a result of the AFMII structure [11]. CoO has a distinctive band gap [12] which is linked to the anti-ferromagnetic nature of the oxide [13]. CoO is known to be an insulator up to 1400 K [9], while the Néel Temperature (anti-ferromagnetic to para-magnetic phase transition temperature) is only 291 K [14]. Therefore the para-magnetic and the AFMII phases are insulating. The typical operating temperature for the Co-based Fischer-Tropsch synthesis ranges from 473-513 K [15]. The phase present at these conditions would thus be the para-magnetic phase.

Shull *et al.* [16] suggested that in a para-magnetic phase of MnO, neighbouring magnetic moments tend to align, resulting in a short range AFM order above the Néel temperature. Mott *et al.* [17] suggested a similar behaviour for other Mott-type AFM insulators above the Néel temperature. This would suggest that each cobalt atom would be in a high spin magnetic state and that the magnetic order exists only over a very short range. The neutron diffraction data of para-magnetic CoO showed a small (averaged) magnetization per atom [18] suggesting an AFMII state with short range order rather than a non-magnetic state. The lack of long range order makes detection of magnetization located on the ions difficult. A para-magnetic state with some short range magnetic order is very different from a non-magnetic state given that the orbital filling and electron-electron interactions are very different for these to magnetic states. The AFMII phase would therefore be used to calculate properties of CoO.

The unique electronic properties of Mott insulators pose a major challenge to DFT since DFT is a ground state theory (see Chapter 2). The standard LDA-DFT is known to reproduce the experimentally found band

gaps for the Mott-insulator class materials with great difficulty [19]. The bulk properties of CoO and other Mott insulators were reproduced successfully by using the DFT+U [20, 21].

This chapter will focus mainly on determining the size dependent surface energy for cubic CoO crystals. The bulk and surface energies of CoO was calculated using the DFT+U approach. The surface energies will be corrected for the intrinsic surface energy correction inherent of DFT at LDA and GGA level [22, 23]. Only the CoO(100) surface is investigated since it is expected to be the most stable surface and therefore the most abundant, as it is the most densely packed non-polar surface of CoO [24, 25]. The surface energies will be calculated using an approach based on the ionic and broken bond contributions to the surface energy. Since no information is available on the surface energy of CoO, the results will be compared with other ionic systems for which the surface energies are known experimentally [7]. The size dependent surface energy will be used to refine the size dependent oxidation model and establish the likelihood of catalyst deactivation via oxidation.

4.2 Methodology

4.2.1 Surface energy calculations

Two methods were used for the surface energy determination: the simple classical electrostatics model and the more accurate DFT+U model. The simplicity of the classical model allows for the calculation of energies for cubes comfortably up to 20 nm. The DFT method on the other hand can calculate accurate surface energies for slab systems. In this work a combination of the two methods will be used to determine size dependent surface energies of small CoO crystallites. The surface energies were calculated according to the methodology discussed in Chapter 2. A surface atom is distinguished from bulk atoms on the basis of lower coordination only. The

total number of surface atoms in the slab or crystal is used for the surface energy determination.

4.2.2 DFT calculations

DFT+U calculations were performed on bulk CoO and a CoO(100) surface with a 3D periodic slab model using VASP (see Section 2.5 for details on standard calculation setup). The study of the bulk properties was performed using PW91-GGA PAW potentials. Due to the fact that CoO is an insulator, a small Gaussian smearing with $\sigma = 0.01\ eV$ was used to ensure a correct physical description by avoiding a partial filling of the electronic bands.

The DFT+U method [20, 26] was used according to the implementation of Dudarev *et al.* [27]. For a more detailed view on the implementation of this method within VASP, see discussion by Rohrbach *et al.* [28]. In the Dudarev implementation, the important parameter is the value of $U_{eff} = (U - J)$ which determines the magnitude of the correlation interaction

$$E^{GGA+U} = E^{GGA} + \frac{U-J}{2}\sum_{\sigma}\left[\left(\sum_{m} n^{\sigma}_{m,m}\right) - \left(\sum_{m,m'} n^{\sigma}_{m,m'}, n^{\sigma}_{m',m}\right)\right]. \tag{4.2}$$

The U and J parameters are the spherically averaged matrix elements of the on-site Coulomb interactions [21] and n is the on-site 3d-orbital occupation matrix obtained by projection of the wave function on to $3d$ atomic orbitals. The different $3d$ orbitals are denoted by m or m' = -2, -1, 0, 1, 2, while the up- or down-spin is given by σ. The PAW potentials allow the convenient projection of the wave functions onto the spherical harmonics/orbitals of the atoms. In this formulation the calculations are insensitive to the value of J for a given U_{eff} between 0 and 10 eV. A value of $J = 1\ eV$ was used for all DFT+U calculations.

A calculation with $U_{eff} = 0\ eV$ gives the result with no correction and the same properties as the standard DFT PW91-GGA calculation. The ex-

act U_{eff} value required to describe CoO is not known explicitly and is a function of the particular system studied. Anisimov *et al.* [20] used "constrained Density Functional Theory" to calculate a value of 6.9 eV for U_{eff} for CoO. They reported an empirical $U_{eff} = 4.9\ eV$ to obtain a good representation of the band gap for CoO. The values calculated by Anisimov *et al.* [20] predicted band gaps larger than seen experimentally. Wang *et al.* [21] parameterized U_{eff} based on the oxidation energies and obtained a value of 3.3 eV for CoO. This value for U_{eff} predicted a smaller than observed band-gap of 2.5 eV for CoO [29]. CoO has a fundamental band gap of 2.5 eV and an optical band gap of 2.7 eV as reported by Tran *et al.* [30]. The value for U_{eff} was parameterized by bulk optimization calculations and varied between 0 and 10 eV to find the value of U_{eff} which gives good agreement with experimental results.

This setup along with a Monkhorst-Pack [31] k-point grid of $13 \times 7 \times 9$ gave a good description of the bulk with the energy converged to within 2 meV per cubic unit cell containing four cobalt and four oxygen atoms. A cut-off energy of 550 eV was required for the PAW-GGA potentials to converge the energy to within 10 meV per unit cell. Calculations on the bulk system were performed using a unit cell, which can accommodate the AFMII unit cells (see Figure 4.2).

The DFT slab calculations were performed on the square CoO(100) surface with a p(1×2) surface unit cell. The slab thickness was varied from two to eight layers with each layer containing two oxygen and two cobalt atoms. For the AFMII structure each layer contains an up- and down-spin cobalt atom. A slab unit cell with a vacuum spacing of 5 layers (10 Å) gave total slab energies converged to within 2 meV. Geometry optimizations for the surface slabs were performed by minimizing the total energy of the slab to within $0.1 \times 10^{-3}\ eV$ and minimizing inter atomic forces to within 0.02 $eV/\AA$.

4.2.3 Classical model

In the simplest theory of cohesion in ionic crystals, it is assumed that the cohesive energy is determined purely by the potential of classical particles at the equilibrium positions in the crystal [32]. Since the positive and negative ions in an ionic crystal are treated as point charges, only the Coulomb interaction is used to describe the cohesion of the crystal. For most highly ionic structures this approach gives a good description of the bulk cohesion. The electrostatic interaction scales with $1/r$ and is thus a long range interaction which decays slowly over distance. At very short inter-atomic distances, the core electrons of the ions in the crystal start to overlap with a resulting Pauli repulsion which acts over a very short range. This repulsive potential can be described by the empirical Born repulsion between neighbouring atoms given by the inverse power nine term B_C/r^9 [33]. The summation of this term is essentially over all atoms j but due to the short range only ions in close proximity to ion i contributes to this interaction. The parameter B_C is the coordination dependent repulsion coefficient which depends on the number of nearest and next-nearest neighbours. Since the inverse power term is simplified to only contain the short range repulsions and not the size or charge of the ions this formulation for repulsion should only be used close to the equilibrium distance r_0 [33]. The energy can be calculated in the general case for any system (finite and infinite) using the classical model as shown in equation 4.3. The summation of the interactions for all ions i with all other ions j in the crystal is performed. The first part is the summation of the Coulomb interactions of ions with charge Z_i and Z_j separated by a distance r_{ij} and a vacuum permittivity ε_0, while the second part gives the short range repulsion as described above. The total electrostatic energy (kJ) for an ionic crystal is given by

$$E^{total} = \sum_i \left[\sum_{j \neq i} \left(-\frac{e^2 Z_i Z_j}{4\pi\varepsilon_0 r_{ij}} \right) + \sum_{j \neq i} \left(\frac{B_C}{r_{ij}^9} \right) \right]. \tag{4.3}$$

This equation can be simplified for an infinite crystal where the summation of all the charges is given by the Madelung constant A_M and is written in terms of the shortest inter-ionic distance r. In this formulation the Madelung constant is simply the sum of the positive and negative charge interactions. The Madelung constant is unique for every crystal structure and can be calculated explicitly by summation of all the ionic charges in the crystal. The electrostatic energy per ion (kJ/mol) in an infinite crystal is then given by

$$E^{bulk} = \left(\frac{e^2}{4\pi\varepsilon_0} \right) \frac{-Z_+ Z_- A_M}{r} + \frac{B_{C-bulk}}{r^9.} \tag{4.4}$$

Due to the fact that the Coulomb interaction scales with $1/r$, the convergence is slow for such an infinite series. If summation is performed incorrectly, this will lead to a diverging series [34]. Various methods for this summation exist [33] but due to its simplicity the Evjen summation scheme was used [35]. The Evjen summation is based on summing over neutral charge groups to avoid the increasing polarization contribution that would result in divergence. In order to achieve this, the summation is performed within a cell where the charge interaction has a weight based on the location within the summation grid. The atoms within the bounding cell have a weight of 1, while the charges at the faces, edges and corners have weights of $\frac{1}{2}$, $\frac{1}{4}$ and $\frac{1}{8}$ respectively for the 3D structures infinite in three dimensions. In the case of a flat sheet or multiple flat sheets, weights of $\frac{1}{2}$ and $\frac{1}{4}$ are used respectively for atoms at the edges or corners of the bounding cell. This approach gives fast converging results for a chain with one infinite dimension, a flat sheet with two infinite dimensions and an infinite 3D structure.

The only unknowns in equations 4.3 and 4.4 are the charge magnitudes

Z_i, Z_j and the effective repulsive interaction B_C. The energy calculated from the classical model is highly dependent on the absolute magnitude of the charge and an accurate charge is therefore required. The bulk repulsive coefficient can be calculated from a given charge at the equilibrium distance by taking the first derivative of the classical expression

$$B_{C-bulk}^{equilibrium} = \left(\frac{e^2}{4\pi\varepsilon_0}\right)\frac{A_M Z_+ Z_- r_0^8}{9}. \tag{4.5}$$

This approach takes care of the electrostatic contribution to bonding. Since bonding consist of an electrostatic and covalent contribution, the covalent contribution must still be included. This can easily be done by using a broken bond approach with nearest neighbouring atoms as demonstrated by Liu *et al.* [8]. In their analysis they did not include the electrostatic contributions which would be necessary for ionic systems.

In order to calculate the surface energy of a slab using the classical approach, the Madelung constant was calculated for CoO(100) surface slabs of various thicknesses. The summation of the Madelung constant for a flat slab which is infinite in two dimensions was performed for slabs of various thickness. In the summation of the Coulomb interactions, the convergence of the Evjen summation was checked for surface atoms and atoms at the centre of the slab. A fast convergence of the Madelung constants was achieved for the slab systems with the two dimensional infinite scheme using the Evjen summation. The number of ions in the summation was checked to ensure a converged value in the same range as the DFT+U calculations.

The charge summation was performed for CoO finite cubes of different sizes. Since these cubes do not have infinite dimensions, the summation was simply performed as in equation 4.3 and the Evjen summation technique was not required. The surface energy of cubes of different sizes could be used to obtain the size dependent behaviour of the surface energy of unrelaxed crystals.

4.3 Results

4.3.1 Bulk CoO

DFT+U calculations were performed on the CoO bulk crystal with the different magnetic phases to demonstrate that the bulk properties are described accurately. Among these properties, the lattice parameter, magnetization and band gap were calculated to compare with experimental results and establish the ability of the DFT+U to describe the system.

The properties were calculated using U_{eff} values ranging from 0 – 10 eV, where a calculation with $U_{eff} = 0$ eV represents the standard DFT approach. A DFT+U calculation with a non-magnetic electronic state did not produce a band gap for a U_{eff} between 0 and 10 eV. The AFMII structure, however, did produce a band gap for $U_{eff} > 1$ eV. A value of $U_{eff} = 5$ eV gave a band gap of 2.55 eV and in good agreement with the measured gap of 2.5 eV. The DOS is shown in Figure 4.3 for the AFMII and the non-magnetic phases with values for U_{eff} of 0 and 5 eV indicating that the correct band gap is only obtained for the AFMII structure with an appropriate value for U_{eff}.

A value for $U_{eff} = 5.9$ eV was determined by Anisimov *et al.* [20], by using a constrained-DFT method [36]. This calculation gave a band gap of 3.1 eV along with a spin moment of 2.63 μ_B. Anisimov *et al.* [20] suggested an empirical value for $U_{eff} = 4.9$ eV to obtain the correct band gap. The optimized lattice parameters for these calculations were not reported.

The volume was optimized for the unit cell shown in Figure 4.2 which can incorporate the AFMII magnetic state. This unit cell can easily be compared with the AFMII cell suggested by Jauch *et al.* [11]. The correct lattice distortion below the Neél temperature [11] is predicted when using $U_{eff} = 5$ eV. When comparing the calculated volume to the experimentally measured volume, the DFT+U method predicts a larger unit cell for all

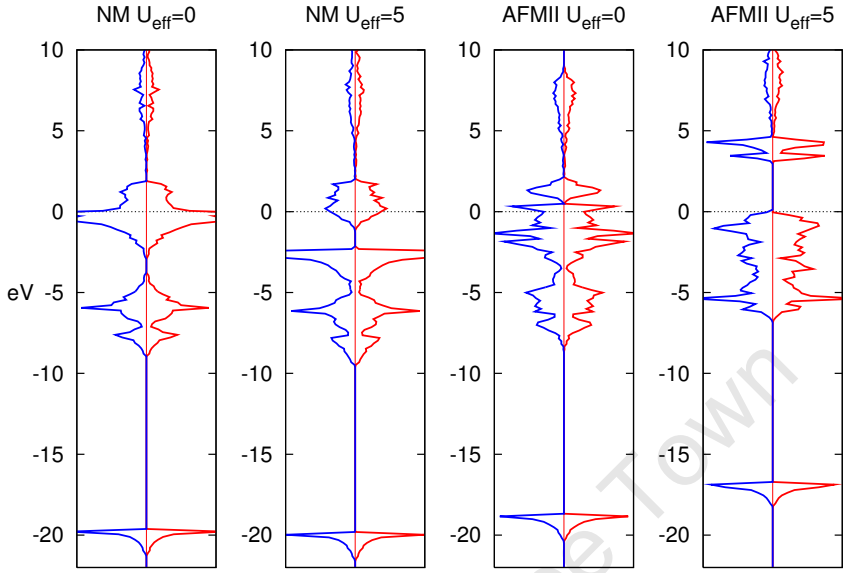

Figure 4.3: DOS of non-magnetic and AFMII phases calculated using the DFT+U formulation with different U_{eff} values in eV. The highest occupied electronic level (Fermi level) is at 0 eV.

$U_{eff} > 2\ eV$ with the value of $U_{eff} = 5\ eV$ in error with experiment by 2.25 %. The lattice parameters of $U_{eff} = 5\ eV$ are in good agreement with those reported by Jauch *et al.* [11] giving a maximum error of 0.07 Å along the diagonal C-axis used by Jauch. A DFT+U calculation with the non-magnetic phase gave an undistorted cubic unit cell with a lattice parameter of 4.093 Å. The calculated volme for the non-magnetic phase is in error by 11.35 % relative to the experimental volume for the AFMII phase as measured by Jauch *et al.* [11].

The magnetization increases slightly with an increase in U_{eff}. A value of 2.69 μ_B was obtained for $U_{eff} = 5\ eV$, which is in good agreement with other calculations [20, 21, 37]. An experimental value of 3.5 μ_B was reported by van Laar [38] and includes an orbital spin of 1 μ_B.

The effective Bader charge increases slightly with U_{eff} suggesting that

Table 4.1: Bulk properties calculated using the DFT+U approach for the AFMII phase.

U_{eff}	Volume Å^3	Band gap eV	Magnetization[a] μ_B	Charge[b] e
0	73.40	0.00	2.32	1.23
1	76.74	0.00	2.46	1.27
2	77.36	0.42	2.53	1.30
3	78.09	1.55	2.61	1.30
4	78.78	2.21	2.66	1.32
5	78.51	2.55	2.69	1.31
6	78.73	3.55	2.76	1.35
7	78.74	4.05	2.79	1.35
8	78.71	4.55	2.83	1.36
9	78.81	5.05	2.87	1.36
10	78.14	5.07	2.90	1.36
Exp.	76.78[c]	2.50[d]	3.50[e]	.

[a] Magnetization given by the PAW projections

[b] Effective charge in electrons per cobalt atom calculated using the Bader analysis

[c] Volume measured for AFMII structure at 10 K [11]

[d] Band gap found by van Elp *et al.* [29]

[e] Magnetization reported by van Laar [38] includes the orbital spin component of 1 μ_B

the charge transfer between cobalt and oxygen increases with increasing U_{eff}. The charge calculated at $U_{eff} = 5\ eV$ is 1.31 e and is in between the value of 1.2 e reported by Sasaki *et al.* [39] from X-ray experiments and 1.48 e reported by Jauch and Reehuis [40] from γ-ray experiments. Other DFT studies [20, 21, 37] did not report on the effective charge.

From the DFT+U results discussed here, only the AFMII magnetic state can describe the experimentally measurable properties of CoO. This fits with the suggestions [17, 41] that for the para-magnetic structure, the magnetization remains on the atomic sites, while the long range magnetic order is lost. The AFMII phase is thus the most promising model for describing the properties of CoO.

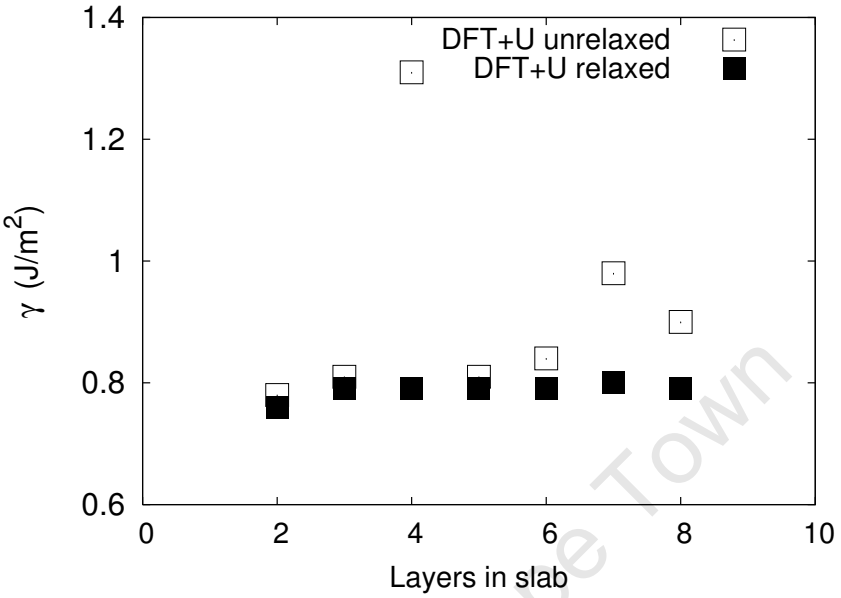

Figure 4.4: Surface energies calculated from DFT+U method with $U_{eff} = 5\ eV$.

4.3.2 DFT Surface energy

The CoO bulk structure can be most reliably predicted using DFT+U calculations with $U_{eff} = 5\ eV$. This value was used for surface slabs by minimizing the forces and total energy through relaxation of all ions in the slab. The surface unit cell was created by cleaving the bulk optimized unit cell along the CoO(100) plane. The surface relaxations were minimal when using the DFT+U approach with the oxygen atoms only moving outwards slightly by 0.01 Å relative to the cobalt atoms. This minimal relaxation was also reported by Felton *et al.* [42], Prutton *et al.* [43] and Brookes *et al.* [44] where the CoO(100) surface was found to remain essentially a bulk cut with relaxation less than 3 %. STM results on CoO(100) [45] showed that the surface has very minor relaxations and is essentially a bulk termination of the crystal as predicted from DFT+U.

The surface energy was calculated for surfaces with various thicknesses

ranging from 2 to 8 layers. The Boettger method [46] was used to calculate the surface energies with a bulk energy as suggested by Fiorentini and Methfessel [47]. The Boettger-Fiorentini method gave a bulk energy which was lower by 10 meV per CoO unit than the bulk DFT+U calculation for the relaxed unit cell. This suggests that the effect of polarization from geometric changes is small for this surface unit cell.

The DFT+U surface energies are given as a function of the slab thickness in Figure 4.4. The surface energy calculated for CoO of 0.79 J/m^2 (49 $meV/\AA^2$) is in good agreement with the 0.78 J/m^2 (49 $meV/\AA^2$) calculated for NiO(100) using the DFT+U approach [48].

The LDA and GGA level of theory is unable to directly predict the correct surface energies (see Chapter 2). The intrinsic surface energy error correction is thus required since this error is not corrected for by DFT+U and is a separate failure of the GGA functionals. The error scales with density and the bulk density can be used to correct the surface energy [23]. The bulk electron density of CoO was calculated to be 0.776 $e/\AA^3$. This density would require a substantial surface energy correction of 0.78 J/m^2. This large correction of surface energy is very surprising since the correction is of similar magnitude to the actual calculated surface energy. This surprising result will be compared with DFT surface energies of other well studied ionic crystals such as NaCl [49], and MgO [50] as well as NiO [48] (see Table 4.2). The intrinsic surface energy correction by Mattsson *et al.* [23] was applied for all calculated results using bulk electron densities of 0.179, 0.428, 0.883 and 0.776 $e/\AA^3$ for NaCl, MgO, NiO and CoO respectively. Depending on the exchange-correlation potential used in the calculations and the electron density, the intrinsic surface energy correction would differ. The experimental surface energies for NaCl and MgO have been reported in literature previously [7, 49].

The compiled results for the ionic species in Table 4.2 suggest that the

Table 4.2: Surface energies (J/m^2) reported in literature for ionic material for which the surface energies are well established. In all cases the intrinsic surface energy correction was applied based on the functional used and the valence electron densities.

Structure	Method	Energy	Correction	Surface energy
NaCl	PBE	0.14[a]	0.15	0.29
	LDA	0.23[a]	0.06	0.29
	Exp			0.28[a]
MgO	PBE	0.87[b]	0.38	1.25
	LDA	1.17[b]	0.15	1.31
	Exp			1.00-1.30[c]
NiO	PW91	0.77[d]	0.87	1.64
	B3PW	1.38[e]		
CoO	PW91	0.77[f]	0.78	1.55

[a] Experimental results summarized by Li *et al.* [49].

[b] DFT calculations by Finocchi and Goniakowski [50]

[c] Experimental results reported by Overbury [7] at 77 K

[d] DFT+U calculations using U_{eff}=6.3 eV by Rohrbach *et al.* [48]

[e] DFT calculation with exact exchange [51] should give more reliable surface energies

[f] Own DFT+U surface calculations using optimized unit cell and atomic coordinates

intrinsic surface error must be corrected by applying the intrinsic surface energy correction [23] for NaCl and MgO. The DFT results corrected for the intrinsic surface energy error resulting form LDA- and GGA-DFT are in good agreement with experimentally determined values. The surface energy correction is thus required for simple ionic crystals such as NaCl and MgO as well. The same correction was applied to the NiO DFT+U surface energy. Unfortunately experimental surface energies could not be found, but a hybrid-GGA calculation gave a surface energy of 86 $meV/\AA^2$ (1.38 J/m^2) [51]. Since the hybrid-GGA functionals make use of exact exchange the surface energy is much more accurate than just simply a GGA calculation. Unfortunately this method does not include the exact electron

correlation energy but the surface energy confirms that the intrinsic surface energy correction should be included for DFT+U systems as well. The corrected surface energy for CoO was found to be 1.55 J/m^2 for infinite flat CoO surfaces and will be used in the remainder of this chapter.

Charge analysis from DFT results

The DFT+U calculations gave an effective Bader ionic charge for bulk ions of 1.31 e which is similar to the ionic charge in a slab. The formal charge for CoO is 2 e but experimentally determined charges of 1.2 e [39], 1.48 e [40] have been reported previously. Computational studies suggested Mulliken charges ranging from 1.55–1.68 e [52]. There is thus no clear link between the Bader and Mulliken charges.

Bredow calculated Mulliken charges for MgO, NiO and CoO using standard DFT and hybrid-DFT approaches. Unfortunately DFT+U was not used in this comparison and a direct comparison of the results can thus not be done. B3LYP calculations gave the most promising results for band-gaps and Mulliken charges of 1.78, 1.67 and 1.68 e for MgO, NiO and CoO respectively [52]. There was, however, no consistency between Mulliken charges calculated from Hartree-Fock, B3LYP and GGA methods.

A Bader charge analysis of the surface slabs calculated using the DFT+U approach indicated that the charge remains 1.32 e per atom throughout the slab. The maximum deviation is 0.02 e per atom, suggesting that the charge remains essentially constant throughout the slab. This shows that the creation of a surface from bulk CoO does not affect the charge localization on the surface or bulk atoms. DFT calculations on NaCl [49] reported Mulliken charges of 0.54 e on the bulk NaCl ions and charges of 0.61 and -0.59 e for the surface Na^+ and Cl^- ions respectively. It is not clear whether the Bader and Mulliken analysis would give similar results for the NaCl surface slabs due to the different approach of partitioning the charge density into ionic charge

per ion. The Bader analysis has a more sound basis for the calculation of effective charges and only Bader charges will be considered.

This constant effective charge and minimal surface reconstruction or relaxation for CoO slabs allows a simple classical approach to calculate the electrostatic contribution to the surface energy. All the CoO ions can be treated as point charges in the classical formulation and the point charges have the same charge magnitude of 1.32 e.

4.3.3 Classical analysis of surface energies for CoO

The classical electrostatics model was used to determine the electrostatic contribution to the surface energy of CoO(100). Since this model is highly dependent on the effective charge used, the energies were calculated for various partial charges. The repulsion constant was calculated as shown in equation 4.5 from the equilibrium lattice parameter and the partial charge. The surface energy was calculated as described in Chapter 2, where the bulk energy was calculated using the bulk Madelung constant for an ideal CoO crystal at the bulk lattice parameter. The slab energy was calculated using the Madelung constant for slabs of various thicknesses and a reduced repulsion interaction of surface atoms with a lower coordination.

The energies calculated for the flat slabs are given for the different effective charges (see Figure 4.5). The classical approach shows that by taking into account only the charge interactions, the surface energy is converged within three layers. Additional layers would not affect the surface energy. This suggests that for a three layer slab which extends to infinity, the long range charge interactions are mostly "saturated" by the in-sheet interactions of the infinite sheet. The long range interactions perpendicular to the infinite sheet are "saturated" once a "bulk" and "surface" sheet can be distinguished.

The electrostatic component of the surface energy was calculated to be

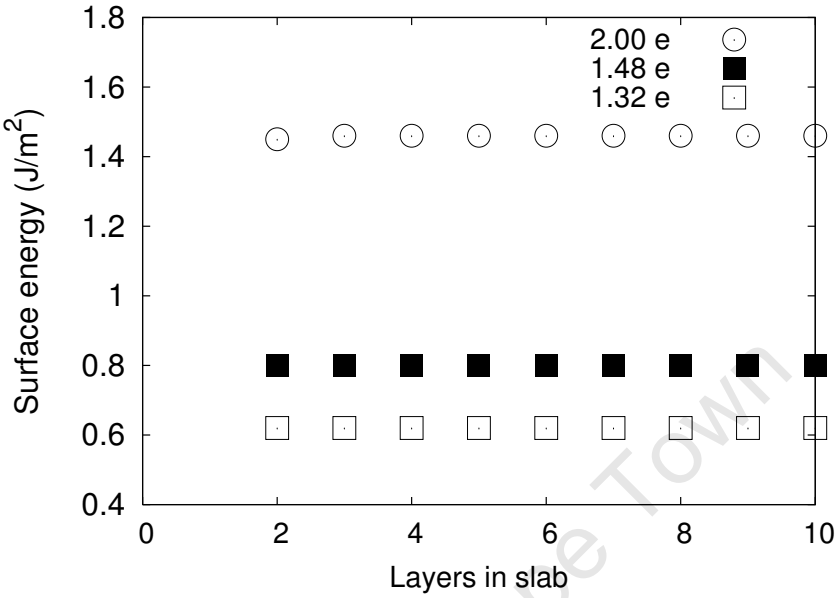

Figure 4.5: Surface energies calculated from classical electrostatics model using different effective charges.

0.62 J/m^2 (17.3 kJ/mol) when using a charge of 1.32 e (found from the DFT+U calculations), which is significantly less than the surface energy calculated with the intrinsic error corrected DFT+U value. A surface energy of 1.45 J/m^2 is found when using an effective charge of 2 e, which is close to the 1.55 J/m^2 calculated using DFT+U and the intrinsic surface energy correction. A previous classical model suggested a surface energy for the NiO(100) surface of 1.39 J/m^2 and 1.17 J/m^2 for MgO when using an effective charge of 2 e [53]. This apparent good agreement with corrected DFT+U results is considered to be fortuitous since bonding in ionic material can not be described by a purely ionic interaction. The covalent energy contribution of broken Co–O bonds on the surface should be included with the ionic contribution of the surface energy to obtain an accurate value for the surface energy.

The covalent or broken bond interactions with nearest neighbours are

neglected in the classical electrostatics approach. The covalent contribution of the broken bond energy was estimated by taking the difference of the real surface energy and the electrostatic surface energy. The surface energy for CoO (1.55 J/m^2) gives a total surface energy per atom of 42.3 *kJ/mol surface atoms*. For a flat slab, the electrostatic contribution of the surface energy per surface atom is 17 *kJ/mol surface atoms*. The Co–O bonding energy required to obtain the surface energy of 1.55 J/m^2 is thus 25.3 *kJ/mol surface atoms*. The large broken bond energy suggests that there is a substantial covalent contribution to the bonding and surface energy. The broken bond energy was not compared with other ionic compounds such as MgO, NaCl and NiO since Bader charges are not available.

4.3.4 Size dependent surface energy

The size dependent energy is determined by calculating the surface energy for different sized finite cubes of CoO. Since the cubic crystals are not infinite, all charge interactions can be calculated exactly for a cube of a given size (see equation 4.3). The surface energies for cubes of different sizes were calculated as discussed in Chapter 2 where the total energy for the cube is the finite energy in equation 2.16. The contribution of the broken bonds are also included for the surface atoms. The flat (100) surface atoms have one broken bond, while the ridge atoms have two and the crystal tip atoms have three; each broken bond with a contribution of 25.3 *kJ per bond* to the surface energy.

The surface energy of the cubes are given as a function of the diameter of a sphere with a similar volume (see Figure 4.6). Below a diameter of 5 nm, the surface energy increases significantly due to the reduced Madelung interaction. Although the surface energies for cubes above 5 nm are similar when using a charge of 2 e and 1.3 e with broken bonds, the behaviour is different for smaller crystallites. When using a charge of 2 e, the surface energy has

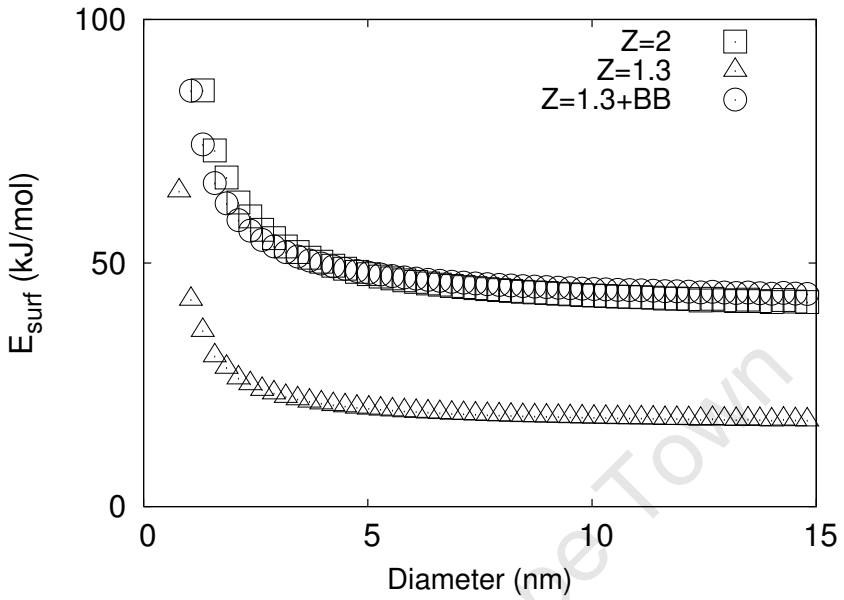

Figure 4.6: Size dependent surface energies (in kJ/mol surface atoms) calculated for cubes of different sizes with CoO(100) faces exposed using a charge of 2 e without broken bond energies and 1.3 e with and without broken bond energies included.

a strong size dependence for small cubes resulting in a substantial increase in the surface energy of small crystallites. The more realistic approach of using a charge of 1.3 e along with the broken bond energy has a weaker size dependence below 5 nm. Due to the smaller charge, the size dependence of the surface energy is weaker. Since the majority of surface atoms only have one broken bond, the broken bond energy contribution is almost a constant addition to the magnitude of the energy and therefore has a minor effect on the size dependence.

4.4 Discussion

4.4.1 Calculating properties of CoO

The standard DFT calculations are not able to predict the correct structure and electronic states for CoO. The DFT+U calculations were used to account for the strong correlation interactions which are important when calculating the properties of CoO. In the case of CoO this electronic state with a band gap is inherently linked to the anti-ferromagnetic nature of this Mott insulator. This has been shown here from the results for the non-magnetic and AFMII magnetic phases from DFT+U calculations. Only the AFMII phase gave the experimentally observed band gap of 2.5 eV when a $U_{eff} = 5\ eV$ was used. The DFT+U calculations were in agreement with the lattice distortion found for the AFMII phase. For the non-magnetic phase, all the DFT and DFT+U calculations gave a significantly smaller volume than observed experimentally.

The operating temperature for the Co-based Fischer-Tropsch synthesis is above the Néel temperature of 291 K for CoO thus the para-magnetic phase should be calculated. In a para-magnetic phase, the spin moments are not aligned any more and therefore the total magnetization is zero, but short range magnetic order still exists, which is a prerequisite for the formation of a band gap. Due to short range magnetization, the band gap is still present for the para-magnetic phase and the AFMII phase is the only that produce this electronic and magnetic state. The most reasonable description of the para-magnetic phase is thus given by an AFMII calculation using the DFT+U approach.

4.4.2 Surface energies

The surface energy for the CoO(100) surface was calculated for the optimized AFMII crystal structure. The results for the standard DFT and the DFT+U

method (with $U_{eff} = 5\ eV$) were compared. The DFT+U result agrees very well with the experimental LEED [42, 43] and STM [45] work on CoO and other Mott insulators. A closer look a the DFT+U charge distribution using the Bader analysis showed that the maximum variation in charge throughout the slab is less than 0.02 e per atom with an effective charge located at the atomic sites of 1.32 e. The standard deviation of the charges throughout the slab was 0.009. The Bader charge is substantially less than the value of 1.48 e determined by Jauch and Reehuis [40].

A (corrected) surface energy per unit area of $\gamma = 1.55\ J/m^2$ was calculated for the CoO(100) surface. This translates to a surface energy of $E_{surf} = 42.3\ kJ/mol\ surface\ atoms$. Comparison with other ionic compounds suggests that correcting for the intrinsic surface energy error improves the results for surface energies substantially. The intrinsic surface energy correction was applied to account for the incorrect description of the exponential decay of electron density into the vacuum by LDA and GGA potentials. The corrected CoO surface energy is substantially higher than the value of 0.46 J/m^2 initially predicted by the classical analysis of van Steen *et al.* [5].

It is thus clear that an ionic treatment of the surface energies must be considered carefully. The classical energies could easily be calculated from a Madelung approach since the crystal structure shows minimal relaxations and all the ions are essentially at their equilibrium positions. The classical surface energy calculated using a charge of 1.31 e (from DFT+U results) is substantially less than the DFT+U surface energy. This is consistent with the classical view that bonding has an ionic and covalent contribution. The covalent contribution was estimated to be 25.3 *kJ per broken bond* of a CoO(100) surface. This is the contribution of one Co–O broken bond. This classical approach can thus be used in the calculation of size dependent surface energies of a CoO cube. The size dependent surface energies were

calculated using this combination of classical electrostatics and broken bond picture.

4.5 Conclusions

A systematic investigation of the properties of CoO using a DFT+U approach, showed that the best agreement with the experimentally observed properties can be found using a $U_{eff} = 5\ eV$. This formulation gives a band gap for the Mott insulator of 2.55 eV which is close to the experimental value of 2.5 eV. The AFMII magnetic phase was the only phase that gave reasonable results for all the known properties of CoO. This approach gave good results for the lattice parameter compared to the experimental values and an effective Bader ionic charge of 1.31 e.

The calculated DFT+U surface energy was corrected for the intrinsic surface energy error inherent in LDA and GGA-level calculations. This correction showed consistent improvement of DFT surface energies for NaCl, MgO and NiO. The final surface energy calculated for CoO(100) is 1.55 J/m^2 (42.3 *kJ/mol surface atoms*). This value is substantially larger than 0.45 J/m^2 estimated previously [5].

The surface structures were calculated and found to have minimal relaxation of the surface atoms. The change in effective charge per atom throughout the slab was minimal and the classical electrostatics approach can therefore be used to calculate the surface energies with a Bader charge of 1.31 e. The purely electrostatic surface energy is only 0.62 J/m^2 and the covalent component (broken bonds) were also included. The broken bond energy was estimated to be 25 *kJ per broken bond*.

The size dependent surface energy was calculated for cubic crystals using the classical approach to determine the electrostatic and broken bond energy contributions. The surface energy was found to increase sharply below 5 nm and have a much stronger size dependence than previously estimated [5].

References

[1] Schanke, D., Hilmen, A.M., Bergene, E., Kinnari, K., Rytter, E., Ådnanes, E., Holmen, A., Catal. Lett. 34 (1995), 269.

[2] Iglesia, E., Appl. Catal. A: General 161 (1997), 59.

[3] Schultz, H., Nie, Z., Ousmanov, F., Catalysis Today 71 (2002), 351.

[4] van Berge, P.J., van de Loosdrecht, J., Barradas, S., van der Kraan, A.M., Catal. Today 58 (2000), 321.

[5] Van Steen, E., Claeys, M., Dry, M.E., van de Loosdrecht, J., Viljoen, E.L., Visagie, J.L., J. Phys. Chem. B 109 (2005), 3575.

[6] van de Loosdrecht, J., Balzhinimaev, B., Dalmon, J.-A., Niemantsverdriet, J.W., Tsybulya, S.V., Saib, A.M., van Berge, P.J., Visagie, J.L., Catal. Today 123 (2007), 293.

[7] Overbury, S.A., Bertrand, P.A., Somorjai, G.A., Chem. Rev. 75 (1975), 547.

[8] Liu, W., Liu, X., Zheng, W.T., Jiang, Q., Surf. Sci. 600 (2006), 257.

[9] Brandow, B.H., Adv. Phys. 26 (1977), 651. ‘

[10] Smart, J.S., Greenwald, S., Phys. Rev. 82 (1951), 113.

[11] Jauch, W., Reehuis, M., Bleif, H.J., Kubanek, F., Pattison, P., Phys. Rev. B 64 (2001), 052102.

[12] Zaanen, J., Sawatzky, G.A., Allen, J.W., Phys. Rev. Lett. 55 (1985), 418.

[13] Terakura, K., Williams, A.R., Oguchi, T., Kübler, J., Phys. Rev. Lett. 52 (1984), 1830.

[14] Golosovsky, I.V., Mirebeau, I., André, G., Tovar, M., Tobbens, D.M., Kurdyukov, D.A., Kumzerov, Y.A., Phys. of the Solid State 48 (2006), 2130.

[15] Anderson, R.B., “The Fischer-Tropsch Synthesis”, Academic Press, Inc., 1984.

[16] Shull, C.G., Strauser, W.A., Wollan, E.O., Phys. Rev. 83 (1951), 333.

[17] Mott, N.F., Zinamon, Z., Rep. Prog. Phys. 33 (1970), 881.

[18] Kernavanois, N., Ressouche, E., Brown, P.J., Henry, J.Y., Lelièvre-Berna, E., J. Phys.: Cond. Matter. 15 (2003), 3433.

[19] Terakura, K., Oguchi, T., Williams, A.R., Kübler, J., Phys. Rev. B 30 (1984), 4734.

[20] Anisimov, V.I., Zaanen, J., Andersen, O.K., Phys. Rev. B 44 (1991), 943.

[21] Wang, L., Maxisch,T., Ceder, G., Phys. Rev. B 73 (2006), 195107.

[22] Mattsson, A.E., Kohn, W., J. Chem. Phys. 115 (2001), 3441.

[23] Mattsson, A.E., Armiento, R., Schultz, P.A., Mattsson, T.R., Phys. Rev. B 73 (2006), 195123.

[24] Tasker, P.W., J. Phys. C Solid State Phys. 12 (1979), 4977.

[25] Noguera, C., J. Phys. Cond. Matt. 12 (2000), R367.

[26] Leichtenstein, A.I., Anisimov, V.I., Zaanen, J., Phys. Rev. B 52 (1995), R5467.

[27] Dudarev, S.L., Botton, G.A., Savrasov, S.Y., Humphreys, C.J., Sutton, A.P., Phys. Rev. B 57 (1998), 1505.

[28] Rohrbach, A., Hafner, J., Kresse, G., J. Phys.: Cond. Matt. 15 (2003), 979.

[29] Van Elp, J., Wieland, J.L., Eskes, H., Kuiper, P., Sawatzky, G.A., de Groot, F.M.F., Turner, T.S., Phys. Rev. B 44 (1991), 6090.

[30] Tran, F., Blaha, P. Schwarz, K.,Novák, P., Phys. Rev. B 74 (2006), 155108.

[31] Monkhorst, H.J., Pack, J.D. Phys., Rev. B 13 (1976), 5188.

[32] Ashcroft, N.W., Mermin, N.D., "Solid State Physics", Thompson Learning, Inc., 1976.

[33] Sherman, J., Chem. Rev. 11 (1932), 93.

[34] Borwein, D., Borwein, J.M., Taylor, K.F., J. Math. Phys. 26 (1985), 2999.

[35] Evjen, H.M., Phys. Rev. 39 (1932), 675.

[36] Gunnarsson, O., Andersen, O.K., Jespen, O., Zaanen, J., Phys. Rev. B 39 (1989), 1708.

[37] Szotek, Z., Temmerman, W.M., Winter, H., Phys. Rev. B 47 (1993), 4029.

[38] van Laar, B., Phys. Rev. 138 (1965), A584.

[39] Sasaki, S., Fujino, K., Takeuchi, Y., Proc. Japan Acad. 55 Ser. B (1979), 43.

[40] Jauch, W. Reehuis, M., Phys. Rev. B 65 (2002), 125111.

[41] Isaak, D.G., Cohen, R.E., Mehl, M.J., Singh, D.J., Phys. Rev. B 47 (1993), 7720.

[42] Felton, R.C., Prutton, M., Tear, S.P., Welton-Cook, M.R., Surf. Sci. 88 (1979), 474.

[43] Prutton, M., Walker, J.A., Welton-Cook, M.R., Felton, R.C., Ramsey, J.A., Surf. Sci. 89 (1979), 95.

[44] Brookes, N.B., Law, D,S-L., Warburton, D.R., Wincott, P.L., Thornton, G., J. Phys.: Cond. Matt. 1 (1989), 4267.

[45] Castell, M.R., Dudarev, S.L., Briggs, G.A.D., Sutton, A.P., Phys. Rev. B 59 (1999), 7342.

[46] Boettger, J.C., Phys. Rev. B 49 (1994), 16798.

[47] Fiorentini, V., Methfessel, M., J. Phys.: Cond. Matt. 8 (1996), 6525.

[48] Rohrbach, A., Hafner, J., Kresse, G., Phys. Rev. B 69 (2004), 075413.

[49] Li, B., Michaelides, A., Scheffler, M., Phys. Rev. B 76 (2007), 075401.

[50] Finocchi, F., Goniakowski, J., Surf. Sci. 601 (2007), 4144.

[51] Cinquini, F., Giordano, L., Pacchioni, G., Ferrari, A.-M., Pisani, C., Roetti, C., Phys. Rev. B 74 (2006), 165403.

[52] Bredow, T., Gerson, A,R., Phys. Rev. B 61 (2000), 5194.

[53] Oliver, P.M., Parker, S.C., Mackrodt, W.C., Mod. Simul. Mater. Sci. Eng. 1 (1993), 751.

Chapter 5

Size Dependent Deactivation

5.1 Introduction

The fundamental concepts of deactivation were discussed in Chapter 1. Deactivation can occur as a result of a change in the intrinsic activity of the catalyst, reduction in the number of active sites or blockage of the pathways in which the gas phase molecules contact the surface. The origin of these processes is either physical, chemical or thermal. For most of these processes, the driving force for deactivation is linked either to thermodynamics of the system or mechanical strength of the catalyst and hydrodynamic behaviour inside the reactor.

The optimal activity per mass of active metal can be achieved by using highly dispersed metal crystallites. For a highly dispersed catalyst the number of active sites per mass of catalyst is at a maximum. In the previous two chapters the surface energies for small crystallites were shown to increase with crystallite size. For small crystallites, the contribution of the surface energy to the chemical potential becomes significant. This thermodynamic destabilization of small crystallites is a driving force for various deactivation mechanisms. The thermodynamic stabilization of small crystallites can either be facilitated by reducing the dispersion through a sintering mechanism or via a phase change to the oxide phase. Other possibilities of deactivation also exist where blockage of the active sites can occur via support creep in an attempt of the crystallite to lower the surface energy. The increase of the chemical potential of small crystallites can also reduce the barrier for the formation of carbonyls, atomic cobalt or mobile species on the support surface.

A thermodynamic approach in which size dependent properties are included was used as a first step to understanding deactivation via sintering and oxidation at a fundamental level. Useful information can be gained without much knowledge of the support interaction by just looking at the stability of ideal nano-crystallites.

5.2 Sintering as deactivation mechanism

Sintering is the loss of catalytically active surface area due to a decrease in dispersion. This is a result of the increase in average crystallite size of the catalytic material [1, 2]. The average crystallite size increases when smaller crystallites coalesce to form large crystallites, resulting in a decrease in dispersion and a smaller surface area [3]. The increase in average crystallite size would result in fewer surface atoms with a low coordination exposed at the surface of a crystallite. Consequently the chemical potential of a crystallite would decrease for larger crystallites due to the reduced contribution of the surface energy. The reduction of the chemical potential with an increase in size is the driving force for sintering.

In Chapter 3 the size dependent surface energies were calculated for various nano-sized crystallites of cobalt. The driving force and possible pathways for sintering can now be discussed based on the thermodynamic analysis which includes size dependent surface energies. The thermodynamic expression for the size dependent chemical potential of a nano-sized crystallite relative to the bulk is given in terms of the size dependent surface energy (per surface atom) and dispersion (see Appendix A.2 for derivation). The size dependent chemical potential $\mu_s(T, P, D)$ is given as a function of the bulk chemical potential $\mu_s(T, P)$, the surface energy per surface atom (E_{surf}) and the dispersion (D_s) as a function of a size parameter m of nano-sized crystallites.

$$\mu_s(T, P, D) = \mu_s^0(T, P) + E_{surf}(m)D_s(m) \tag{5.1}$$

The size-dependent chemical potential (see Figure 5.1) shows that smaller crystallites are less stable (per mol) than large crystallites. For large crystallites the contribution of the surface energy is negligible and close to the bulk chemical potential. Due to the ever present thermodynamic driving

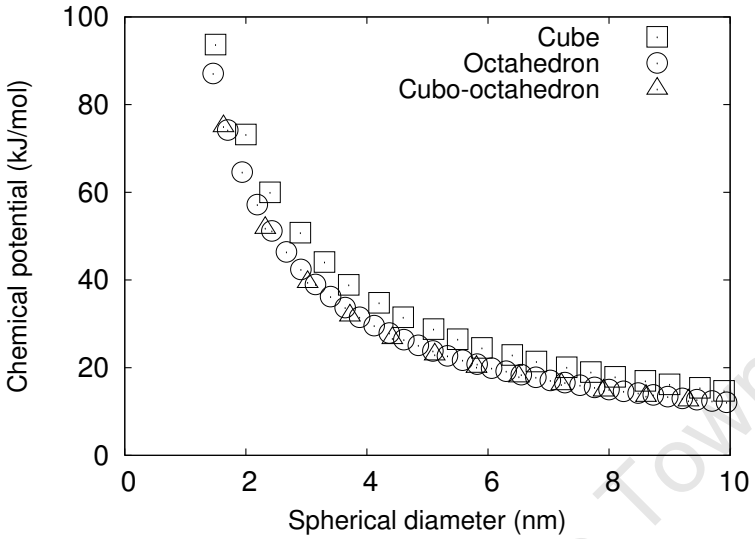

Figure 5.1: Size dependent chemical potential of various nano-sized crystallites indicating the decrease in stability of smaller crystallites.

force, the effect of sintering can not be avoided completely for nano-sized catalysts. This driving force becomes weaker for larger crystallites and the rate of deactivation would slow down for larger crystallites. As long as the dispersion can be reduced via crystallite growth, the driving force for sintering would be present. Deactivation via sintering is usually described by an asymptotic decay over time on stream [1, 4]. Sintering via coalescence is usually a result of Brownian motion. Consequently, the rate of sintering can be described by a power law rate expression [5].

Various mechanisms of sintering have been proposed which can be divided into two main categories [4]:

- The coagulation process with crystallite growth by migration [6] and coalescence [7, 8] of other crystallites.

- The ripening process with growth via inter particle transport [9, 10]

of mobile species of the active metal. These mobile species are either atomic or molecular depending on the stability of the mobile species and the gas phase conditions. The inter particle transport mechanism is known as Ostwald ripening and is characterized by larger crystallites growing at the expense of smaller crystallites.

An understanding of the parameters affecting the sintering process is required in order to minimize the deactivation resulting from sintering. Twelve complex physiochemical processes were suggested by Bartholomew [2] to affect sintering:

1. dissociation and emission of metal atoms or metal containing molecules from crystallites,
2. adsorption and trapping of metal atoms or metal containing atoms on the support surface,
3. diffusion of metal atoms, metal-containing atoms and/or metal crystallites across support surfaces,
4. metal or metal oxide particle spreading,
5. support surface wetting by metal or metal oxide particles,
6. metal particle nucleation,
7. coalescence of or bridging between two metal particles,
8. capture of atoms or molecules by metal particles,
9. liquid formation,
10. metal volatilization through volatile compound formation,
11. splitting of crystallites in O_2 atmosphere due to formation of oxides of a different specific volume,

12. metal atom vaporization.

Liquid formation, metal dissociation, vaporization and metal volatilization are affected by the chemical potential of the metal. The other interactions are controlled by the metal-support interaction or kinetic processes such as diffusion.

In a typical system, sintering via coalescence or ripening can be possible depending on the active metal [2], gas phase conditions [11], support interaction [12], temperature [3] and crystallite size as will be discussed here. These parameters affect the mechanistic pathways in different ways.

The main difference between the two mechanisms lies in how the crystallite size distribution changes. Pure crystallite diffusion results in small crystallites coalescing to form larger crystallites. For a starting size distribution, the population of smaller crystallites decreases (and eventually disappears), while the population of the larger size ranges increases, resulting in a tailing to larger crystallite sizes [9]. For a purely inter-crystallite transport process (Ostwald ripening), small crystallites are formed since one crystallite grows at the expense of another. Small crystallites are continuously formed by the shrinking of larger crystallites [10].

5.2.1 Growth via crystallite migration

Sintering via crystallite diffusion takes place in two steps which include crystallite diffusion and coalescence. Coalescence is exothermic due to the thermodynamic driving force of lowering the chemical potential by reducing the dispersion when forming larger crystallites [7]. Consequently the rate of atomic diffusion within the combined crystal is high, resulting in fast coalescence rates [8] along with melting and solidifying into ordered crystals [7].

Geus [13] argued that Au crystallites of 3.2 nm at 300 K in the gas phase would have a mean velocity of 1.42×10^9 nm/s. Experimental results by Masson *et al.* [14] for Au crystallites with an average size of 3.1 nm

supported on potassium chloride indicated mean velocities of 0.15 nm/s at 367 K and 0.4 nm/s at 377 K respectively. A support would thus reduce the rate of sintering since the probability for coalescence is reduced by the slower diffusion rate [12].

The strength of the crystallite-support interaction would control the speed at which the crystallites can move [7]. It was demonstrated for Cu on graphite (HOPG) and a roughened Ar^+ treated HOPG (with a stronger support interaction) that coalescence is reduced by a stronger support interaction [12]. This random movement of metal crystallites resulting from thermal vibrations can be characterized by Brownian motion [5]. Brownian motion is random and over time, initially well dispersed crystallites would collide, resulting in instantaneous coalescence [7]. Since the activation energy for Brownian motion is relatively small, crystallites are likely to be mobile on the surface.

The diffusion rate of entire crystallites increases if the surface atoms of the metal clusters are mobile [7]. Surface melting can occur below the bulk melting temperature due to the destabilization from the surface energy contribution. If surface melting occurs, crystallites can become mobile on the surface. Typically a strong support interaction anchors the crystallites on the surface and restrict movement. If surface melting occurs, or surface atoms become mobile, the crystallite can not be anchored to the support.

Sintering is generally known to be enhanced when surface atoms can become mobile at the Hüttig temperature (0.3 T_{melt}) and when bulk mobility can occur at the Tamman temperature (0.5 T_{melt}) [3]. Close to the melting temperature the crystals are likely to have liquid-like behavior and consequently be extremely mobile on the support surface.

It is well established that the melting temperature for metals decreases with crystallite size [15, 16, 17, 18]. For small crystallites the chemical potential increases due to the contribution of surface energy (see Figure 5.1).

The solid-liquid transition can occur at lower temperatures due to the destabilization of the chemical potential of small crystallites. This would affect the Hüttig and Tamman temperatures for sintering. The size dependent melting temperature is given by the following equation (see Appendix A.3 for detail and derivation).

$$\frac{T}{T_\infty} = 1 - \frac{1}{\Delta H_{fus}}\left(E_{surf}(m)D_s(m) - \frac{3\sigma}{\rho_l^{2/3}}\left(\frac{4\pi}{3N_T(m)}\right)^{\frac{1}{3}}\right) \tag{5.2}$$

The size dependent melting can then be determined from the bulk melting temperature of 1768 K, a heat of fusion ($\Delta H_f = 16.4\ kJ/mol$ [19]) and the liquid surface energy ($\sigma(0K) = 2.51\ J/m^2$). Overbury [20] suggested an empirical equation for determining temperature dependent surface energies

$$\gamma = \gamma^0\left(1 - \frac{T}{T_C}\right)^{1+R} \tag{5.3}$$

with an R value for Cu and Ag of 0.22. It is assumed that this value would also be applicable to cobalt. This method can be used to determine the surface energies at the temperatures of interest. The liquid cobalt surface energy at 500 K can then be equated to $\sigma = 2.33\ J/m^2$. The surface energy of the solid was determined in Chapter 3 with the corresponding size dependent melting temperatures in Figure 5.2. A crystallite with a diameter of 9.3 nm has a Hüttig temperature of 500 K which is in the range of typical Fischer-Tropsch operating temperatures. Crystallites with diameters less than 9.3 nm would thus be highly susceptible to sintering at realistic operating temperatures.

As shown in Figure 5.2, the melting temperature is below the operating temperature for crystallites below a diameter of 2.3 nm. These crystallites will have liquid-like behaviour and should be highly mobile on the support. Crystallites with diameters between 2.3–3.7 nm are above the Tamman temperature and bulk mobility should be possible. These crystallites can be ex-

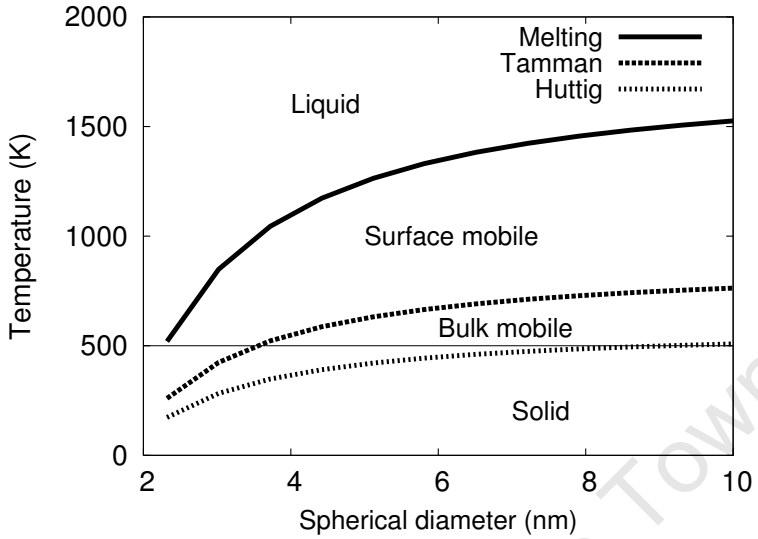

Figure 5.2: Size dependent melting temperature as well as the Hüttig and Tamman temperatures. The typical operating temperature is around 500 K as given by the thin line.

pected to sinter in a fairly short space of time at the operating conditions due to the large driving force and high mobility on the support surface. Above the Hüttig temperature, the surface atoms are mobile and these crystallites are likely to sinter if the support interaction is not very strong. Crystallites with diameters greater than 12 nm have Hüttig temperatures greater than 523 K which is well above the operating temperature of cobalt-based Fischer-Tropsch catalysts. Crystallites with diameters larger than 12 nm should not be susceptible to fast sintering. The sintering of these crystallites should be minimal unless the support interaction is very weak. Due to the fact that Brownian motion does not have a high activation energy, the temperature dependence is weak and sintering can not be avoided, especially for the smaller crystallites.

5.2.2 Growth via inter-crystallite diffusion

An alternative pathway for sintering via crystallite migration is transport of metal atoms either via the gas phase or via surface diffusion [13]. A strong support interaction prevents the mobility of large crystallites, but can enhance diffusion of atomic species via the surface. Stable intermediates can exist in the form of metal oxides or hydroxides on the support surface in certain systems. The mobile gas phase species do not necessarily have to be in the metallic state as postulated for Ag [9].

In the case of a ripening mechanism, the thermodynamics is still driven by the size effect to reduce the dispersion. The kinetics are influenced by the since the energy barriers are reduced for smaller crystallites. This can be illustrated by the argument that an intermediate specie, such as a metal atom or carbonyl is a function of the temperature, pressure and the gas phase composition. At a given set of gas phase conditions, the intermediate specie would have a certain energy. If the intermediate specie is a gas phase cobalt atom, the vapour pressure is determined by the energy difference between the chemical potential of bulk cobalt and the energy of the gas phase cobalt atom. The chemical potential of the small crystallite is higher than for the bulk metal and consequently the energy required to form the gas phase cobalt atom from a nano-crystallite is less. The vapour pressure of a gas phase cobalt atom is higher for small crystallites than for large crystallites. The formation of the mobile intermediate specie (atomic gas phase cobalt) requires less energy if formed from a small crystallite than from a large crystallite. This can be illustrated by the argument that an intermediate specie, such as a metal atom or carbonyl is a function of the temperature, pressure and the gas phase composition. At a given set of gas phase conditions, the intermediate specie would have a certain energy. If the intermediate specie is a gas phase cobalt atom, the vapour pressure is determined by the energy difference between the chemical potential of bulk cobalt and the energy of

the gas phase cobalt atom. The chemical potential of the small crystallite is higher than for the bulk metal and consequently the energy required to form the gas phase cobalt atom from a nano-crystallite is less. The vapour pressure of a gas phase cobalt atom is higher for small crystallites than for large crystallites. The formation of the mobile intermediate specie (atomic gas phase cobalt) requires less energy if formed from a small crystallite than from a large crystallite.

In the case of bulk cobalt the vapour pressure is 1 Pa at 1790 K. This is very low and even for small crystallites, it is highly unlikely that cobalt crystallites would sinter or simply evaporate and disappear into the product. The vapour pressure of 100 Pa for cobalt is only achieved for crystallite sizes below 2 nm (at 1790 K). At lower temperatures the vapour pressure would be even lower. Consequently metal loss or sintering through metal vapour transport of cobalt would be unlikely. The fact still remains that the energy required to form the mobile intermediate from a small crystallite is less than for a large crystallite. The smaller crystallites would thus sinter faster than larger crystallites.

Cobalt carbonyls are significantly more volatile than evaporated cobalt atoms or dimers due to the stabilization from the CO molecules. The sublimation temperature for $Co_2(CO)_8$ is 313 K (in vacuum) and boiling temperature 323 K at atmospheric pressure. The carbonyl compounds decompose at higher temperatures unless extremely high CO partial pressures are maintained. The carbonyl compounds are also sensitive to hydrogen. At large hydrogen and CO partial pressures the $HCo(CO)_4$ carbonyl can be formed but for $H_2/CO > 1$, cobalt carbonyls would not be stable and decompose to the metal and syngas. Again, the energy required to form the cobalt carbonyls is less for small crystallites than for large crystallites. The small crystallites would thus sinter faster than large crystallites due to the higher driving force as well as lower energy barriers for the formation of mobile

intermediates.

5.2.3 Size dependent oxidation

It was shown by Van Steen *et al.* [21] that the likelihood of size dependent oxidation can be determined from thermodynamics, by including a size dependent term in the formulation of the chemical potential. The size at which the oxide phase becomes more stable than the metal phase can be determined using the expression derived in Appendix A.4.2. This expression can be formulated to use the size dependent metal surface energy and the size dependent ratio of metal and oxide surface energies to determine the cut-off size at which oxidation occurs.

$$\mu^0_{CoO(s)} + \mu^0_{H_2(g)} - \mu^0_{Co(s)} - \mu^0_{H_2O(g)} + RTln\left(\frac{p_{H_2}}{p_{H_2O}}\right) + \\ + \frac{6\gamma_{Co}}{\rho_{Co}d_{Co}}\left(\frac{\gamma_{CoO}}{\gamma_{Co}}\left(\frac{\rho_{Co}}{\rho_{CoO}}\right)^{\frac{2}{3}} - 1\right) > 0 \qquad (5.4)$$

Size dependent metal surface energies were determined in Chapter 3. A simple broken bond approach was shown from DFT calculations to give a good description of the coordination dependent surface energy. Therefore the size dependent surface energy can accurately be determined for nanocrystallites. Since CoO is an ionic substance, the size dependent surface energies were determined from the electrostatic energy contribution and a broken bond energy contribution (see Chapter 4). Since polar surfaces of ionic materials are not stable [22, 23], a non-polar stoichiometric surface was considered. The CoO(100) surface is the most densely packed non-polar ionic surface. A cubic crystallite is the most stable morphology which only exposes (100) surfaces.

As a conservative approach, CoO crystallites are assumed to be perfect and consequently have the lowest energy possible. In order to compare the

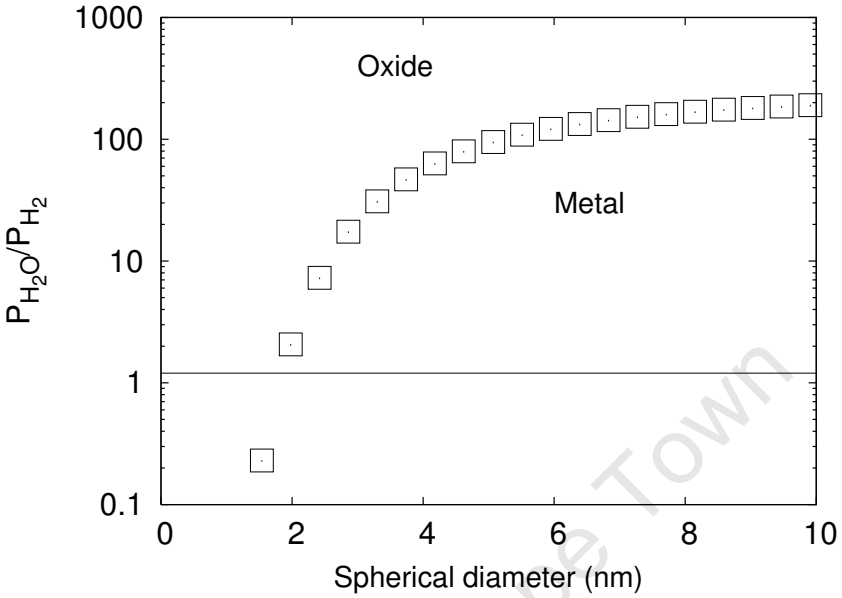

Figure 5.3: Size dependent trend for the oxidation of cobalt to CoO for cubic crystals exposing (100) faces with a data point for each perfect cubic oxide crystallite. The thin line indicates $H_2O/H_2 = 1.2$.

energies for a cobalt and CoO crystal directly, the same number of cobalt atoms are required. The metal crystallite must then either be a perfect cube or transform to a different morphology. The number of atoms in a cube and other crystallite morphologies such as a cubo-octahedron or octahedron do not match. Consequently the oxide crystallite was a assumed to transform to a metal cube upon reduction. The metal cube is not the most stable metal morphology and analysis provides a best case scenario for the formation of CoO.

Figure 5.3 shows the size dependent equilibrium H_2O/H_2 ratios. Based on this information, oxidation at industrially relevant conditions of 500 K and $P_{H_2O}/P_{H_2} < 1.2$ [24] would only occur for crystallites smaller than 2 nm, which is a substantially lower cut-off point than suggested by Van Steen *et al.* of 4.5 nm. Crystallites up to 6 nm would only be in danger of oxidation at ratios of $P_{H_2O}/P_{H_2} > 100$ suggesting that oxidation is highly unlikely at

commercial operating conditions. This result is still consistent when compared to experimental observations as reviewed by Van de Loosdrecht *et al.* [25].

5.3 Conclusions

In this section the effect of the crystallite size on the sintering behaviour of cobalt crystallites was illustrated. It was shown that the driving force for sintering increases with crystallite size. Two sintering mechanisms were discussed, the bulk crystallite diffusion and diffusion via the vapour phase. From the results it is suggested that crystallites with a cubo-octahedron shape and an effective diameter below 7.2 nm would be likely to sinter at Fischer-Tropsch conditions via the coalescence mechanism. This is due to the fact that the operating temperature is above the Hüttig temperature for these crystallites. Larger crystallites would still have the thermodynamic driving force to sinter but this would be kinetically inhibited by the support interaction. The sintering of crystallites below 7.2 nm can not be avoided since the surface atoms of small crystallites are mobile at these temperatures.

Transport of cobalt through the gas phase is unlikely since the vapour pressure is very low. Transport via cobalt carbonyls rather than the atomic species might be possible, but CO partial pressures are presumably too low to ensure stability of carbonyl species.

Due to a larger surface energy than originally estimated, the CoO phase would be even less favourable than suggested previously [21]. The risk of oxidation should be minimal as recently suggested by Van de Loosdrecht *et al.* [25].

References

[1] Astier, M., Teichner, S.J., Vergnon, P., p. 63, in Materials Science Research, Volume 10, "Sintering and Catalysis", Kuczynski, G.C., ed., Plenum Press, 1975.

[2] Bartholomew, C.H., Appl. Catal. A: Gen. 212 (2001), 17.

[3] Moulijn, J.A., Van Diepen, A.E., Kapteijn, F., Appl. Catal. A: Gen. 212 (2001), 3.

[4] Wynblatt, P., Ahn, T-A., p. 83 in Materials Science Research, Volume 10, "Sintering and Catalysis", Kuczynski, G.C., ed., Plenum Press, 1975.

[5] Yang, D.-Q., Sacher, E., Surf. Sci. 516 (2002), 43.

[6] Williams, F.J., Malikova, N., Lambert, R.M., Catal. Lett. 90 (2003), 177.

[7] José-Yacamán, M., Gutierez-Wing, C., Miki, M., Yang, D.-Q., Piyakis, K.N., Sacher, E., J. Phys. Chem. B 109 (2005), 9703.

[8] Lehtinen, K.E., Zacariah, M.R., Phys. Rev. B 63 (2001), 205402.

[9] Wodiunig, S., Keel, J.M., Wilson, T.S.E., Zemichael, F.W., Lambert, R.M., Catal. Lett. 87 (2003), 1.

[10] Rosenfeld, G., Morgenstern, K., Esser, M., Comsa, G., Appl. Phys. A 69 (1999), 489.

[11] Charles, E., Sykes, H., Williams, F.J., Tikhov, S., Lambert, R.M., J. Phys. Chem. B 106 (2002), 5390.

[12] Yang, D.-Q., Sacher, E., J. Appl. Phys. 90 (2001), 4768.

[13] Geus, J.W., p. 29 in Materials Science Research, Volume 10, "Sintering and Catalysis", Kuczynski, G.C., ed., Plenum Press, 1975.

[14] Masson, A., Métois, J.J., Kern, R., Surf. Sci. 27 (1971), 463.

[15] Dick, K., Dhanasekaran, T., Zhang, Z., Meisel, D., J. Am. Chem. Soc. 124 (2002), 2313.

[16] Shi, F.G., J. Mater. Res. 9 (1994), 1307.

[17] Hanszen, K.-J., Z. Phys. 157 (1960), 523.

[18] Buffat, P., Borrel, J.-P., Phys. Rev. A 13 (1976), 2287.

[19] Lide, D.R., Kehiaian, H.V., "CRC Handbook of Thermophysical and Thermochemical Data", CRC Press, Inc., 1994.

[20] Overbury, S.A., Bertrand, P.A., Somorjai, G.A., Chem. Rev. 75 (1975), 547.

[21] Van Steen, E., Claeys, M., Dry, M.E., Van de Loosdrecht, J., Viljoen, E.L., Visagie, J.L., J. Phys. Chem. B 109 (2005), 3575.

[22] Tasker, P.W., J. Phys. C Solid State Phys. 12 (1979), 4977.

[23] Noguera, C., J. Phys. Cond. Matt. 12 (2000), R367.

[24] Van Berge, P.J., Van de Loosdrecht, J., Barradas, S., Van der Kraan, A.M., Catal. Today 58 (2000), 321.

[25] Van de Loosdrecht, J., Balzhinimaev, B., Dalmon, J.-A., Niemantsverdriet, J.W., Tsybulya, S.V., Saib, A.M., Van Berge, P.J., Visagie, J.L., Catal. Today 123 (2007), 293.

Part IV

Deactivation from Carbon Deposition

Chapter 6

The Formation of Carbon Clusters on an FCC-Co(111) Surface

6.1 Introduction

Carbon deposition has been suggested to be one of the possible mechanisms of deactivation in the Fischer-Tropsch synthesis [1, 2, 3] and reported on Fe [4, 5, 6], Co [7, 8, 9, 10] and Ni [11, 12, 13]. Excessive carbon deposition may result in catalyst encapsulation, pore blockage and at extreme conditions, catalyst breakage [2, 4]. The formation of deactivating carbon deposits is a problem which needs to be understood and prevented if possible, by tuning the operating conditions or the catalyst.

At low carbon coverage, the Co surfaces can be reconstructed by adsorption of atomic carbon [14]. Various types of carbon have been suggested to form at high carbon coverages such as polymeric and amorphous films, filaments, fibers, whiskers, platelets and graphite [1].

In Ni-based reforming catalysts, encapsulating carbon and pyrolytic carbon [11] have been suggested to be a possible cause of deactivation. The deposition of carbon has been studied experimentally on Ni-based catalysts [15, 16, 17] to investigate the types of carbon deposited, as well as the effect of conditions on the type of carbon deposited. Various DFT [11, 18, 19] and grand canonical Monte Carlo [20, 21] studies have been performed to investigate carbon structures which can be formed on Ni catalysts. Experimental work on Ru [22] suggested that carbon clusters are preferentially formed at surface steps. DFT studies on Ni showed that graphene and small carbon clusters are stable on flat Ni surfaces [23, 24]. The formation of large carbon clusters on Ni have been investigated using canonical Monte Carlo simulations [20, 21].

Based on experimental and theoretical work, mechanisms have been proposed for carbon formation [25, 26] suggesting that for Ni-based catalysts, stepped surfaces play an important role in carbon deposition. As a consequence, suggestions were made that the selective poisoning of steps should reduce carbon deposition for Ni catalysts [12, 13]. Selective poisoning of Co

catalysts [7] have shown that the type carbon deposits formed are different when poisoned by sulfur, but carbon deposition did not stop completely.

Most of the work to date suggest that the carbon clusters would preferentially form at surface steps. In nano-sized crystallites, the defect sites where nucleation can start according to this mechanism would be much less abundant than on large surfaces. The question therefore arises whether carbon deposits can form on defect- and step-free surfaces. A deeper understanding of the parameters controlling the formation of carbon clusters and overlayers is required to answer this. The information on carbon cluster nucleation and growth would provide insight on the likelihood that carbon deposits will form on nano-sized cobalt crystallites.

Pathways for carbon formation on the flat FCC-Co(111) surface have not been proposed yet. Recent work suggested much lower barriers for C–C coupling on a flat Co(0001) surfaces than on surface steps [27]. Furthermore alternative pathways on flat surfaces would become more important for small crystallites in the nanometer range where the number of steps should be minimal. Consequently surface steps should not play a major role in carbon over-layer formation but rather flat surface regions and possibly ridge sites. Studies on carbon cluster or sheet formation have not been reported for FCC-Co surfaces, where the FCC-Co is stable in small crystallites with diameter below 120 nm [28]. Surfaces for the HCP-Co(0001) and FCC-Co(111) are similar with subsurface layers of HCP-Co which have an ABAB configuration, while subsurface layers of FCC-Co have an ABCABC configuration. This chapter will focus on the formation of carbon clusters on FCC-Co(111) to elucidate pathways for the formation of carbon overlayers.

6.2 Methodology

A systematic study of stability of atomic carbon, carbon clusters, semi-infinite and infinite carbon sheets was performed. This approach would aid

in the understanding of the aspects which play a role in the formation of carbon sheets on flat surfaces of Co-based catalysts. Intermediates under consideration might be formed by sequential addition of atomic carbon to existing carbon clusters on the surface. This analysis is therefore not an exhaustive study of all possible pathways, but rather shows the stability trends of the intermediates with increase in size of the carbon clusters. The energy of carbon addition to existing clusters in the growth process can be used to propose a mechanistic pathway for carbon deposition. The stability of carbon atoms adsorbed on a FCC-Co(111) surface and small carbon clusters as shown in Figures 6.1, 6.2, 6.3 and 6.4 was determined.

The nucleation of carbon clusters may take place by coupling of atomic carbon species to form dimers, trimers and larger carbon clusters (see Figure 6.1). These clusters may grow further forming branched (see Figure 6.3) and ring (see Figure 6.4) structures. Larger clusters may be represented by infinitely long chains as shown in Figure 6.5. Adding an atom to an infinite chain results in branching and further carbon addition leads to ring formation of the surface carbon species. Further addition of carbon results in formation of connected carbon rings (see Figure 6.6) and eventually will form graphene.

For the small clusters, the clusters are named by number of carbon atoms and whether the atoms are on the fcc (f), hcp (h) or bridge (b) site. For larger clusters the number of carbon atoms is used along with the character such as linear, branched or ring. For the infinite chains, the clusters are named after the "functional" group to the chain such as a branch, C5-ring or C6-ring. For the infinite aromatic rings (Ar), the structures with one ring in the finite dimension are named according to the adsorption site and whether the centre of the ring is above the bridge or top site. The larger aromatic structures are only named by the number of rings in finite dimension.

All these structures were calculated in periodic unit cells. One of the

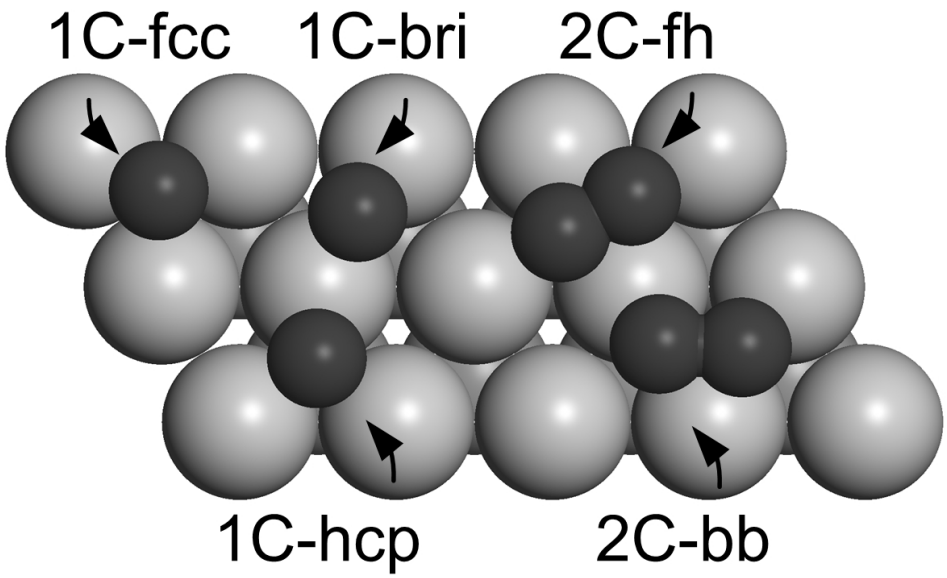

Figure 6.1: Atomic carbon on fcc (*1C-fcc*), hcp (*1C-hcp*) and bridge sites and carbon dimers (*2C-bb* and *2C-fh*) investigated as possible intermediates in the formation of graphene.

limitations of the periodic cell approach is that extremely large unit cells are required to fit the carbon structures into the unit cell and minimize lateral interactions with neighboring clusters. The computational cost scales significantly for larger unit cells with more atoms. For this reasons unit cells beyond $p(1 \times 6)$, $p(2 \times 3)$ and $p(3 \times 3)$ were not investigated.

Lateral interactions must be minimized since the resulting destabilization does not provide the true stability of the cluster. If surface cobalt atoms are connected to carbon atoms of different clusters, the energy of the carbon cluster was found to be destabilized by at least 20 *kJ/mol carbon* (for atomic species, dimers and branched chains). The surface models were set up such that carbon atoms in the structures did not share surface cobalt atoms with neighboring clusters. This was found to drastically reduce lateral interaction and give a good representation of the stability of the cluster. Comparing the adsorption energy of atomic carbon on FCC-Co(111) at a coverage of

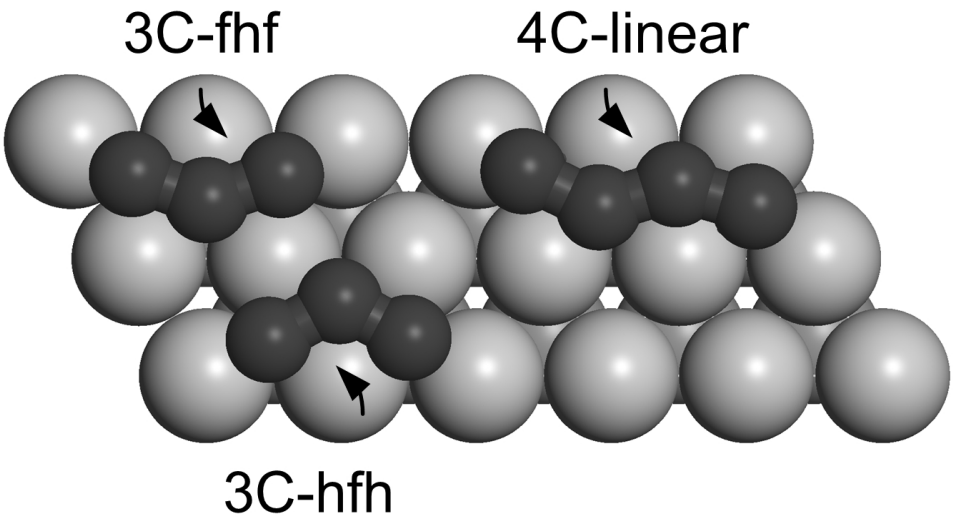

Figure 6.2: Trimers and linear tetramer investigated as possible intermediates in the formation of graphene. The *3C-fhf* has two carbon atoms on fcc sites and one on the hcp site in between, while the *3C-hfh* has two hcp and one fcc atom.

25% and 11%, the reduced lateral interaction resulted in a further stabilization by only 3 *kJ/mol carbon* and therefore surface coverage of 25% was therefore used for the adsorbed carbon atoms. A similar result was found for the infinite *Ar-1ring-top* structure, where this structure was more stable by 3 *kJ/mol carbon* at a lower coverage.

For the carbon clusters containing up to three atoms a $p(2 \times 2)$ surface unit cell was used resulting in minimal lateral interactions, but for larger clusters $p(2 \times 3)$ and $p(3 \times 3)$ surface unit cells were used. For most of the structures in Figure 6.5 a $p(2 \times 3)$ surface unit cell was used. The structures in Figure 6.6 (*Ar-1ring-bri* and *Ar-2ring-bri*) were calculated in a $r(1 \times 4)$ surface unit cell, while the *Ar-3ring-bri* and *Ar-4ring-bri* structures were calculated in a $p(1 \times 6)$ surface unit cell.

The calculated energies for the atomic species and clusters ($E_{ads-carbon}$ in *kJ/mol carbon*) are reported as the energy of formation of carbon clusters ($E_{C^*_{ads}}$) from CO (with energy E_{CO}) and hydrogen (E_{H_2}) yielding water

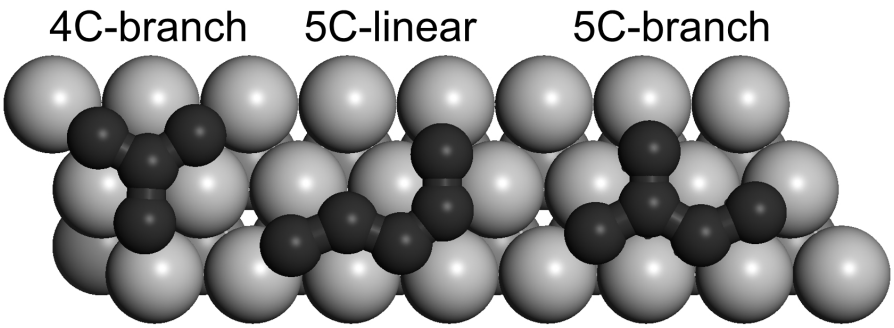

Figure 6.3: Larger clusters investigated as possible intermediates in the formation of graphene.

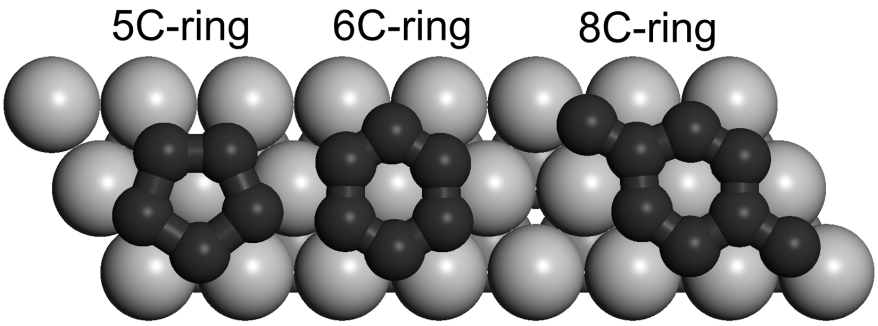

Figure 6.4: Ring clusters investigated as possible intermediates in the formation of graphene.

(E_{H_2O}) as a by-product.

$$CO + H_2 \Longleftrightarrow C^*_{ads} + H_2O \tag{6.1}$$

$$E_{ads-carbon} = \frac{(E_{C^*_{ads}} + E_{H_2O}) - (nE_{CO} + nE_{H_2} + E_{slab})}{n} \tag{6.2}$$

The adsorption energy per carbon atom can also be calculated relative to atomic carbon in the gas phase. The adsorption energy is then simply 902 *kJ/mol carbon* lower than the adsorption energies reported here. The energy relative to $H_2 + CO$ was used since this is more representative of a Fischer-Tropsch like environment. A negative adsorption would suggest that the adsorption state is favoured relative to $H_2 + CO$ in the gas phase

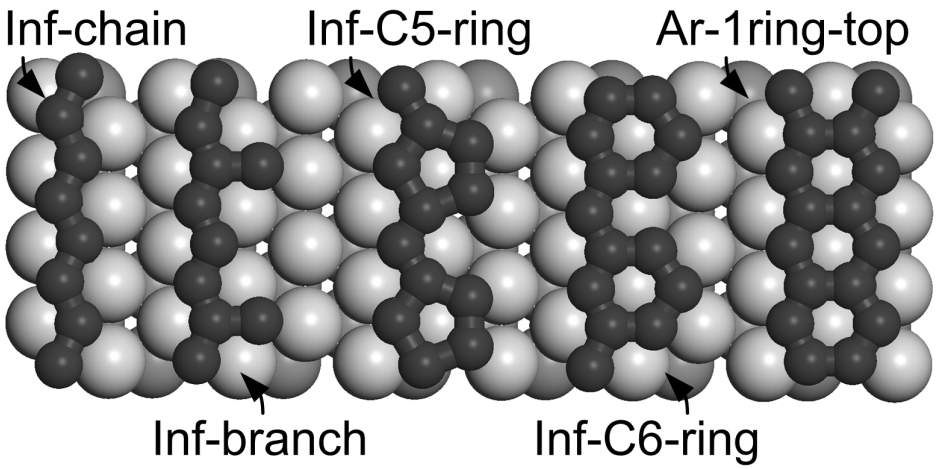

Figure 6.5: Infinite structures in one dimension were studied such as shown here.

being converted to adsorbed carbon and H_2O. This adsorption energy does not provide insight into the interaction strength of the carbon atoms or clusters with the surface but the thermodynamic stability of the species on the surface.

Calculations were performed with only carbon on the FCC-Co(111) surface. The results would therefore describe a situation where oxygen removal via water formation on surface is fast, ensuring no hydrogen or oxygen species from the syngas on the surface. Hydrogenated species were not considered in this study but Cheng *et al.* [27] did investigate barriers for C–H and other hydrogenated carbon species.

Spin polarized DFT calculations for these adsorbed structures have been performed on a 3D periodic slab model using VASP (see discussion in Chapter 2). PW91-GGA pseudopotentials were used which gave a bulk lattice parameter for the FCC-Co phase of 2.501 Å. Various Monkhorst-Pack [29] k-point grids have been used for these unit cells ranging from $15 \times 15 \times 1$ for a $p(1 \times 1)$ unit cell to $5 \times 5 \times 1$ for a $p(3 \times 3)$ unit cell. Along with these settings, an energy cut-off of 400 eV and a Methfessel-Paxton [30] smearing with $sigma = 0.1$ eV was used to ensure accurate energies with small errors

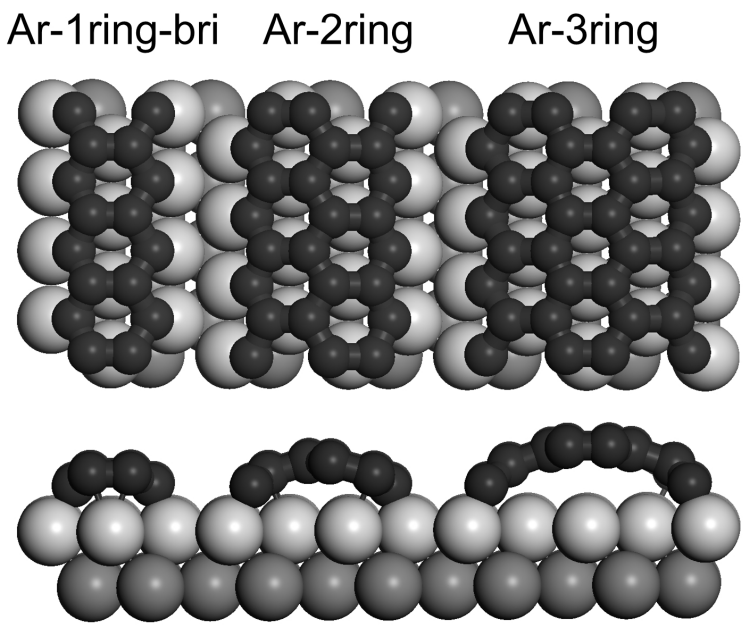

Figure 6.6: Optimized geometries for infinite multiple ring structures viewed from the top and side.

due to smearing of less than 10 *meV per unit cell* for all systems (containing at least 20 metal atoms). A slab thickness of 5 layers for the FCC-Co(111) surface gave good convergence for adsorption energies (within 2 *kJ/mol carbon* relative to adsorption energies on a 7 layer slab for atomic species and graphene sheets). Slabs were separated by 8 vacuum layers, resulting in a separation distance of at least 10 Å between adsorbed carbon structures on the surface. Geometry optimizations were performed by minimizing the energy to within 1×10^{-4} eV for the slab and minimizing forces to within 0.02 $eV/$Å by allowing all atoms to relax.

A vibrational analysis was performed on the *1C-hcp*, *2C-fh*, *3C-fhf*, *4C-branched*, *Inf-1ring-bri* and adsorbed graphene structures to ensure that the zero point energy correction would not affect the stability trends. The zero point vibrational energies were 9.4, 10.3, 10.4, 2.4, 6.7 *kJ/mol carbon* for these structures respectively, suggesting that the zero-point energy does not

affect the energy trends. The zero-point energy corrections are not included in the reported energy trends.

6.3 Results

6.3.1 Stability trends of carbon species

The energies of the adsorbed carbon atoms and clusters are given in Figure 6.7 as relative to the formation from H_2 + CO to form H_2O as a by-product. Thermodynamically stable geometries for atomic species are such that the carbon atoms in the cluster are located in the threefold hollow sites with Co–C distances of 1.80 Å. The energy of adsorption is -66.9 *kJ/mol carbon* on the fcc and -91.6 *kJ/mol carbon* on the *hcp* site. The energy difference between the atomic carbon adsorbed on fcc and *hcp* sites is 24.7 *kJ/mol carbon* suggesting a substantial site preference for the *hcp* site due to the interaction of the carbon atom with the sub-surface cobalt atom. Atomic carbon species are not stable on the top of the metal atom or on the bridge sites since the carbon optimized to the hollow (fcc and *hcp*) positions from the top and bridge starting geometries. A quasi-Newton approach was used where only the forces minimized to determine the adsorption energy at the bridge site with an energy of -49.6 *kJ/mol carbon*. A vibrational analysis confirmed that the bridge site has one imaginary frequency and is therefore a transition state for diffusion.

Carbon clusters were found to be more stable than atomic carbon species (see Figure 6.7). All the chain-like (unbranched) clusters were found to have the most stable geometries with the carbon atoms in hollow sites. Various dimer configurations at 0.5 ML coverage were calculated but only the *2C-fh* and *2C-bb* was found to be stable. The dimer (*2C-fh*) has a C–C distance of 1.32 Å, while the Co–C distances are 1.89 Å and 2.05 Å respectively. The C–C distances for the trimers (*3C-fhf* and *3C-hfh*) are both 1.35 Å,

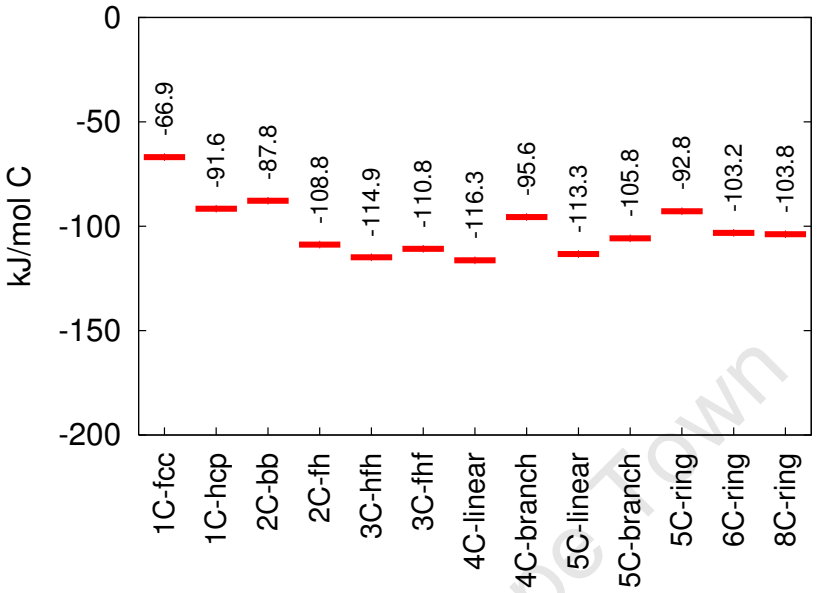

Figure 6.7: The energies for the finite carbon clusters (see Figures 6.1, 6.2, 6.3 and 6.4) are given here relative to syngas.

while the Co–C distances range between 1.87 Å and 2.01 Å with the middle carbon atom slightly lifted. Similar Co–C bond lengths are observed for the unbranched tetramer (*4C-linear*) and pentamer (*5C-linear*), while the C–C bond lengths are slightly distorted to 1.32 Å and 1.35 Å respectively for tetramer and vary between 1.32–1.39 Å for the unbranched pentamer (*5C-linear*). The terminating carbon atoms on the cluster bind stronger to the surface than the internal carbon atoms. These distances show that the interaction with the surface decreases slightly with an increase in cluster size. All the linear clusters are more stable than atomic species with adsorption energies ranging from -108.8 to -116.3 *kJ/mol carbon*. An infinite linear chain as shown in Figure 6.5 also has a stability in this range and similar bond lengths (Co–C distances are 2.03 Å, while the C–C distances are close to 1.33 Å).

Nucleation of branched clusters could be possible, but calculations show

that the finite branched clusters (*4C-branch* and *5C-branch*) are less stable than linear clusters (*4C-linear* and *5C-linear*) with the same number of atoms. The branched carbon atoms which are connected to three other carbon atoms are lifted from the surface indicating a weaker interaction with the surface compared to linear clusters. The branched tetramer (*4C-branch*), have C–C distances of 1.47 Å, while the Co–C distances vary from 1.87–1.95 Å for the terminating atoms to 2.27 Å for the tertiary carbon atom. Similar bonding distances are observed for the branched pentamer (*C5-branch*) where the C–C bond lengths to the tertiary carbon atom vary between 1.44 and 1.48 Å, while the C–C bonding lengths between the internal and terminating carbon atoms are close to 1.35 Å. The infinite branched chain (*inf-branch*) shows similar results with C–C distances to the branched atoms of 1.44 Å, while the C–C distances between internal carbons are only 1.35 Å. The Co–C atoms for carbon connected to tertiary carbon atoms range between 1.87–1.95 Å, while the Co–C distances for internal carbon atoms range between 2.01–2.28 Å. For the tertiary carbon atoms, the Co–C bonds range between 2.26–2.38 Å. This is also the case for branched ring (*8C-ring*). Tertiary carbon atoms have thus a decreased interaction with the surface and therefore a greater Co–C distance. This could be explained by the fact that the sp_2 orbitals for tertiary carbon atoms can be filled by the electrons of surrounding carbon atoms. The terminating carbon atoms of the cluster do not have this stabilization and remain close to the surface for small unbranched clusters or move toward the surface for larger branched clusters and sheets.

Ring species such as the *6C-ring* and *5C-ring* structures are more stable than the atomic species but not as stable as the linear unbranched species. The branching of these ring clusters (*8C-ring*) does not severely affect the stability of the clusters as seen in Figure 6.7. When linking up the *C5-* and *C6-ring* structures (see Figure 6.5), only the *Inf-C5-ring* structure is stabi-

lized, while the *Inf-C6-ring* has a similar stability to the finite ring structures. When an infinite aromatic ring structure (*Ar-1ring-top*) is formed by adding one carbon atom, a significant stabilization is obtained (see Figure 6.8). The Co–C bonds are slightly longer than for the finite clusters with the bridged carbon atoms having a Co–C distance of 2.32 Å, while the bridging (internal) carbon atoms have a Co–C distance of 2.12 Å. The C–C distances are 1.50 Å between the branched atoms, while the other C–C bond lengths are 1.44 Å.

This *Ar-1ring-top* structure can then be stabilized with 10 *kJ/mol carbon* by shifting the structure to the ring-bridge site (*Ar-1ring-bri*) where the centre of the ring is above the bridge site. The optimized structure on this site had C–C distances of 1.48 Å between branched atoms and 1.44 Å for the other C–C bonds. For this structure the carbon atoms are not directly above the hollow sites anymore, but two Co–C distances are lengthened, while one is shortened. The secondary carbon atoms have nearest Co–C distance of 1.89 Å, while the other two Co–C distances are 2.46 Å. A similar trend is observed for the branched atoms with one Co–C distance of 2.01 Å, while the other two Co–C distances are between 2.81 and 2.84 Å. For these aromatic structures, the secondary carbon atoms would terminate the cluster and therefore have a stronger interaction with the surface. For the aromatic structures, the carbon atoms have a sp_2 orbital structure and the tilting of the terminating atom towards a metal atom can fill the sp_2 orbital and stabilize the cluster. The ring-bridge site would therefore be ideal to fill the sp_2-like orbitals.

Larger ring structures were calculated up to aromatic 4-ring structures where the aromatic 1-, 2- and 3-ring structures are shown in Figure 6.6. All these structures are most stable on the ring-bridge type geometries. The larger aromatic structures are significantly more stable compared to the linear clusters (see Figure 6.8). For these structures, the branched carbon

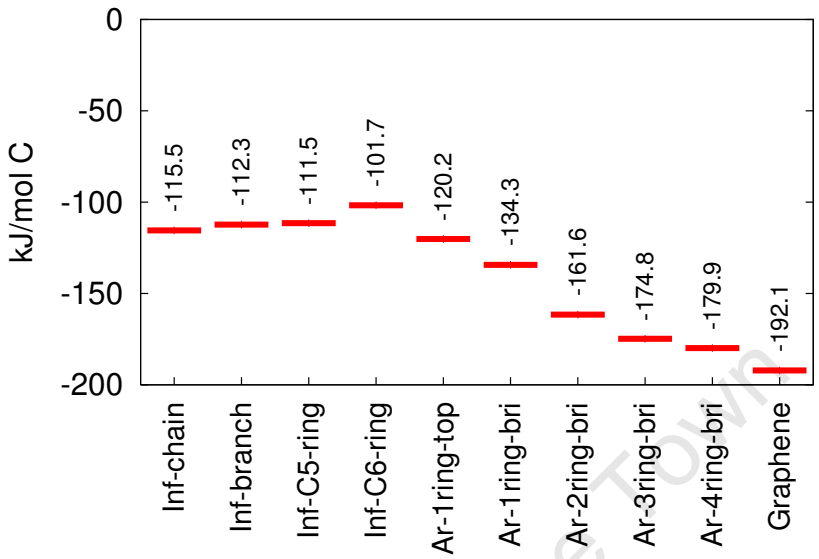

Figure 6.8: Energies for clusters with one or more infinite dimensions (see Figures 6.5 and 6.6 relative to syngas.

atoms start lifting from the surface forming an "arch-like" structure. The Co surface atoms can then easily fill the sp_2 orbitals of the cluster terminating carbon atoms. The Co–C distances for the cluster terminating carbon atoms are 1.91 Å and 2.23 Å. The carbon atoms at the centre of the cluster are approximately 2.8 Å above the surface for the *Ar-2ring-bri* structure. The *Ar-3ring-bri* cluster lifts up to 3.1 Å in the centre of the cluster, while the *Ar-4ring-bri* cluster lifts up to approximately 3.3 Å above the surface. The C–C distances for all the larger ring structures range between 1.43 and 1.45 Å, which is close to the 1.42 Å of graphene.

The energy of the flat graphene sheet on the surface was the most stable of all the aromatic structures. The graphene sheet had a Co–C distance of 2.12 Å. This stability is ascribed to the tendency of the system to accommodate both the aromaticity of the cluster and the metal-carbon interaction required to saturate the terminating sp_2-like bonds.

6.3.2 Coverage effects

Carbon clusters are stable at a high coverage, but carbon atoms are not. In the case of atoms the interaction at coverage above 0.25 ML is repulsive, rendering a coverage of carbon atoms at 1 ML unstable relative to the Fischer-Tropsch gas phase conditions due to the positive adsorption energy. The infinite chain at an effective coverage of 1 ML is more stable than adsorbed carbon atoms at 0.25 ML. Very stable clusters can be formed when the local coverage become high enough to form C–C bonds. The large stability at high coverages can be attributed to C–C bonds rather than the interaction of carbon with the surface. The interaction with the surface weakens if other atoms or clusters are too close to the carbon cluster.

From a thermodynamic point of view, high carbon coverages will result in the formation of carbon clusters. Cluster growth can be seen as a thermodynamic surface phase segregation or "island" formation. For the most stable state, a region of high carbon coverage (carbon cluster with coverage of up to 2 ML) and a region of low coverage is more stable than than an even distribution of atomic carbon on the surface with a carbon coverage above 0.11 ML.

6.4 Discussion

All proposed carbon clusters on FCC-Co(111) are stable with respect to the conditions of the Fischer-Tropsch synthesis and can thus be formed under these conditions. Furthermore, carbon clusters are more stable than adsorbed atomic carbon, demonstrating the stabilizing effect obtained through C–C coupling. The carbon clusters are less stable than adsorbed graphene on FCC-Co(111). The formation of graphene from adsorbed carbon atoms or clusters is energetically a downhill process since the thermodynamic driving force will always exist. A surface covered purely with carbon will inevitably

lead to deactivation through the formation of large carbon clusters.

Growth of carbon clusters may occur through surface C–C coupling. This may happen faster on flat surfaces than on stepped surfaces as shown for the HCP-Co(0001) surface by Cheng *et al.* [27]. C–C coupling not only requires a facile transition state, but also adsorbed carbon species in close proximity. Diffusion of atomic carbon is thus an important sub-process in C–C coupling. Atomic carbon on stepped surfaces is expected to have a lower mobility than carbon atoms adsorbed on the flat surface. This is a result of the interaction of carbon atoms with low coordination surface atoms being stronger than the interaction of atomic carbon with higher coordinated flat surface atoms [18]. The mobility of atomic carbon adsorbed on the FCC-Co(111) surface can be estimated from the energy of formation of atomic carbon on the bridge and top sites. These geometries are not stable, but can be used to estimate the lower limit to the barrier of diffusion of atomic carbon on the FCC-Co(111) surface. The energy of formation of carbon on the bridge site is found to be -49 *kJ/mol carbon* suggesting a barrier for diffusion of atomic carbon from the hcp to fcc sites of 42 *kJ/mol carbon*. The barrier of diffusion from the fcc to hcp site is only 18 *kJ/mol carbon*. The barrier for diffusion from the hcp site to hcp site is thus 42 *kJ/mol carbon* on the FCC-Co(111) surface. This value is in good agreement with the 52 *kJ/mol carbon* suggested for Ni(111) [18]. The diffusion of atomic carbon on the FCC-Co(111) surface should therefore be possible under Fischer-Tropsch conditions of 500 K. The mobility of larger carbon clusters is expected to be much less than that of the smaller clusters and especially atomic carbon. A translation of larger clusters would require a concerted movement over the surface since C–C bonds are very strong. Such a concerted movement would lead to all of the atoms being destabilized over the bridge sites simultaneously.

Growth of carbon clusters is therefore thought to occur initially from the attachment of adsorbed atomic carbon to the larger structures. The formu-

lation of linear chains by sequential addition of adsorbed atomic carbon is favoured over the formation of branched and cyclic clusters. Hence, the formation of chain-like structures on the FCC-Co(111) surface can be expected as was shown for Ni Monte Carlo simulations [20]. Branches can be formed and are more likely to form with longer chains, since the energy difference between the addition of atomic carbon to the terminal carbon atom and the formation of a branch is only 3–4.5 *kJ/mol carbon* added to a chain. The formation of larger carbon clusters is even favoured at relative high coverage of the surface. Linkage between adjacent chains may lead to the formation of more stable aromatic structures such as *Ar-1ring-top*. This may further stabilize through a shift in the adsorption position to *Ar-1ring-top*. Further linkage with long chains or sequential addition of carbon may lead to growth of the aromatic structure and eventually lead to the formation of graphene on the surface.

From this growth model, the formation of carbon sheets on cobalt does not require a stepped surface or defects. Carbon diffusion over the surface is facile and nucleation and is thermodynamically favoured on the flat FCC-Co(111) surface. It has been proposed that steps act as preferential nucleation sites [18], but the relative high mobility of adsorbed atomic carbon negates the presence of these special nucleation sites. Selective poisoning of the step defects would thus not necessarily inhibit the formation of graphene, since stable intermediates can be formed on the flat FCC-Co(111) surface. A certain minimum number of adjacent Co surface atoms on the flat surface are required to nucleate carbon clusters and grow the graphitic ring structures. It can thus be postulated that if a sufficient number of adjacent metal atoms on the surface is not available, carbon clusters can not nucleate or grow. This could be the case if immobile atoms such as gold or sulphur are present on the surface, limiting the space available on the surface for cluster growth and consequently "poisoning" the surface for cluster nucleation

and growth. It was postulated previously [13] that these poisoning atoms would have a greater inhibiting effect on the formation of carbon deposits which require a large surface ensemble than e.g. methanation which requires a smaller ensemble of surface atoms. Sulphur poisoning by Kim *et al.* [7] showed the formation of less "graphitic" carbon and more "amorphous" carbon. This was postulated to be due to the fact that small clusters can not grow to sheets but rather form a nano-crystalline agglomeration of amorphous carbon.

Step defects may stabilize the aromatic clusters further and thus facilitating carbon over-layer formation. It was shown that in aromatic structures, the clusters start bending to accommodate the sp_2-like orbitals of the terminating carbon atoms of the cluster. This termination can also easily occur at a step defect in the surface. This might prevent bending of the part of the cluster down to the surface in order to fill the sp_2-like orbitals of the cluster terminating carbon atoms. It was shown that carbon sheets connected to step defects would remain flat on the surface as shown on Ni [17]. For relatively small carbon structures, having one side of the aromatic cluster attached to a step does not necessarily result in a flat sheet, as seen for Ni [18] where bent structures were observed in order to saturate the sp_2 bonds of the terminating carbon atoms. Cluster termination may occur with hydrogen, allowing the aromatic cluster to remain "flat" on the surface.

The bent structures have only been calculated with one infinite dimension. The behaviour of a two dimensional cluster would probably be slightly different since the sp_2-like bonds must then be saturated in two dimensions (see [21]). The compensation for the sp_2 like orbitals of the carbon should be more difficult for a two dimensional cluster since this would require the formation of a blister on the surface as reported for Ni [16].

6.5 Conclusions

DFT calculations on FCC-Co(111) show that graphitic carbon clusters can form via stable intermediates on the flat Co surface starting from adsorbed atomic carbon. The preferential site for atomic adsorption is the hcp-site. The formation of linear carbon structures is slightly favoured over the formation of branched carbon structures with the same number of carbon atoms, due to a reduced metal-carbon interaction and carbon-carbon interaction on the tertiary carbon atom. Aromatic clusters were seen to lift off from the flat surface, resulting in Co–C distances substantially larger than the Co-C distance for graphene adsorbed on a flat FCC-Co(111) surface. This is caused by the need to saturate the terminating sp_2-like bonds by forming Co–C bonds and the need to maintain aromaticity of the system. Sequential addition of carbon is proposed as the initial step for the formation of carbon over layers resulting in the formation of (branched) carbon chains. Linkage of carbon chains at high coverage will give rise to the formation of the more stable aromatic clusters. Further growth of these structures, either through addition of atomic carbon or linking-up of longer chains will result in the formation of graphene on the surface. A pre-requisite for this mechanism is that enough space is available on the surface. Highly mobile atomic carbon carbon species on the surface is also required. This is the case for atomic carbon on the FCC-Co(111) surface for which the barrier of diffusion is in the order of 40-50 *kJ/mol carbon*.

These structures can simply form from the sequential addition of atomic carbon or carbon dimers to other clusters with a resulting growth of the clusters to form carbon sheets. Alternative pathways to the step growth mechanisms (where the carbon sheet grows from the surface step) are available for the formation of graphitic carbon. Larger connected ring structures start bending to ensure maximum interaction of sp_2 type orbitals with the surface.

The formation of aromatic carbon clusters and sheets has a large thermodynamic driving force since the aromatic carbon is very stable. Deactivation via carbon deposition can thus not be avoided completely. A suitable environment for carbon deposition would be low in hydrogen since hydrogen can limit the cluster growth by terminating the clusters. High carbon coverages without hydrogen or other strongly adsorbing "poisoning" surface species such as sulphur, would inevitably result in aromatic carbon formation and a physical blockage of the surface.

References

[1] Bartholomew, C.H., Appl. Catal. A: Gen. 212 (2001), 17.

[2] Moulijn, J.A., Van Diepen, A.E., Kapteijn, F., Appl. Catal. A: Gen. 212 (2001), 3.

[3] Menon, P.G., J. Mol. Catal. 59 (1990), 207.

[4] Dry, M.E., Catal. Today 71 (2002), 227.

[5] Sault, A.G., Datye, A.K., J. Catal. 140 (1993), 136.

[6] Shroff, M.D., Kalakkad, D., Coulter, K.E., Köhler, S.D., Harrington, M.S., Jackson, N.B., Sault, A.G., Datye, A.K., J. Catal. 156 (1995), 185.

[7] Kim, M.S., Rodriguez, N.M., Baker, R.T.K., J. Catal. 143 (1993), 449.

[8] Lee, D., Lee, J., Ihm, S., Appl. Catal. 36 (1988), 199.

[9] Font Freide, J.J.H.M., Gamlin, T.D., Hensman, J.R., Nay, B., Sharp, C., J. Nat. Gas Chem. 13 (2004), 1.

[10] Gruver, V., Young, J., Engman, J., Robota, H.J., Prepr. Pap. Am. Chem. Soc. Div. Pet. Chem. 50 (2005), 164.

[11] Bengaard, H.S., Nørskov, J.K., Shested, J., Clausen, B.S., Nielsen, L.P., Molenbroek, A.M., Rostrup-Nielsen, J.R., J. Catal. 209 (2002), 365.

[12] Besenbacher, F., Chorkendorff, I., Clausen, B.S., Hammer, B., Molenbroek, A.M., Nørskov, J.K., Stensgaard, I., Science 279 (1998), 1913.

[13] Rostrup-Nielsen, J.R., J. Catal. 85 (1984), 31.

[14] Ciobîcă, I.M., Van Santen, R.A., Van Berge, P.J., Van de Loosdrecht, J., Surf. Sci. 602 (2008), 17.

[15] Derbyshire, F.J., Carbon 13 (1975), 189.

[16] Presland, A.E.B., Walker, P.L., Jr., Carbon 7 (1969), 1.

[17] Helveg, S., Lopez-Cartes, C., Shested, J., Hansen, P.L., Clausen, B.S., Rostrup-Nielsen, J.R., Abild-Pedersen, F., Nørskov, J.K., Nature 427 (2004), 426.

[18] Abild-Pedersen, F., Nørskov, J.K., Rostrup-Nielsen, J.R., Sehested, J., Helveg, S., Phys. Rev. B 73 (2006), 115419.

[19] Lee, Y.H., Kim, S.G., Tomanek, D., Phys. Rev. Lett. 78 (1997), 2393.

[20] Amara, H., Bichara, C., Ducastelle, F., Phys. Rev. B 73 (2006), 113404.

[21] Amara, H., Bichara, C., Ducastelle, F., Surf. Sci. 602 (2008), 77.

[22] Wu, M.C., Xu, Q., Goodman, D.W., J. Phys. Chem. 98 (1994), 5104.

[23] Kalibaeva, G., Vuilleumier, R., Meloni, S., Alavi, A., Ciccotti, G., Rosei, R., J. Phys. Chem. B 110 (2006), 3638.

[24] Wang, S.G., Liao, X.Y., Cau, C.B., Li. Y.W., Wang, J., Jiao, H., J. Phys. Chem. 111 (2007), 10894.

[25] Rostrup-Nielsen, J., Trimm, D.L., J. Catal. 48 (1977), 155.

[26] Shelton, J.C., Patil, H.R., Blakely, J.M., Surf. Sci. 43 (1974), 493.

[27] Cheng, J., Gong, Z.-Q., Hu, P., Lok, C.M., Ellis, P., French, S., J. Catal. 254 (2008), 285.

[28] Kitakami, O., Sato, H., Shimada, Y., Sato, F., Tanaka, M., Phys. Rev. B 56 (1997), 13849.

[29] Monkhorst, H.J. Pack, J.D., Phys. Rev. B 13 (1976), 5188.

[30] Methfessel, M., Paxton, A.T., Phys. Rev. B 40 (1989), 3516.

Chapter 7

Interaction of Graphene with an FCC-Co(111) Surface

7.1 Introduction

At standard and severe operating conditions in the Fischer-Tropsch synthesis, carbon deposits can be formed, which may cover the active metal surface resulting in loss of catalytic activity [1, 2]. In the previous chapter it was shown that the driving force is thermodynamics since the large carbon clusters are very stable. The carbon deposits are usually formed in layered structures on the surface [3, 4]. Deactivation can result from strong adsorption of a graphene sheet on the catalyst surface [5], which would lead to blockage of the surface.

It is important to establish whether the carbon sheets would "stick" to the surface or whether they can lift or slide off the surface. The mobility is determined by the interaction of the sheet with the metal surface. The interaction of a graphene layer with the Ni surface has been studied previously [6, 7, 8, 9, 10, 11, 12, 13, 14]. The experimental and theoretical work suggested the mono-layer of carbon on the surface to have a C–C distance of 1.44 Å which is only slightly larger than the C–C distance in graphite of 1.42 Å [15]. Some of these studies claim the metal-graphene interaction to be Van der Waals in nature while other claim that charge transfer takes place from the metal to the graphene. There is no agreement on the nature or the strength of interaction of the graphene sheet with the Ni(111) surface.

DFT calculations on Ni suggested an adsorption energy for graphene on the Ni(111) surface of -4.8 *kJ/mol carbon* [6]. Although this is a small energy per atom, it must be kept in mind that this energy is only the energy per carbon atom for an infinitely large sheet adsorbing on a Ni(111) surface. If a sheet consists of 100 carbon atoms, the adsorption energy would be 480 kJ for the sheet. The removal of the sheet would have too high an energy cost and would therefore not be likely to occur.

This chapter explores the nature and strength of the interaction of a graphene mono-layer with the FCC-Co(111) surface. Periodic DFT provides

an efficient and accurate model to calculate properties of transition metal surfaces and is in this study.

7.2 Methodology

7.2.1 DFT calculation setup

Periodic slab calculations were performed for graphene, graphite, metal slabs and adsorbed graphene to understand the interactions that exist between the graphene and the surface. DFT calculations have been performed with VASP (see discussion in Chapter 2). The PW91-GGA PAW potentials were used for all calculations. Additional calculations were performed with ultrasoft LDA potentials [17, 18]. A Monkhorst-Pack [19] k-point grid of $15 \times 15 \times 1$ was used for the $p(1 \times 1)$ unit cell. Along with these settings, an energy cut-off of 400 eV and a Gaussian smearing with $\sigma = 0.01$ eV was used to ensure accurate energies with errors due to smearing of less than 1 meV per unit cell. Geometry optimizations were performed by minimizing the energy to within 0.1×10^{-3} eV for the slab and minimizing interatomic forces to within 0.02 $eV/$Å by optimizing the geometry of all atoms. This electronic setup for the calculations was used to calculate the physical properties such as density of states, work function, and electron density distribution (see Chapter 2 for details on how to analyse these properties).

7.2.2 Graphene and graphite

Graphite (multiple sheets) and graphene (single sheet) were studied in order to establish the ability of DFT to describe the pure carbon system. Graphene is described by one lattice parameter a, which gives the intra-sheet dimensions and relates the C–C distances (C–C $= a/\sqrt{3}$) within an aromatic carbon sheet. Since graphene is a single aromatic carbon sheet,

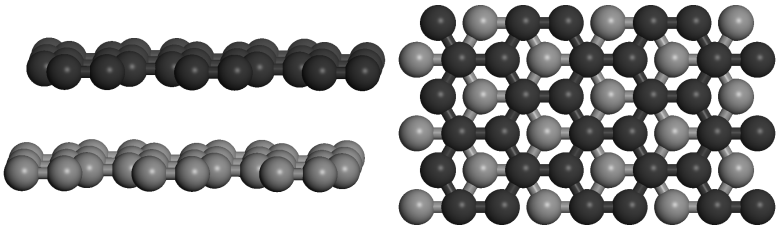

Figure 7.1: Two layers of graphite viewed from the side and top indicating the ABAB configuration.

with the energy calculated in a 3D periodic unit cell, the distance perpendicular to the sheets in the repeating unit must be large enough to avoid any interaction through the vacuum. It was found that a 10 Å interlayer separation was sufficient to eliminate long range electron interactions between different sheets. In order to test the DFT model for carbon, the graphite structure (see Figure 7.1) was used where the graphene sheets are π-stacked in an ABAB configuration while the lattice parameter c represents the inter-sheet spacing. The lattice parameter a was fixed at the equilibrium value or 2.46 Å and used for the optimization of the inter-sheet lattice parameter c of graphite in an AAAA and ABAB configuration. This approach was followed since the inter- and intra-sheet interactions are different in nature and are not described by DFT equally well [20]. The inter-sheet results will be discussed in more detail in the results section.

7.2.3 Surface model

For the FCC-Co(111) surface, slab models of 5- and 7-metal layers were used with graphene adsorption on both sides of the slab using inversion centre symmetry to speed up the calculations efficiently while keeping the surfaces on both sides of the slab identical. The adsorption energies calculated were checked for convergence relative to slabs with thicknesses of 9 and 11 layers to ensure that the slab is thick enough to provide accurate results. Calculations of the cobalt metal surface energy (uncorrected) differed

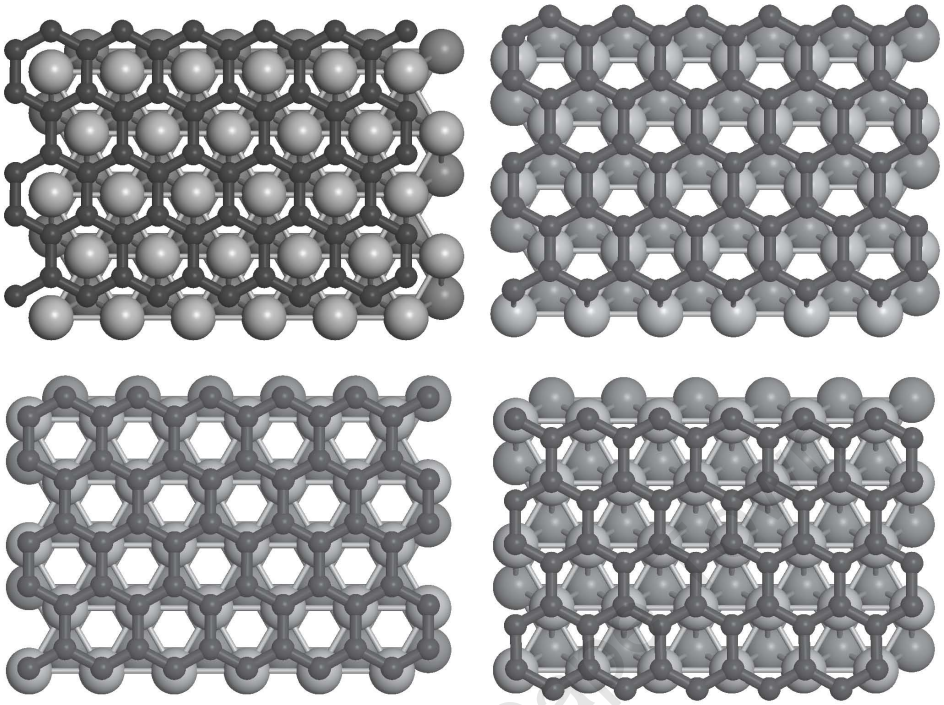

Figure 7.2: Adsorption sites for graphene on FCC-Co(111) at *ring-top* (top left), *ring-bridge* (top right), *ring-fcc* (bottom left) and *ring-hcp* (bottom right) sites. The top layer Co atoms are light gray and the second layer is dark gray with the carbon atoms in black.

by 0.02 *eV/surface atom* or 0.07 J/m^2 from 5 to 11 layers. In the 3D periodic cell, the surface slabs were separated by 8 vacuum layers, resulting in a vacuum spacing of about 14 Å for the clean surface and 10 Å for a surface with graphene adsorbed. The graphene was adsorbed to the surface on four different sites, *ring-top*, *ring-fcc*, *ring-hcp* and *ring-bridge* where the centre of the 6-member carbon ring is above the site given as shown in Figure 7.2.

7.2.4 Surface properties

The inter-sheet binding (cleavage) energy (with units *kJ/mol carbon*) of graphite was calculated relative to single sheets of graphene in equation 7.1.

$$W_{adhesion} = E_{graphite} - E_{graphene} \tag{7.1}$$

The adsorption energy per carbon atom in a graphene sheet (E_{ads}), was calculated for the system in which carbon was adsorbed on the surface ($E_{graphene\ adsorbed}$) relative to the energy of a carbon atom in a single sheet of graphene ($E_{graphene}$) and the clean surface (E_{slab}).

Most of the calculations were performed for a $p(1 \times 1)$ surface, where graphene has a coverage of two carbon atoms per surface cobalt atom and a unit cell containing two surface cobalt atoms (one on each side of the slab). Larger surface unit cells gave similar results.

$$E_{ads} = (E_{graphene\ adsorbed} - E_{slab} - E_{graphene})/4 \tag{7.2}$$

7.2.5 Intrinsic surface error correction

The correction of the surface intrinsic error [21] was included to improve the energies for the surface calculations (see discussion in Chapter 2). The surface energy correction is mapped on the electron density of the surface [22].

As shown in Figure 7.2 the graphene sheets will be adsorbed onto the surface resulting in a new "surface" layer of carbon rather than cobalt. This intrinsic surface energy error will be different for the clean metal and the adsorbed graphene due to different densities. This intrinsic surface error must thus be corrected for the clean slab and the slab with graphene adsorbed. Since the in-plane density of the surface layer is different for the metal and graphene layer, the bulk density can not be used. In this case the electron density in the xy-plane will be used to map the intrinsic surface energy correction (see Figure 7.5).

Previous work by Mattsson suggested two limiting cases for the electron densities to calculate the intrinsic surface energy correction. The bulk density can be used as the lower limit [23] (for atomic vacancy systems) and maximum density in an xy-plane as an upper limit [21]. Mattsson and Jennison [21] suggested a reasonable estimate for the electron density to be used

for the intrinsic surface energy correction, is that at 75% of the jellium density in the surface plane. Unfortunately, the jellium density is not available for these systems and as a reasonable estimate, 75% of the maximum density will be used to find the surface energies and related adsorption energies for graphene as suggested for the surface systems [21].

7.3 Results

7.3.1 Graphene and graphite

In order to establish the ability of the DFT model to describe the graphene system, the graphene lattice parameter in the sheet a was optimized to 2.46 Å using GGA potential and 2.44 Å using the LDA potential. Both values are in good agreement with the experimental lattice parameter of $a = 2.46$ Å [15], with the LDA potential slightly over binding the carbon atoms in the graphene sheet.

The optimum inter-sheet spacing was calculated using the US-LDA potential (see Figure 7.3) and found to be 3.35 Å, which is close to the experimental spacing of 3.336 Å [15]. The PAW-GGA and US-GGA results are virtually indistinguishable for the inter-sheet lattice parameter showing a weak attraction for lattice spacings between 3.8 - 7.0 Å. The LDA potential *seems* to give a better description of the inter-sheet geometry of graphite compared to GGA potentials, but the LDA potential does not contain the required physics to describe the interaction, and this apparent good performance is due to fortituous cancellation of errors [24]. Consequently this functional can not be used with confidence since the errors would not necessarily cancel when graphene is adsorbed on a metal surface.

The minimum energy calculated is the cleavage energy for graphite relative to graphene and is calculated as -2.4 *kJ/mol carbon* (25 *meV/carbon atom*) at a separation of 3.34 Å for the US-LDA potential and -0.3 *kJ/mol car-*

bon for the GGA potentials at a separation of 5 Å. GGA calculations the AAAA sheet configuration showed that the inter-sheet repulsion was stronger below 4 Å suggesting that the ABAB graphite configuration is more stable than the AAAA configuration at c smaller than 4.5 Å.

Experimental inter-sheet binding energies of 35, 43 and 61 *meV/carbon atom* determined by three different experimental techniques have been reported [25, 26, 27]. These energy values differ significantly from each other. The binding energy can be interpreted in various ways as either the "exfoliation" energy (removal of surface sheet via sliding of one sheet over the other) or "adsorption" energy (removal of sheet by lifting) or cleavage energy (removal of sheet from bulk resulting in an infinite separation of all sheets). These three interactions are strictly speaking not the same and would have different magnitudes. The experimental values can thus only give an indication of the magnitude of interaction and not easily be compared to DFT calculated values directly. It is clear that the GGA potentials can not describe the inter-sheet interactions sufficiently since neither the cleavage energy nor the lattice parameter c are in reasonable agreement with experiment.

Similar results have been reported previously for GGA and LDA potentials [24] and explained by the inability of GGA DFT to treat the low electron density regions and therefore the inter-sheet interactions [20, 28]. This inability of DFT in describing these regions of low electron density in graphene and therefore the inter-sheet interactions, is important when considering the adsorption of graphene on to the metal surface. The interaction energy between the graphene sheet and the metal surface will not be described accurately if the electron density between the metal surface and graphene sheet is low. The description of regions with low electron density and the long range non-local Van der Waals interactions is still one the shortcomings of DFT [28, 29]. A scheme for improved treatment of the

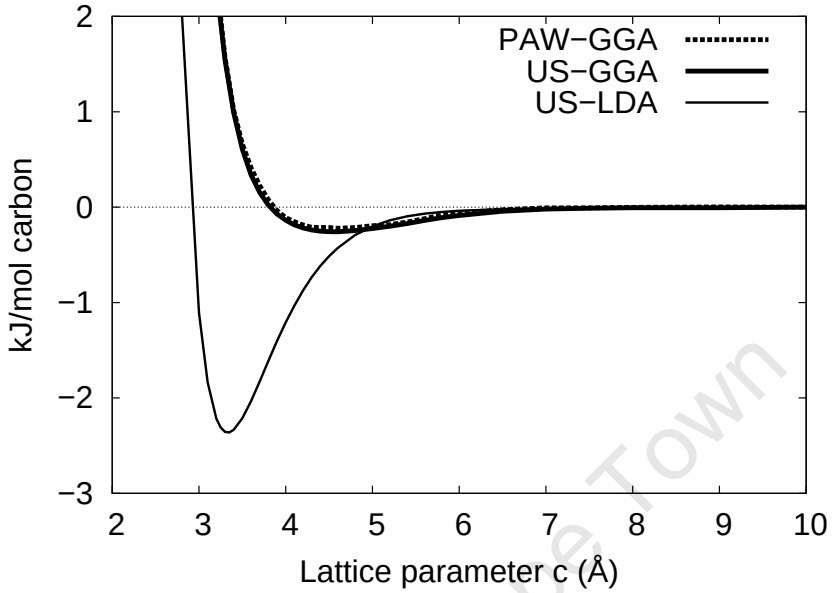

Figure 7.3: Calculation of graphite lattice parameter c showing the different results for the GGA and LDA potentials relative to the energy of a graphene sheet.

low electron density regions of surfaces and vacuum systems has been suggested by Mattsson and Jennison [21] and Mattsson and Mattsson [23] while Van der Waals DFT functionals, which include the London forces are in the process of being developed [28, 29].

The electron densities in the xy-planes were plotted for graphite at different sheet spacings (see Figure 7.4). The summation of density in the xy-plane for various graphene separations indicates that the electron density tail stretches about 4 Å from the centre of the sheet. At this point the repulsion in the GGA potentials starts to increase due to interaction of the p_z electrons of the carbon atoms in the graphene sheet. Even at a spacing of 3 Å the maximum electron density between the planes is very low (less than 0.05 $Å^{-3}$) indicating that the graphite system would not be described accurately by GGA potentials within the DFT approach due to the regions of low electron density.

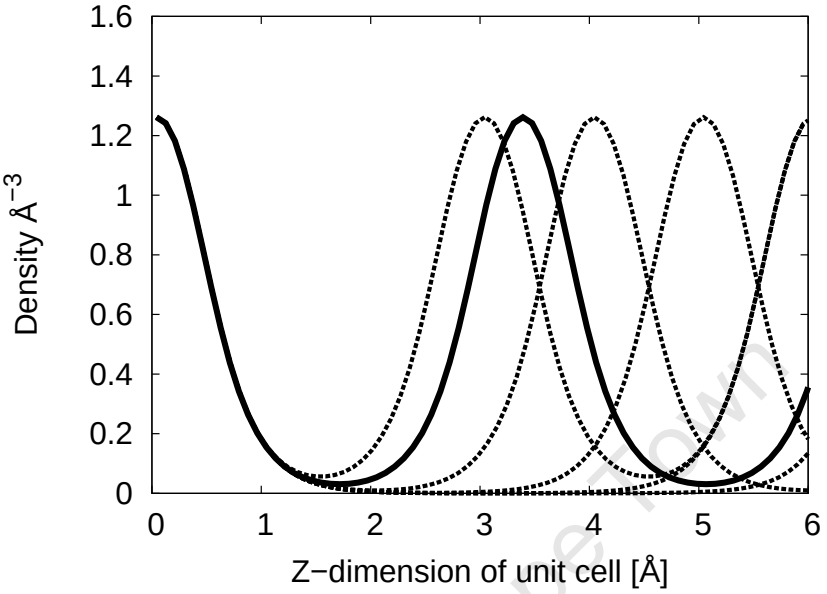

Figure 7.4: Electron densities in xy-cut for graphite with various c lattice spacings. The density distribution for graphite with $c = 3.35$ Å is given by the solid line indicating a very low density between the sheets. For sheet spacings greater than 4 Å the density between the planes become essentially zero.

7.3.2 Graphene on FCC-Co(111)

The adsorption of graphene was investigated for four highly symmetric orientations (*ring-top*, *ring-bridge*, *ring-hcp* and *ring-fcc*) on the FCC-Co(111) surface of which the *ring-bridge*, *ring-hcp* and *ring-fcc* were found to be stable on the surface. For the *ring-top* site where the centre of the carbon ring is above a Co surface atom, the graphene lifted off from the surface without a barrier to a height of 3.8 Å. The *ring-fcc*, *ring-hcp* and *ring-bridge* sites were found to stay close to the surface with Co-C bonding distances of 2.157 Å for the *ring-fcc*, 2.164 Å for the *ring-hcp* and 2.249 Å for the *ring-bridge* adsorption mode. These results are in good agreement with the LEED work reported on Ni [12] where a height of 2.11 Å was reported for the *ring-hcp* adsorption mode. DFT calculations for graphene on Ni also

obtained similar geometries [13, 14]. A slight buckling occurred with the carbon atoms above the hollow sites being slightly closer to the surface than the carbon atoms on top of the metal atoms.

For the *ring-fcc* and *ring-hcp* adsorption states, all the C–C distances were stretched from 1.42 Å for graphene to 1.44 Å of the adsorbed state. This lattice expansion results in matching of the graphene structure with the FCC-Co(111) surface lattice. The expansion of the graphene lattice without the metal present has an energy cost to stretch the bonds of 1.23 *kJ/mol carbon.*

The adsorption of graphene on the FCC-Co(111) surface without the surface energy correction gives a very low work of adhesion as seen in Table 7.1. Checking this energy for various slab thicknesses show that the adsorption energy is converged with slab thickness with an energy variation of about 0.4 *kJ/mol carbon* adsorbed on $ring - fcc$ site and 0.4 *kJ/mol carbon* on the $ring - hcp$ site. Without the intrinsic surface energy correction, the adsorption energy relative to pure graphene (a = 2.46 Å) is about -0.3 (+-0.2) *kJ/mol carbon* for *ring-hcp* (with carbon atoms on *fcc* and *top* positions) and -0.40 (+-0.05) *kJ/mol carbon* for the *ring-fcc* site. This suggests a rather weak adsorption.

Experimental work on Ni [8] suggests that graphene adsorption on the *ring-top* site would be stable but only at a C–Ni distance of 3.10 Å with a height of 2.8 Å above the metal slab. The DFT-LDA calculation by Abild-Pedersen *et al.* [6] found a minimum at a height of 3.22 Å above the Ni surface atoms. The *ring-top* site suggested from experiment [8] with a 2.8 Å could be a physisorbed state bound by a combination of non-bonding Van der Waals forces and orbital interactions as for graphite. It should be noted that the LDA formulation does not contain the underlying physics of Van der Waals forces [24] and gives a poor description of the properties of most transition state metals [16].

Table 7.1: Energies (in *kJ/mol carbon*) for graphene adsorption on a five-layer slab with a FCC-Co(111) surface. The uncorrected energies for the various adsorption sites is given along with the zero-point vibrational energy correction (ZPC) and intrinsic surface error corrections as calculated with the PAW potentials based on the bulk density and 75% of maximum density in the plane.

Site	E_{ads}	ZPC	Bulk corr.	Max. corr.	75% corr.	E'_{ads} [a]
Ring-fcc	-0.45	-0.03	-2.72	-4.63	-3.63	-4.11
Ring-hcp	-0.38	0.03	-2.72	-4.63	-3.63	-3.71
Ring-bri	1.38	-0.13	-2.72	-4.63	-3.63	-2.38
Ring-top	1.23					

[a] E'_{ads} is calculated based on the energy, including the ZPC and intrinsic surface energy correction at 75% of maximum density

The adsorption energies obtained using PAW-GGA potentials are unusually small. Further investigation into the adsorption properties was done to understand why the adsorption energies are so low. The bonding distances for graphene adsorbed on the *ring-hcp* and *ring-fcc* sites are only slightly longer than the sum of Co and C covalent radii. Comparing these Co-C bonding distances of 2.15 Å to the 3.34 Å for the interlayer spacing of graphite suggests that the interaction between the graphene sheet on these sites has a chemical nature and the Van der Waals contribution should be minimal.

An electron density summation was made in the *xy*-planes to determine the electron density between the graphene sheet and the surface (see Figure 7.5). The electron density between adsorbed graphene and the metal slab in the *ring-hcp* site (graphene 2.15 Å above the surface) is similar to the electron density (larger than 0.2 $Å^{-3}$) between metal layers in the slab. The fact that the region between the graphene sheet and the metal is not a low electron density region implies that DFT should be able to predict graphene adsorption on cobalt in the chemisorbed state correctly. On the other hand, the electron density between adsorbed graphene and the metal

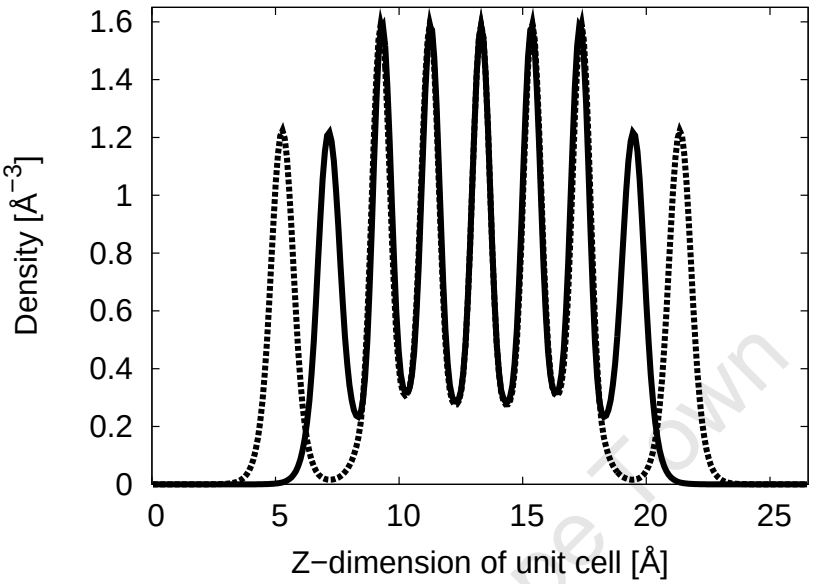

Figure 7.5: Electron densities in *xy*-cut for graphene adsorbed on an FCC-Co(111) surface indicating a similar electron density distribution between the metal and graphene sheet as for the metal sheets in the slab. The density (solid line) is given for graphene adsorbed on the *ring-hcp* site 2.15 Å above surface, while the dashed line is for graphene on the *ring-top* site 3.8 Å above the surface.

slab in the ring-top site (graphene 3.8 Å above the surface) is low (ca. 0.02 Å^{-3}). This adsorption mode can not accurately be described by DFT since Van der Waals interactions are not accounted for.

The adsorption energy needs to be corrected for the intrinsic surface energy error [21, 22] (see Table 7.1). In the lower limit to the correction, the bulk electron density of the metal (0.81 Å^{-3}) is used to determine the surface energy correction. The upper limit of the intrinsic surface error correction is given by the average density in a plane of surface atoms as suggested by Mattsson and Jennison [21]. This maximum electron density was found to be 1.62 Å^{-3} for the FCC-Co(111) sheet and 1.21 Å^{-3} for the adsorbed graphene sheet as calculated with the PAW potentials. As suggested by Mattsson and Jennison [21], 75% of the maximum density was used for the

intrinsic surface energy error mapping. The correction factor for the PW91 exchange-correlation functional and PAW potentials was used as given by Mattsson *et al.* [22]. The correction of the intrinsic surface error then gives an adsorption energy in the order of 4 *kJ/mol carbon* for graphene adsorbed on the *ring-fcc* and *ring-hcp* sites.

An energy analysis for the removal of graphene by graphene lifting was performed, where a flat graphene sheet was lifted from the surface. For this system a much larger vacuum spacing was used of about 28 Å to avoid interaction between the graphene sheets through the vacuum as the graphene was lifted from the surface. The single point energies were calculated for the sheet at various heights above the surface for the graphene adsorbed on the ring-fcc site as seen in Figure 7.6. In the interpretation it should be noted that the graphene remains stretched ($a = 2.501$ Å), therefore the "adsorption energy" at a height of 5 Å is 1.23 *kJ/mol carbon*. This energy is the energy required to stretch the graphene sheet from $a = 2.46$ Å to $a = 2.501$ Å to fit onto the cobalt surface.

This adsorption potential clearly shows that there is a barrier to adsorption. This barrier would be the result of Pauli repulsion, where electrons of the same quantum state interact with a resulting increase in energy and work function. Overlap between the orbitals from the metal and graphene sheets results in stabilization of the chemisorbed state.

7.3.3 Vibrational analysis

Vibrational analysis was performed to establish whether the adsorption states are true local minima and determine the zero-point vibrational energy (ZPVE). The *ring-hcp* and *ring-fcc* had only real frequencies while the *ring-bridge* site had one imaginary frequency (see Table 7.2). This would suggest that the *ring-hcp* and *ring-fcc* were calculated as local minima while the *ring-bridge* is a first order saddle point and therefore a transition state

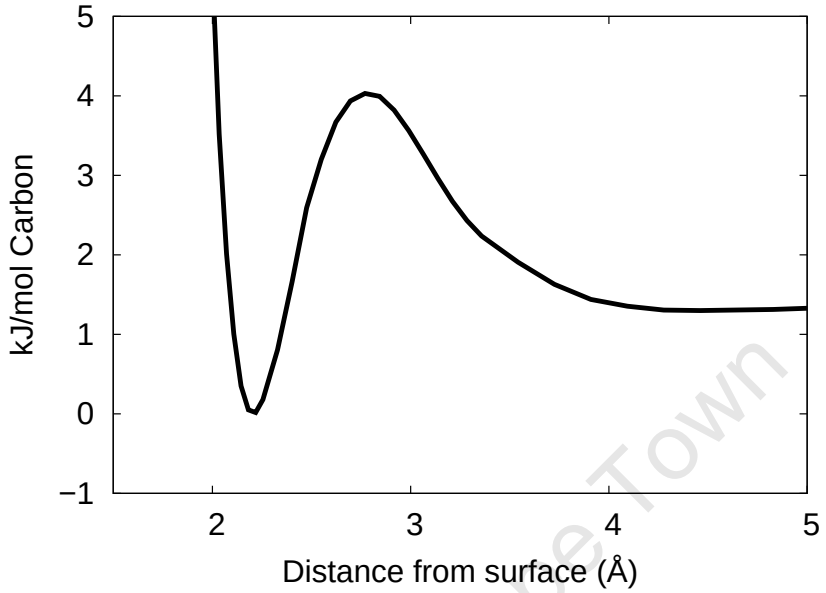

Figure 7.6: Energy profile for graphene lifting perpendicular to the surface atom showing a barrier for the adsorption of graphene on the surface (not corrected for intrinsic surface energy error).

of the translation of the graphene from the *ring-hcp* to *ring-fcc* site. The barrier for the translational movement is rather flat as indicated by the imaginary frequency of 59i cm^{-1}, which is not surprising given the very low energy barrier of 2 *kJ/mol carbon*. A perturbation of the graphene adsorbed on the bridge site in the direction of the imaginary frequency confirmed this.

From the analysis of the vibrational frequencies it could be seen that the high frequency modes at 1555 cm^{-1} for a graphene sheet are softened with adsorption due to a weakening of the intra-sheet bonds. The low frequency modes become larger due to the interaction with the surface, which was not present in the clean single sheet of graphene.

Table 7.2: Frequencies (cm^{-1}) for the carbon atoms of graphene in clean graphene and adsorbed on the various states

Clean	*ring-fcc*	*ring-hcp*	*ring-bridge*
1556	1492	1491	1500
1555	1491	1491	1498
874	708	711	701
16	183	195	177
14	72	74	107
13	71	74	59i

7.3.4 Density of States analysis

Partial density of states analysis was performed where the density of states was decomposed into the projections of *s, p* and *d* orbitals for the carbon and cobalt atoms. The DOS is given relative to the vacuum potential of zero with the Fermi level drawn in. The calculated work function is 5.01 eV for the clean metal and 4.26 eV for a graphene sheet. These values are in good agreement with values reported in literature for graphene of 4.3 eV [9] and 4.6 eV [30] and 5.0 eV for Co [31]. The adsorption of graphene resulted a work function of 3.5 eV. This change in work function is in a similar range to that observed for graphene on Ni where a value of 3.9 eV was reported [10]. Due to the upward shift of the Fermi level some electrons are located in higher energy bands. This would suggest that Pauli repulsion is present as a result of interaction from filled electronic bands of the same quantum state. For graphene adsorption from the gas phase, a crossing barrier is shown in Figure 7.6. The barrier can be explained by the fact that energy levels shift up due to Pauli repulsion as the sheet approaches the surface. If the sheet moves closer to the surface and crosses the barrier, stabilization can occur by bond formation as a result of electrons being transferred to other bands with a lower energy.

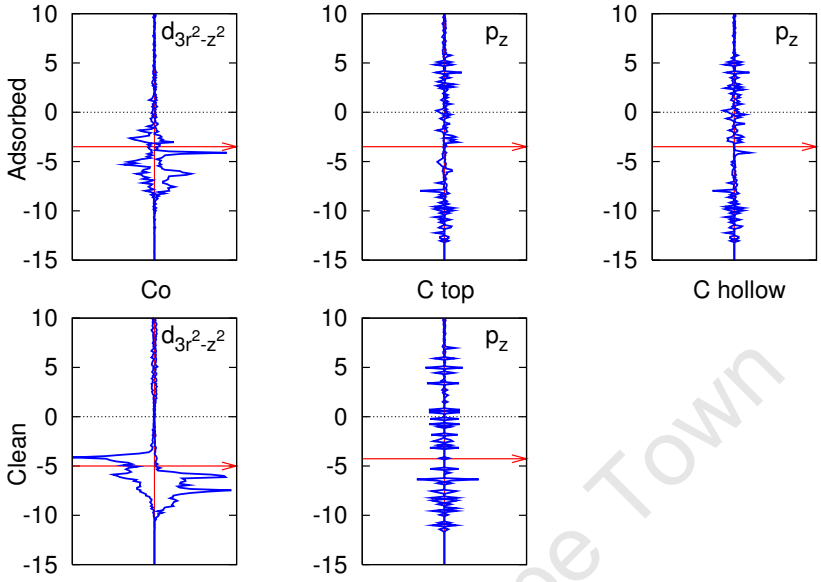

Figure 7.7: Density of states for graphene adsorption on the *ring-fcc* site with all energies given (in eV) relative to a vacuum potential of zero. The Fermi level is drawn in to show the level to which the bands are filled. The DOS for adsorbed system is given on top while the clean metal surface and graphene bands are shown in the bottom row. The α-spin and β-spin is shown with α-spin on the right hand side.

The DOS (see Figure 7.7 for the Co $d_{r^2-z^2}$ and C p_z orbitals) showed changes for the adsorbed system relative to the clean system while the DOS for other orbitals and atoms did not show much difference. The adsorption of graphene results in a splitting of the Co $d_{r^2-z^2}$ bands along with a change in shape, suggesting that the Co $d_{r^2-z^2}$ energy levels are shifted with the bonding of the graphene sheet on the surface. For the adsorbed graphene the electronic states shift to lower energies suggesting that the C p_z orbitals are experiencing a bonding interaction. The bonding of the carbon to the surface is weak since strong mixing peaks of Co $d_{r^2-z^2}$ bands with C p_z bands do not occur.

Comparison of the DOS for the adsorbed carbon atoms above the metal atom and in the hollow site showed that the DOS for both atoms are not

identical. The difference is only within the energy levels between -3.8 eV and 2 eV relative to the Fermi level of the adsorbed system. There is a very small magnetization of the carbon atoms in the graphene sheets with adsorption. This points to a definite electronic interaction with the surface.

7.3.5 Charge analysis

The Bader charge analysis was performed to see whether a redistribution of electrons took place with graphene adsorption as qualitatively suggested by DOS (see discussion in Chapter 2 for details on the method and implementation). The redistribution of electron density from the metal to graphene would suggest bonding of the sheet to the slab, even though the adsorption energy is so low. The charge of the adsorbed system was compared to the clean graphene and the clean metal (see Table 7.3). The absolute charge on the metal and graphene carbon atoms were essentially zero. Adsorption of graphene resulted in a redistribution of charge density; the surface metal atoms lost 0.144 e while the carbon atoms on top gained 0.151 e. An electron charge transfer 0.88 e from Ni to graphene was previously calculated from a Mulliken analysis of DFT results [14]. Experimental work suggested a charge transfer of 0.02 e from Ni to C measured by UPS work [9]. Unfortunately, the height and site was not given for graphene on the surface. It is possible that this could be the Van der Waals bonded graphene at a height of 2.8 Å above the surface on the *ring-top* site as shown in [8].

Very small changes in the charge of the carbon atom above the hollow site and the metal atoms in the bulk were observed, which suggest that a localized charge interaction exists.This charge transfer from the metal to the carbon atom would be indicative of chemical bond formation between carbon atoms above metal atoms.

Table 7.3: Effective charges (e) determined from the Bader analysis of the electron density distribution for graphene adsorbed on the *ring-fcc* site of a 7-layer slab.

Atom	Location	Adsorbed	Clean	Difference
C	hollow	0.029	0.022	0.007
C	top	-0.173	-0.022	-0.151
Co	layer 1	0.125	-0.019	0.144
Co	layer 2	0.020	0.020	0.001

7.4 Discussion

The main focus of the study is to determine the adsorption of graphene on the FCC-Co(111) surface. It is therefore important to establish why DFT fails to describe the graphite system in order to be able to know whether the results for graphene adsorption on the metal surface can be trusted.

7.4.1 Graphene - graphite interaction

The graphene structure calculated here is analogous to the highly orientated pyrolytic graphite (HOPG) [32] in which infinite 2D flat hexagonal sp_2 honeycomb sheets of carbon are π stacked in 3D structure of flat layers. The intra-sheet sp_2-σ-bonds are very strong compared to the weak p_z-π-interaction between the sheets [20, 24, 33, 34]. These intra-sheet σ-bonds are characterized by a substantial electron density, which can be described well using DFT. The inter-sheet bonding is a result of p_z-orbitals of the different sheets interacting with each other [35, 36]. This band interaction between the sheets is responsible for the formation of the ABAB Bernal [37] structure. The electron density between the sheets at a separation of 3.35 Å is very low (see Figure 7.4), suggesting that the sheets are not chemically bound. At these long bonding distances the slight overlap of the orbitals (at the Van der Waals bonding distance) result in Pauli repulsion [33] where

electrons of the same quantum state interact. In the case of graphite this Pauli repulsion is balanced by the weak Van der Waals forces [38], more specifically the London force, which is physically an attractive charge interaction of "virtual dipoles" resulting from polarization due to transient fluctuations in electron density [33]. This effect is a completely non-local electron-electron interaction and in essence, can not be described by the local LDA or semi-local GGA potentials. The LDA and GGA potentials are designed for non-uniform electron gas and fail to capture the essence of the Van der Waals interactions [39]. Although the LDA potentials give a good result for the interlayer spacing, the energy profile at larger distances is different from the potentials based on London forces [20, 40]. The shape of this energy potential is determined by the electron interactions and the Van der Waals interactions are in essence long range correlation effects that should be incorporated in the exchange-correlation term [41]. The long range and non-local parts of the correlation interactions are responsible for the Van der Waals contribution [42].

7.4.2 Graphene adsorption on FCC-Co(111)

The graphene adsorption on *ring-fcc* and *ring-hcp* sites was found to converge at a height of about 2.16 Å while the *ring-bridge* is the transition state for surface diffusion at a similar height above the surface. Along with the electron density plots and other analysis methods, it was shown that graphene has a chemical interaction with the surface on these sites. Chemisorption is typically well described by DFT.

The observed charge transfer and the shifts in the Fermi energy level and electronic levels suggest that the graphene is chemically bound to the surface on the *ring-hcp*, *ring-fcc* and *ring-bridge* sites. In the case of the graphene adsorption on the *ring-hcp*, *ring-fcc* and *ring-bridge* sites, the Pauli repulsion was overcome by the formation of chemical bonds between the graphene

sheet and the surface. This is further supported by the vibrational analysis since the vibrational modes within the sheets are weakened while the modes perpendicular to the surface are strengthened.

The accuracy of this energy is quite important when determining the strength of adsorption. Consequently the zero point vibrational energy correction and intrinsic surface energy corrections were applied. The ZPVE had virtually no effect on the adsorption energy, but the intrinsic surface energy error did make a significant contribution to the energy. This is due to the fact that the electron density of the surface layer is different for a clean metal slab and the adsorbed graphene sheet resulting in a different decay of the electron density into the vacuum. Since the adsorption energy is so small, it is important to apply these corrections to obtain accurate values. In this case the intrinsic surface energy correction is required to account correctly for the polarization of the surface with and without the adsorbed graphene.

The total corrected adsorption energy for graphene is therefore -4 *kJ/mol carbon* when adsorbed on the most stable *ring-hcp*. The energy barrier (corrected) for sliding would would be the adsorption energy on the *ring-bridge* site relative to the *ring-hcp* and *ring-fcc* site of 1.83 *kJ/mol carbon*. The energy for lifting was calculated without the intrinsic surface energy correction since this correction was not determined for the barrier of desorption. The energy of this barrier relative to the *ring-hcp* site is about 4 *kJ/mol carbon* (see Figure 7.6). The C–C bonds in a graphene sheet are much stronger than C–Co bonds as shown by the high frequencies in the vibrational analysis. The C–C bonds are thus more rigid and the carbon sheet would not be easily stretched or compressed within the sheet. Consequently, the movement of a graphene sheet along the direction of the sheet plane would require a concerted movement. The barrier of concerted movement would be given by the energy required per atom as calculated in this study multiplied by the

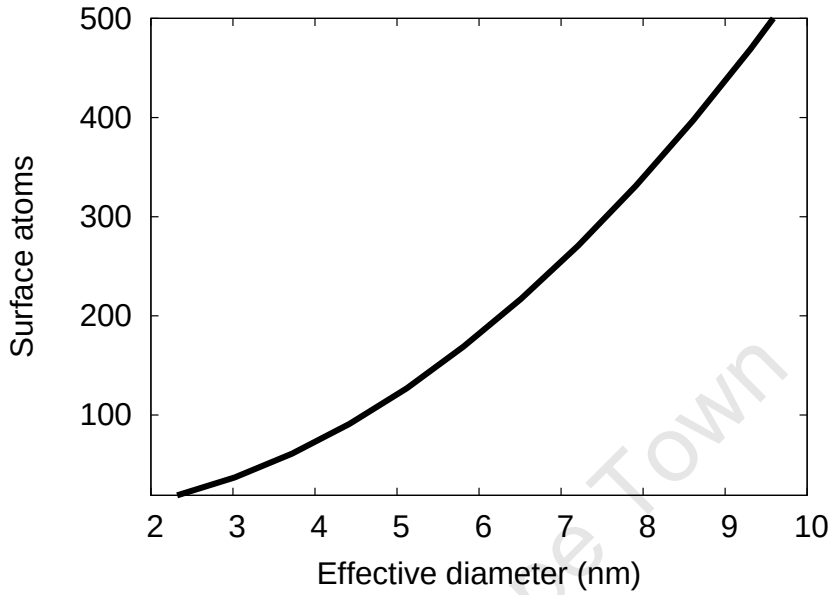

Figure 7.8: The number of surface atoms per plane for a (111) surface of a fcc cubo-octahedron as a function of the effective volume.

number of atoms. The concerted movement of a graphene sheet would be more likely occur via sliding over the surface than lifting off the surface. The vibrational analysis showed that the vibrational modes of a graphene sheet are softer perpendicular to the sheet, suggesting that bending of the sheets is easier than stretching or compression the sheets within the plane. The lifting of a graphene sheet would most likely not occur via a concerted lifting but via bending since less Co–C bonds are required to break simultaneously when lifting occurs via bending.

7.4.3 Graphene on nano-sized cobalt

In order to understand the deactivating role of graphene, the energies determined here must be placed in context of crystallite size. Since the energies calculated above are given essentially per carbon atom the adhesion of the carbon sheet will be directly affected by the number of carbon atoms binding

to the surface. The adhesion of the sheet can be given by the number of surface metal atoms covered by such a graphene sheet. For nano-crystallites a limited number of surface atoms are exposed as described by the Van Hardeveld and Hartog [43] statistics. These statistics were used to determine the number of surface cobalt atoms per crystal face as a function of the crystallite size (see Figure 7.8). A cobalt crystallite size of ca. 3 nm would result in (111) planes containing ca. 37 surface cobalt atoms.

A graphene sheet on a FCC-Co(111) surface has a coverage of 2 carbon atoms per cobalt atom. Although the adsorption energy of -4.11 *kJ/mol carbon* seems low, this can become quite a significant number with an increase in surface size. The energy of removing carbon can be estimated by assuming the adsorption energy is independent of crystallite size and the sheet edge atoms do not affect the adsorption energy. The effect of edge atoms will be negligible when the sheet is either terminated with hydrogen or bent away from the metal surface. The barrier for a concerted diffusion of the graphene sheet from *ring-fcc* to *ring-hcp* over the *ring-bridge* site (2 *kJ/mol carbon*) would be approximately 140 *kJ/mol* of graphene sheet, which contain 70 carbon atoms (for a minimum crystal diameter of ca. 3 nm). The barrier for concerted lifting (4 *kJ/mol carbon*) of the whole sheet would be 280 *kJ/mol* of graphene sheets, which contain 70 atoms on the same size metal surface. This energy is expected to increase for smaller crystallites due to a lowering of the Fermi-level of the metal [44].

If the carbon sheet does not bend away from the surface and the edge atoms of the carbon sheet is not terminated with hydrogen, the sheets try to saturate the sp_2-like bonds of the carbon atoms in the sheet by bending in such a way that the surface metal atoms can saturate these bonds (see semi infinite clusters in the previous chapter and Monte Carlo study by Amara *et al.* [45]). These clusters would probably be even less mobile due to the strong bonding interaction of the terminating carbon atoms.

7.5 Conclusions

The adsorption of graphene on the FCC-Co(111) surface was shown to be due to chemical interaction for the *ring-hcp*, *ring-fcc* and *ring-bridge* adsorption states. The *ring-bridge* is the transition state for the sliding of the sheet from *ring-fcc* to the *ring-hcp* position. The graphene has to overcome Pauli repulsion when adsorbing on the surface, resulting in an increase in the work function of the surface and also a splitting of the $d_{r^2-z^2}$ bands. Charge transfer from the metal to the graphene sheet was observed along with a weakening of the vibrational modes within the graphene sheets with adsorption. A weaker physisorbed state was also found, but due to poor description of the London type Van der Waals forces, this can not be characterized properly.

Graphene would be more likely to slide than lift off the surface if a concerted movement is assumed. The energy cost of sliding would increase with the size of the sheet and become prohibitive for very large sheets.

References

[1] Menon, P.G., J. Mol. Catal. 59 (1990), 207.

[2] Bartholomew, C.H., Appl. Catal. A: Gen. 212 (2001), 17.

[3] Sault, A.G., Datye, A.K., J. Catal. 140 (1993), 136.

[4] Helveg, S., Lopez-Cartes, C., Shested, J., Hansen, P.L., Clausen, B.S., Rostrup-Nielsen, J.R., Abild-Pedersen, F., Nørskov, J.K., Nature 427 (2004), 426.

[5] Moulijn, J.A., Van Diepen, A.E., Kapteijn, F., Appl. Catal. A: Gen. 212 (2001), 3.

[6] Abild-Pedersen, F., Nørskov, J.K., Rostrup-Nielsen, J.R., Sehested, J., Helveg, S., Phys. Rev. B 73 (2006), 115419.

[7] Shelton, J.C., Patil, H.R., Blakely, J.M., Surf. Sci. 43 (1974), 493.

[8] Rosei, R., De Crescenzi, M., Sette, F., Quaresima, C., Savoia, A., Perfetti, P., Phys. Rev. B 28 (1983), 1161.

[9] Rosei, R., Modesti, S., Sette, F., Quaresima, C., Savoia, A., Perfetti, P., Phys. Rev. B 29 (1984), 3416.

[10] Nagashima, A., Tejima, N., Oshima, C., Phys. Rev. B 50 (1994), 17487.

[11] Souzu, Y., Tsukada, M., Surf. Sci., 326 (1995), 42.

[12] Gamo, Y., Nagashima, A., Wakabayashi, M., Terai, M., Oshima, C., Surf. Sci. 374 (1997), 61.

[13] Kalibaeva, G., Vuilleumier, R., Meloni, S., Alavi, A., Ciccotti, G., Rosei, R., J. Phys. Chem. B 110 (2006), 3638.

[14] Wang, S.G., Liao, X.Y., Cau, C.B., Li. Y.W., Wang, J., Jiao, H., J. Phys. Chem. 111 (2007), 10894.

[15] Baskin, Y., Meyer, L., Phys. Rev. 100 (1955), 544.

[16] Swart, J.C.W., Van Helden, P., Van Steen, E., J. Phys. Chem. C 111 (2007), 4998.

[17] Ceperley, A.C., Alder, B.J., Phys. Rev. Lett. 45 (1980), 566.

[18] Perdew, J.P., Zunger, A., Phys. Rev. B 23 (1981), 5048.

[19] Monkhorst, H.J., Pack, J.D., Phys. Rev. B 13 (1976), 5188.

[20] DiVincenzo, D.P., Mele, E.J., Holzarth, N.A.W., Phys. Rev. B 27 (1983), 2458.

[21] Mattsson, A.E., Jennison, D.R., Surf. Sci. 520 (2002), L611. ‘

[22] Mattsson, A.E., Armiento, R., Schultz, P.A., Mattsson, T.R., Phys. Rev. B 73 (2006), 195123.

[23] Mattsson, T.R., Mattsson, A.E., Phys. Rev. B 66 (2002), 214110.

[24] Hasegawa, M., Nisidate, K., Phys. Rev. B 70 (2004), 205431.

[25] Girifalco, L.A., Lad, R.A., J. Chem. Phys. 25 (1956), 693.

[26] Benedict, L.X., Chopra, N.G., Cohen, M.,L., Zettl, A., Louie, S.G., Crespi, V.H., Chem. Phys. Lett. 286 (1998), 490.

[27] Zacharia, R, Ulbricht, H., Hertel, T., Phys. Rev. B 69 (2004), 155406.

[28] Rydberg, H., Dion, M., Jacobson, N., Scrö der, E., Hyldgaard, P., Simak, S.I., Langreth, D.C., Lundqvist, B.I., Phys. Rev. Lett. 91 (2003), 126402.

[29] Rydberg, H., Lundqvist, B.I., Langreth, D.C., Dion, M., Phys. Rev. B 62 (2000), 6997.

[30] Takahashi, T., Tokailin, H., Sagawa, T., Phys. Rev. B 32 (1985), 8317.

[31] Michaelson, H.B., J. Appl. Phys. 48 (1977), 4729.

[32] Ooi, N., Rairkar, A., Adams, J.B., Carbon 44 (2006), 231.

[33] Brenan, R.O., J. Chem. Phys. 20 (1952), 40.

[34] Schabel, M.C., Martins, J.L., Phys. Rev. B 46 (1992), 1785.

[35] Yoshizawa, K., Kato, T., Yamabe, T., J. Chem. Phys. 105 (1996), 2099.

[36] Yoshizawa, K., Yumura, T., Yamabe, T., Bandow, S., J. Am. Chem. Soc. 122 (2000), 11871.

[37] Bernal, J.D., Proc. Roy. Soc. Lond. A 106 (1924), 749.

[38] Cotton, F.A., Wilkinson, G,. "Advanced Inorganic Chemistry", 4th ed., Wiley, New York, (1980).

[39] Kohn, W., Meir, Y., Makarov, D.E., Phys. Rev. Lett. 80 (1998), 4153.

[40] Girifalco, L.A., Hodak, M., Phys. Rev. B 65 (2002), 125404.

[41] Charlier, J.C., Gonze, X., Michenaud, J.P., Europhys. Lett. 28 (1994), 403.

[42] Langreth, D.C., Dion, M., Rydberg, H., Scröder, E., Hylgaard, P., Lundqvist, B.I., J. Quantum Chem. 101 (2005), 599.

[43] Van Hardeveld, R., Hartog, F., Surf. Sci. 15 (1969), 189.

[44] Phala, N.S., Van Steen, E., Gold Bulletin 40 (2007), 150.

[45] Amara, H., Bichara, C., Ducastelle, F., Surf. Sci. 602 (2008), 77.

Part V

Conclusions

Chapter 8

Overview of Findings and Outlook

8.1 Limitations of using DFT to calculate surface energies

8.1.1 Intrinsic surface energy correction

In Chapters 3 and 4 the size dependent surface energies of cobalt and CoO were determined. The surface energies for low coordinated atoms were calculated from hexagonal and octagonal rods. The surface energy contributions had to be corrected for the intrinsic surface energy error, which is inherent to GGA-DFT surface calculations. Good agreement of calculated surface energies and experimental surface energies was found. Uncorrected surface energies gave coordination dependent bonding energies with similar trends as previous work on other metals. Correcting for the intrinsic surface energy error, however, gave a linear relationship between the surface energy and coordination number.

Although this correction is perhaps not the most elegant way of determining correct surface energies, it is based on exact theories of exchange and correlation interactions. The electron density provides a useful way of mapping intrinsic surface energy error. Hence, this method is based on suitable theory and addresses the problems of the GGA functionals independent of the system studied. This approach is more fundamental than the use of LDA functionals, which contains an inadequate level of theory to describe surfaces, while providing a seemingly good result. It should be noted that the use of LDA in the case of transition metals (such as cobalt) will not result in a proper description of bulk properties, and thus the derived surface properties cannot be fundamentally correct.

The calculation of the surface energies of CoO also required correction for the intrinsic surface energy error inherent of GGA functionals. Questions can be raised regarding the applicability of this method to ionic systems, in which electron density can be highly localised. The correction was compared

for other well studied ionic materials such as NaCl, MgO and NiO. For all these ionic materials, the surface energy correction resulted in surface energies comparable with experimental results. This is a very interesting finding since the surface energies of ionic materials can thus be greatly under predicted by both GGA and LDA functionals. This intrinsic surface energy error correction should thus be applied for any surface calculation performed with GGA functionals.

8.1.2 Strong correlation interaction

CoO is a Mott insulator characterized by antiferromagnetism and a band gap. These properties originates from the strong electron correlation interactions when the electrons are paired. The strong correlation prevents pairing and consequently the antiferromagnetic structure and the band gap is formed. Due to the fact that these strong correlation effects of excited electronic states are not well described at LDA- and GGA-DFT level a more advanced theory is required. This can be addressed by the computationally rather inexpensive DFT+U approach. Other approaches such as using hybrid functionals with exact exchange has also been shown to provide the good predictions of the band gaps of Mott insulators. These functionals, however, do not inherently describe strong electron correlation effects and are computationally much more expensive.

The DFT+U approach is an *ad hoc* correction based on the principles, which defines the Mott insulators. DFT+U provides a way of penalising a paired state by increasing the on-site Coulomb interaction (U) of paired electrons in the same orbital. The formulation in VASP is based on using $U - J$ (U_{eff}) to penalize the paired (correlated) electronic state. A value of $U_{eff} = 5\ eV$ was found to give a good representation of the measurable physical properties such as the band gap, crystal structure, lattice distortion and magnetization. This value is close to the empirical value of $U_{eff} =$

4.9 eV suggested by Anisimov *et al.* (1991) to give a good representation of the band gap.

8.1.3 Current status of computational chemistry

In this thesis, the many boundaries were pushed in an attempt to obtaining quantitative information from DFT calculations by systematically correcting for known limitations. Given the problematic systems encountered in this work and the limitations of the GGA functionals, it is thus necessary to include the intrinsic surface energy correction for metals as well as ionic materials to obtain accurate surface energies. Although the DFT+U approach and the intrinsic surface energy correction are not *ab-initio* approaches, they systematically correct the errors by using a level of theory suitable to address the shortcomings of the GGA functionals.

Caution was taken to avoid using levels of theory which are unable to describe the physics of the particular systems, while providing good results, but for the wrong reasons. An example here is the use of LDA functionals in the calculation of surface energies and graphene sheets where Van der Waals interactions are at play. A more advanced functional capable of calculating exact correlation and exact exchange is the "holy grail" of computational chemistry, since such a functional would have chemical accuracy and provide quantitative results. In the meantime, the most efficient way of obtaining useful results for these problematic systems is by systematically correcting for the known limitations of these functionals.

8.2 Size dependent surface energies

The size-dependent surface energy can be estimated using a simple broken bond model for FCC and HCP type of metals and in the case of ionic systems a combination of the electro-static interaction and a broken bond model.

The linear relationship between the surface energy and the coordination number of the surface atom for FCC type of metals supports a broken bond type of model for estimation of surface energies. Size dependent surface energies can easily be calculated from purely broken bond interactions, since long range interactions do not contribute largely to the surface energy of these systems. This method allows for the estimation of surface energies of crystallites far beyond the capability of quantum-chemical methods. The use of this approach for BCC-type of metals, however, remains questionable, since nearest and next nearest neighbour interactions are at play.

Ionic interactions can act over long ranges which makes the determination of size dependent surface energies more involved than a simple nearest neighbour broken bond approach. Since CoO is not a purely ionic material, the Bader charge analysis was used to determine the effective ionic charge on each ion. The magnitude of the charge was found to be +1.3 e for Co and -1.3 e for oxygen. A pure charge-interaction gave a much lower surface energy than the corrected surface energy calculated from the DFT+U method. Consequently, the broken bond energy was estimated from the difference between the DFT+U energy and the purely ionic interaction. The use of both electro-static interactions and the broken bond method can be rationalized based on the partial charge obtained for the ions within the structure. The partial charge implies a partial ionic and thus also a partial covalent bonding within the structure. Hence, the surface energy needs to take into account both effects. The use of a combination of electrostatic and broken bond methods for ionic materials has not been demonstrated previously. This might open up some opportunities for estimating thermodynamic properties of large ionic systems beyond the reach of more advanced theories.

8.3 Catalyst deactivation

8.3.1 Size dependent sintering

Size dependent surface energies were calculated for cobalt nanocrystallites of various shapes. The chemical potential was found to increase substantially for smaller crystallites. Therefore the driving force exists to reduce the chemical potential of small crystallites by reducing the number of surface atoms. Sintering can occur as a result of coalescence of smaller crystallites yielding larger crystallites resulting in a reduction of the chemical potential. This thermodynamic driving force to reduce the relative number of surface atoms is detrimental to the catalytic activity since fewer surface atoms are available to catalyse the elementary steps of the Fischer-Tropsch synthesis.

Supports are commonly used to anchor active metal crystallites and slow down the sintering process. Due to the increased chemical potential of small crystallites relative to large crystallites, the melting temperatures of small crystallites are lower than for large crystallites. Sintering processes are known to be significantly faster close to the melting temperature due to the enhanced mobility of surface atoms. Strong support interactions can thus be negated by the enhanced mobility of small crystallites resulting in fast sintering. This is a serious consequence in the light of catalyst deactivation since the sintering of highly dispersed crystallites can not be avoided. This creates a major constraint when improving the activity per mass of catalyst by increasing the dispersion, since the highly dispersed catalysts would simply sinter to larger crystallites in a short space of time resulting in fast initial catalyst deactivation.

The size dependent melting model predicts small crystallites below 2 nm to be in the liquid phase. Crystallites with diameters smaller than 9.3 nm have Hüttig temperatures below the cobalt Fischer-Tropsch operating temperatures. These crystallites would be likely to sinter due to the high mobil-

ity of surface atoms. Sintering via transport of gas phase metal atoms are not expected to be a problem due to the very low partial pressures of gas phase metal atoms.

Since sintering processes are typically slow and difficult to quantify experimentally, this fundamental understanding of why small crystallites sinter quickly would be useful in explaining fast initial deactivation of highly dispersed catalysts. Since sintering is not only applicable to catalysis but other fields of materials science. The approach followed in this study can be used to obtain a more fundamental understanding of sintering behaviour of highly dispersed materials.

8.3.2 Size dependent oxidation

A thermodynamic model inclusive of size dependent surface energies was used to calculate the sizes at which small crystallites are expected to oxidize. Previously van Steen *et al.* (2005) predicted that crystallites below 4.5 nm would be oxidized under realistic Fischer-Tropsch synthesis conditions ($p_{H2O}/p_{H2} > 1$). Careful calculations of size dependent surface energies using the DFT+U method with surface energies corrected for the intrinsic surface energy error suggested the surface energies to be much higher (1.55 J/m^2) than the value originally predicted by van Steen *et al.* (2005) of 0.45 J/m^2. Consequently, only crystallites below 2.1 nm are at risk of oxidation. This evidence suggests that long debated matter of oxidation would not be a problem for a Co-based Fischer-Tropsch catalyst. This finding is consistent with experimental evidence as contextualized by van de Loosdrecht *et al.* (2007) in a review on oxidation as a deactivation mechanism.

8.3.3 Carbon deposition

Carbon deposition was investigated by calculating the stability of carbon clusters which would be intermediates in the formation of carbon overlayers.

These clusters were found to be very stable and therefore a significant driving force for the formation of carbon sheets exist. The energy barrier to diffusion was found to be very low, suggesting diffusion to be facile on the flat FCC-Co(111) surface. Small linear clusters are more stable than atoms, but when branching takes place and aromatic clusters are formed, the clusters become very stable. The build up of carbon deposits on large flat FCC-Co(111) surfaces can thus not be prevented due to the large thermodynamic driving force of carbon cluster formation. The likelihood of the formation of carbon deposits can be reduced by preventing C–C coupling of pure carbon species by ensuring that enough hydrogen is available on the surface. C–H species would prevent the formation of large graphene species since a carbon sheet can not grow where a C–H bond is present. The carbon clusters can have a "poisoning" effect if they remain on the surface since they prevent gas phase molecules form accessing the surface.

The interaction of graphene clusters with the surface was also investigated. The adsorption energy for these clusters was found to be very small. Three adsorption states were found where the sheet has a chemical interaction with the metal surface. This was confirmed by DOS, work function and charge analysis. One of the adsorption states was found to be a transition state for diffusion with a barrier of 2 *kJ/mol carbon* for a concerted movement. The barrier for a concerted lifting was found to be 4 *kJ/mol carbon* which is much higher than for sliding. These values are small per atom, but can become prohibitive for large sheets. Since the adsorption energy scales with the number of atoms interacting with the surface, large graphene sheets would be more difficult to remove. This will also lead to lower catalytic activity since gas phase molecules can not access the surface which catalyses the Fischer-Tropsch reaction.

Although deactivation by carbon formation is thermodynamically favoured, the formation of carbon deposits can be inhibited by ensuring enough hydro-

gen is available on the surface to prevent the formation of carbon clusters. Some authors suggested the use of other metal atoms to "selectively poison" the surface for carbon deposition, but depending on the nature of these "selective poisons" the intrinsic activity of the catalyst can be affected.

Appendix A

Thermodynamic Methods

A.1 Basic thermodynamics

The change in internal energy (dU) of any closed system is determined by taking into account the work (dW) and the heat (dQ) in the process.

$$dU = dW + dQ \tag{A.1}$$

The change in work for a condensed phase can be written in terms of the change in volume with constant area (dV) and the change in area at constant volume (dA)

$$dW = -PdV + \sigma dA \tag{A.2}$$

The heat term can be written as

$$dQ = TdS \tag{A.3}$$

$$dU = TdS - PdV + \sigma dA \tag{A.4}$$

The enthalpy is defined as

$$H = U - TS \tag{A.5}$$

and derivation gives

$$dH = dU - TdS - SdT \tag{A.6}$$

while the Gibbs free energy is defined as

$$G = H + PV \tag{A.7}$$

and derivation gives

$$dG = dH + PdV + VdP. \tag{A.8}$$

$$dG = (dU - TdS - SdT) + PdV + VdP \tag{A.9}$$

$$dG = \Big((-PdV + \sigma dA + TdS) - TdS - SdT\Big) + PdV + VdP \tag{A.10}$$

$$dG = -SdT + VdP + \sigma dA \tag{A.11}$$

This can be written for the overall quantities and also for the molar properties

$$d\left(\frac{G}{n}\right) = -\frac{S}{n}dT + \frac{V}{n}dP + \sigma d\left(\frac{A}{n}\right) \tag{A.12}$$

Where $\frac{G}{n} = \mu$ is the molar Gibbs free energy, S is the entropy, V is the volume and D is the dispersion which is a molar property.

A.2 Thermodynamics of finely dispersed systems

For nano-sized spheres, the chemical potential (μ) is not only affected by temperature and pressure, but also the size of the sphere. The contribution of the surface tension to the energy becomes significant for spheres in the nanometer range. This energy contribution of the surface will increase the chemical potential of the crystallite.

A rigorous formulation of the dispersion dependent chemical potential is thus required in order to describe these systems. The size dependent equilibrium between of the solid(s) vs liquid(l) and metal vs metal-oxide are of interest for catalytic purposes. The solid vs liquid transition equilibrium would affect the melting temperature which has an effect on sintering while the metal vs metal-oxide affects the size dependent oxidation behaviour.

Some assumptions on the system can further simplify the size dependent chemical potential. In the case of a gas bubble enclosed by by a liquid surface, a change in size can be realised by changing the volume inside the bubble as well as the enclosing surface while keeping the number of moles gas inside the bubble constant. The change in surface area will co-inside with a change of volume and molar volume (or concentration). Consequently the pressure will increase for small crystallites. The resulting expression is

essentially the Laplace relation for size dependence.

$$P^r - P^\infty = \frac{2\sigma}{r} \tag{A.13}$$

In the case of a nano-size liquid droplet, a change in area results in a change in volume and number of moles since the molar volume (or concentration) remains essentially constant due to the limited compressibility of the liquid. For a liquid droplet only the density remains constant with a change in surface area, volume and the number of moles. The density can be removed from the derivative leaving the derivative of the dispersion. Since the compressibility of condensed matter is very small the pressure term can be neglected and at constant temperature the temperature term can be neglected as well.

The chemical potential for the condensed liquid sphere with is thus given as

$$d\mu = \frac{\sigma}{\rho} d\left(\frac{A}{V}\right) \tag{A.14}$$

$$d\mu = \frac{\sigma}{\rho} dD \tag{A.15}$$

$$\mu_l^r - \mu_l^\infty = \frac{3\sigma_l}{\rho_l r} \tag{A.16}$$

The surface energy can be determined relative to the surface area (with units J/m^2) or relative to the number of exposed surface atoms (with units of kJ/mol surface atoms). The former is more suitable for spherical liquid droplets with surfaces which are not anisotropic while the latter is more suited for solids with different types of atoms exposed at the surface.

The surface energy for a solid can then be written relative to the surface energy per unit area $\gamma(r)$ as

$$d\mu_s = \frac{\gamma(r)}{\rho_s} dD_s. \tag{A.17}$$

For a given crystal shape and size, the van Hardeveld and Hartog statistics can be used to determine the number of surface and total atoms in a crystal where m is a parameter that describes the size of the crystal.

The surface tension of a liquid is isotropic and assumed to be independent of the size or curvature. The size dependence of the surface energy should thus be included to give an accurate size dependent chemical potential. For solids however, the surface energy is anisotropic and depends on the surface atoms exposed showed in Chapter 3.

For solids the surface energy can be given by the average molar surface energy per exposed surface atom $E_{surf}(m)$ (with units of kJ/mol surface atoms). This was done for the Cobalt metal by incorporating the coordination dependent broken bond model from Chapter 3 with the van Hardeveld and Hartog statistics for idealized nano-crystals

$$E_{surf}(m) = \frac{\sum \gamma_i(C)}{N_S(m)} \tag{A.18}$$

where $\gamma_i(C)$ is the surface energy contribution of surface atom i with a coordination C and $N_S(m)$ is the total number of surface atoms. See Chapter 4 for the approach used to determine the size-dependent surface energies of CoO. The size dependent dispersion can be calculated from

$$D = \frac{number\ of\ surface\ atoms}{number\ of\ total\ atoms\ in\ crystal} = \frac{N_S(m)}{N_T(m)}. \tag{A.19}$$

For a cubo-octahedron, the total number of atoms ($N_T(m)$) is given by

$$N_T(m) = 16m^3 - 33m^2 + 24m - 6 \tag{A.20}$$

where m is the number of atoms along a ridge while the total number of surface atoms ($N_S(m)$) is given by

$$N_S(m) = 30m^2 - 60m + 32 \tag{A.21}$$

The dispersion of the solid can then be written as a function of the size parameter m

$$D(m) = \frac{30m^2 - 60m + 32}{16m^3 - 33m^2 + 24m - 6} \tag{A.22}$$

If the crystal shape is known (eg. octahedron), the size dependent surface energy can be written in terms of an equivalent spherical diameter r_s. The equivalent spherical diameter is determined as the diameter of the sphere with the same volume as crystal (V_s) with a given size and shape.

$$r_s = \left(\frac{V_s}{(4/3)\pi}\right)^{\frac{1}{3}} \tag{A.23}$$

$$r_s(m) = \left(\frac{N_T(m)}{(4/3)\pi\rho_s}\right)^{\frac{1}{3}} \tag{A.24}$$

The size dependent chemical potential can then be written as

$$d\mu_s = d[E_{surf}(m)D_s(m)] \tag{A.25}$$

$$\mu_s^r - \mu_s^\infty = E_{surf}(m)D_s(m). \tag{A.26}$$

A.3 Size dependent melting

In the case of a solid-liquid transition, the number of metal atoms remain constant. In the equilibrium calculation it would also be assumed that the metal is either in liquid or solid state and not a solid core with liquid shell.

For solid-liquid equilibrium of a single component of highly dispersed material the equilibrium condition is $\mu^l = \mu^s$ for the condensed solid and liquid phases.

The thermodynamic expression for the size dependent chemical potential for a solid is

$$\mu_s(T, P, D_s) = \mu_s^0 - s_s dT + v_s dP + \frac{\gamma}{\rho_s} dD_s \tag{A.27}$$

and similarly for a liquid

$$\mu_l(T, P, D_l) = \mu_l^0 - s_l dT + v_l dP + \frac{\sigma}{\rho_l} dD_l \tag{A.28}$$

The integrals of dT must be evaluated from the bulk reference condition (T_0) to the temperature of interest (T) for the droplet or crystallite with a specific size. The dispersion term is evaluated at the dispersion of interest to a dispersion of zero which is the bulk condition where dispersion does not affect the energy $D_0 = 0$.

For spherical droplets, the dispersion term can be written as

$$D_l = \left(\frac{A_l}{V_l}\right) \tag{A.29}$$

The expression for the size dependent chemical potential of the liquid can then be written where $v_l = 1/\rho_l$ as

$$\mu_l(T, P, D) = \mu_l^0 - s_l dT + v_l dP + \frac{\sigma}{\rho_l} dD_l \tag{A.30}$$

$$\mu_l(T, P, D) = \mu_l^0 - s_l dT + \frac{3\sigma}{\rho_l}\left(\frac{-1}{r_l^2}\right) dr_l \tag{A.31}$$

This expression can be evaluated from a dispersion at the radius r_l to $r = \infty$ giving

$$\mu_l(T, P, D) = \mu_l^0 - s_l dT + \frac{3\sigma}{\rho_l}\left(\frac{1}{r_l}\right) \tag{A.32}$$

A similar expression can be written for the solid state if the surface is isotropic

$$\mu_s(T, P, D) = \mu_s^0 - s_s dT + \frac{3\gamma}{\rho_s}\left(\frac{-1}{r_s^2}\right) dr_s \tag{A.33}$$

Integration over the radius of interest and an infinitely large crystal would

give

$$\mu_s(T,P,D) = \mu_s^0 - s_s dT + \frac{3\gamma}{\rho_s}\left(\frac{1}{r_s}\right) \tag{A.34}$$

A mass balance would give the expression to connect r_s and r_l

$$\rho_l V_l = \rho_s V_s \tag{A.35}$$

$$(4/3)\pi r_l^3 = \frac{\rho_s}{\rho_l}(4/3)\pi r_s^3 \tag{A.36}$$

$$r_l = \left(\frac{\rho_s}{\rho_l}\right)^{1/3} r_s \tag{A.37}$$

For the liquid, the equilibrium expression would then be

$$\mu_l(T,P,D) = \mu_l^0 - s_l dT + \frac{3\sigma}{\rho_l}\left(\frac{\rho_l}{\rho_s}\right)^{1/3}\left(\frac{1}{r_s}\right) \tag{A.38}$$

The total equilibrium is then

$$\mu_l^0 - s_l dT + \frac{3\sigma}{\rho_l}\left(\frac{\rho_l}{\rho_s}\right)^{1/3}\frac{1}{r_s} = \mu_s^0 - s_s dT + \frac{3\gamma}{\rho_s}\left(\frac{1}{r_s}\right) \tag{A.39}$$

$$0 = \mu_s^0 - \mu_l^0 - (s_s - s_l)dT + \frac{3\gamma}{\rho_s}\left(\frac{1}{r_s}\right) - \frac{3\sigma}{\rho_l}\left(\frac{\rho_l}{\rho_s}\right)^{1/3}\left(\frac{1}{r_s}\right) \tag{A.40}$$

$$0 = \Delta H_{fus}\left(\frac{T}{T_\infty} - 1\right) + \frac{3\gamma}{\rho_s r_s}\left(1 - \frac{\sigma}{\gamma}\left(\frac{\rho_s}{\rho_l}\right)^{2/3}\right) \tag{A.41}$$

$$\frac{T}{T_\infty} = 1 - \frac{3\gamma}{\rho_s r_s \Delta H_{fus}}\left(1 - \frac{\sigma}{\gamma}\left(\frac{\rho_s}{\rho_l}\right)^{2/3}\right) \tag{A.42}$$

When taking the surface anisotropy of the solid into account, the follow-

ing expression can be derived:

$$\mu_s(T,P,D) = \mu_s^0 - s_s dT + v_s dP + d[E_{surf}(m)D_s(m)] \tag{A.43}$$

For the solid $dP = 0$ and evaluation of the dispersion from the size of interest to the bulk where $D_s = 0$ gives

$$\mu_s(T,P,D) = \mu_s^0 - s_s dT + d[E_{surf}(m)D_s(m)] \tag{A.44}$$

The final expression for the equilibrium is thus

$$\mu_l(T,P,D_l) = \mu_s(T,P,D_s) \tag{A.45}$$

$$\mu_l^0 - s_l dT + \frac{3\sigma}{\rho_l}\frac{1}{r_l} = \mu_s^0 - s_s dT + d[E_{surf}(m)D_s(m)] \tag{A.46}$$

$$0 = \mu_s^0 - \mu_l^0 - (s_s - s_l)dT + d[E_{surf}(m)D_s(m)] - \frac{3\sigma}{\rho_l}\frac{1}{r_l} \tag{A.47}$$

Integration from the diameter d to infinity gives

$$0 = \Delta H_{fus}\left(\frac{T}{T_\infty} - 1\right) + E_{surf}(m)D_s(m) - \frac{3\sigma}{\rho_l^{2/3}}\left(\frac{4\pi}{3N_T(m)}\right)^{\frac{1}{3}} \tag{A.48}$$

$$\frac{T}{T_\infty} = 1 - \frac{1}{\Delta H_{fus}}\left(E_{surf}(m)D_s(m) - \frac{3\sigma}{\rho_l^{2/3}}\left(\frac{4\pi}{3N_T(m)}\right)^{\frac{1}{3}}\right) \tag{A.49}$$

A.4 Reaction equilibria

A.4.1 Formation of Carbonyls

The size dependent formation of carbonyls $Co(CO)_x$ can be determined by using the size dependent chemical potential of the solid relative to the gas

phase. The reaction for the formation of carbonyls can be written as follows

$$2Co + 8CO \rightleftharpoons Co_2(CO)_8 \tag{A.50}$$

$$4Co + 12CO \rightleftharpoons Co_4(CO)_{12} \tag{A.51}$$

$$6Co + 16CO \rightleftharpoons Co_6(CO)_{16} \tag{A.52}$$

At equilibrium

$$a\mu_{Co}(T,P,D) + b\mu_{CO}(T,P) = \mu_{Co_a(CO)_b}(T,P) \tag{A.53}$$

$$a\mu_{Co}(T,P,D) = a\mu^0_{Co} + av_{Co}dP - as_{Co}dT + aE_{surf}(m)dD_{Co}(m) \tag{A.54}$$

$$b\mu_{CO}(T,P) = b\mu^0_{CO} + bv_{CO}dP - bs_{CO}dT \tag{A.55}$$

$$\mu_{Co_a(CO)_b}(T,P) = \mu^0_{Co_a(CO)_b} + v_{Co_a(CO)_b}dP - s_{Co_a(CO)_b}dT \tag{A.56}$$

Rearranging gives

$$\mu^0_{rxn} = \mu^0_{Co_a(CO)_b} - a\mu^0_{Co} - b\mu^0_{CO} \tag{A.57}$$

$$s_{rxn} = s_{Co_a(CO)_b} - as_{Co} - bs_{CO} \tag{A.58}$$

$$-\mu^0_{rxn} + s_{rxn}dT + aE_{surf}(m)dD_{Co}(m) = (v_{Co_a(CO)_b} - av_{Co} - bv_{CO})dP \tag{A.59}$$

The molar volume of Co (v_{Co}) is negligible compared to the gas phase species and the effect of temperature is not important since μ^0 is calculated at the temperature of interest, thus

$$-\mu^0_{rxn} + aE_{surf}(m)dD_{Co}(m) = (v_{Co_a(CO)_b} - bv_{CO})dP \tag{A.60}$$

$$-\mu^0_{rxn} + aE_{surf}(m)dD_{Co}(m) = RT\left(\frac{1}{P_{Co_a(CO)_b}} - b\frac{1}{P_{CO}}\right)dP \tag{A.61}$$

$$-\mu^0_{rxn} + aE_{surf}(m)dD_{Co}(m) = RTln\left(\frac{P_{Co_a(CO)_b}}{{P_{CO}}^b}\right) \tag{A.62}$$

A.4.2 Formation of CoO

The size dependent formation of CoO can also be determined for the following reaction

$$Co + H_2O \rightleftharpoons CoO + H_2 \tag{A.63}$$

At equilibrium

$$\mu_{Co}(T, P, D_{Co}) + \mu_{H_2O}(T, P) = \mu_{CoO}(T, P, D_{CoO}) + \mu_{H_2}(T, P) \tag{A.64}$$

The chemical potential terms are defined as follows

$$\mu_{Co}(T, P, D_{Co}) = \mu^0_{Co} - s_{Co}dT + v_{Co}dP + E^{surf}_{CoO}(m)dD_{Co}(m) \tag{A.65}$$

$$\mu_{H_2O}(T, P) = \mu^0_{H_2O} - s_{H_2O}dT + v_{H_2O}dP \tag{A.66}$$

$$\mu_{CoO}(T, P, D_{CoO}) = \mu^0_{CoO} - s_{CoO}dT + v_{CoO}dP + E^{surf}_{CoO}(m)dD_{CoO}(m) \tag{A.67}$$

$$\mu_{H_2}(T, P) = \mu^0_{H_2} - s_{H_2}dT + v_{H_2}dP \tag{A.68}$$

The following reaction properties are defined

$$\mu^0_{rxn} = \mu^0_{CoO} + \mu^0_{H_2} - \mu^0_{Co} - \mu^0_{H_2O} \tag{A.69}$$

The change in equilibrium constant with temperature is not important, thus $dT = 0$. Integration of the size is from D to $D^\infty = 0$. equating with equilibrium equation gives

$$-\mu^0_{rxn} = \Big(-v_{Co} - v_{H_2O} + v_{CoO} + v_{H_2}\Big)dP - E^{surf}_{Co}(m)D_{Co}(m) + E^{surf}_{CoO}(m)D_{CoO}(m) \tag{A.70}$$

The molar volumes v_{Co} and v_{CoO} are negligible compared to the gas phase, thus

$$-\mu^0_{rxn} = \Big(- v_{H_2O} + v_{H_2}\Big)dP - E^{surf}_{Co}(m)D_{Co}(m) + E^{surf}_{CoO}(m)D_{CoO}(m) \tag{A.71}$$

$$-\mu^0_{rxn} = RT\left(- \frac{1}{P_{H_2O}} + \frac{1}{P_{H_2}}\right)dP - E^{surf}_{Co}(m)D_{Co}(m) + E^{surf}_{CoO}(m)D_{CoO}(m) \tag{A.72}$$

$$-\mu^0_{rxn} = RTln\left(\frac{P_{H_2}}{P_{H_2O}}\right) - E^{surf}_{Co}(m)D_{Co}(m) + E^{surf}_{CoO}(m)D_{CoO}(m) \tag{A.73}$$

$$-RTln\left(\frac{P_{H_2}}{P_{H_2O}}\right) = \mu^0_{rxn} - E^{surf}_{Co}(m)D_{Co}(m) + E^{surf}_{CoO}(m)D_{CoO}(m) \tag{A.74}$$

A.5 Additional Info

Table A.1: Thermodynamic data

Species	Cp	H_f	G_f	T_{melt}
	J/mol.K	kJ/mol	kJ/mol	K
Co[a]	24.8	0.0	0.0	1769
CoO[a]	55.2	-237.9	-214.2	2103
H_2[a]	28.8	0.0	0.0	
H_2O[a]	33.6	-241.8	-228.3	
CO[a]	29.1	-110.5	-137.2	

[a] Information from Lide, D.R., Kehiaian, H.V., "CRC Handbook of Thermophysical and Thermochemical Data", CRC Press, Inc., 1994

Bibliography

Abild-Pedersen, F., Nørskov, J.K., Rostrup-Nielsen, J.R., Sehested, J., Helveg, S., Phys. Rev. B 73 (2006), 115419. "Mechanisms for catalytic carbon nanofiber growth studied by *ab-initio* Density Functional Theory calculations"

Abild-Pedersen, F., Andersson, M.P., Surf. Sci. 601 (2007), 1747. "CO adsorption energies on metals with correction for high coordination adsorption sites: A density functional study"

Adamo, C., Barone, V., J. Chem. Phys. 110 (1999), 6158. "Toward reliable density functional methods without adjustable parameters: The PBE0 model"

Amara, H., Bichara, C., Ducastelle, F., Phys. Rev. B 73 (2006), 113404. "Formation of carbon nanostructures on nickel surfaces: A tight-binding grand canonical Monte Carlo study"

Amara, H., Bichara, C., Ducastelle, F., Surf. Sci. 602 (2008), 77. "Interaction of carbon clusters with Ni(100): Application to the nucleation of carbon nanotubes"

Anderson, R.B., in "The Fischer-Tropsch Synthesis", Academic Press, Inc., 1984.

Anderson, Y., Langreth, D.C., Lunqvist, B.I., Phys. Rev. Lett. 76 (1996), 102. "Van der Waals Interactions in Density-Functional Theory"

Anisimov, V.I., Korotin, M.A., Kurmaev, E.Z., J. Phys.: Cond. Matt. 2 (1990), 3973. "Band-structure description of Mott insulators (NiO, MnO, FeO, CoO)"

Anisimov, V.I., Zaanen, J., Andersen, O.K., Phys. Rev. B 44 (1991), 943. "Band theory and Mott insulators: Hubbard U instead of Stoner I"

Aschroft, N. W., Mermin, N. D., in "Solid State Physics", Holt, Rinehart and Winston, New York, 1976.

Astier, M., Teichner, S.J., Vergnon, P., p. 63, "Sintering and Catalysis" in Materials Science Research, Volume 10, "Sintering and Catalysis", Kuczynski, G.C., ed., Plenum Press, 1975.

Atkins, P.W., "Physical Chemistry", Sixth edition, Oxford University Press, 1998.

Barbier, A., Tuel, A., Arcon, I., Kodre, A., Martin, G.A., J. Catal. 200 (2001), 106. "Characterization and catalytic behavior of Co/SiO_2 catalysts: Influence of dispersion in the Fischer-Tropsch reaction"

Bartholomew, C.H., Appl. Catal. A: Gen. 212 (2001), 17. "Mechanisms of catalyst deactivation"

Baskin, Y., Meyer, L., Phys. Rev. 100 (1955), 544. "Lattice constants of graphite at low temperatures"

Becke, A.D., Int. J. Quant. Chem. 23 (1983), 1915. "Hartree-Fock Exchange Energy of an Inhomogeneous Electron Gas"

Becke, A.D., J. Chem. Phys. 85 (1986), 1784. "On the large-gradient behavior of the density functional exhange energy"

Becke, A.D., J. Chem. Phys. 98 (1993), 5648. "Density Functional termochemistry. III. The role of exact exchange"

Becke, A.D., J. Chem. Phys. 109 (1998), 2092. "A new inhomogeneity parameter in density-functional theory"

Benedict, L.X., Chopra, N.G., Cohen, M.,L., Zettl, A., Louie, S.G., Crespi, V.H., Chem. Phys. Lett. 286 (1998), 490. "Microscopic determination of the interlayer binding energy in graphite"

Bengaard, H.S., Nørskov, J.K., Shested, J., Clausen, B.S., Nielsen, L.P., Molenbroek, A.M., Rostrup-Nielsen, J.R., J. Catal. 209 (2002), 365. "Steam reforming and graphite formation on Ni catalysts"

Bernal, J.D., Proc. Roy. Soc. Lond. A 106 (1924), 749. "The structure of graphite"

Besenbacher, F., Chorkendorff, I., Clausen, B.S., Hammer, B., Molenbroek, A.M., Nørskov, J.K., Stensgaard, I., Science 279 (1998), 1913. "Design of a surface alloy catalyst for steam reforming"

Bezemer, G.L., Bitter, J.H., Kuipers, H.P.C.E., Oosterbeek, H., Holewijn, J.E., Xu, X., Kapteijn, F., Van Dillen, A.J., de Jong, K.P., J. Am. Chem. Soc. 128 (2006), 3956. "Cobalt particle size effects in the Fischer-Tropsch reaction studied with carbon nanofiber supported catalysts"

Blöchl, P.E., Phys. Rev. B 50 (1994), 17953. "Projector augmented wave method"

Boettger, J.C., Phys. Rev. B 49 (1994), 16798. "Nonconvergence of surface energies obtained for thin-film calculations"

Borwein, D., Borwein, J.M., Taylor, K.F., J. Math. Phys. 26 (1985), 2999. "Convergence of lattice sums and Madelung's constant"

Brandow, B.H., Adv. Phys. 26 (1977), 651. "Electronic structure of Mott insulators"

Bredow, T., Gerson, A,R., Phys. Rev. B 61 (2000), 5194. "Effect of exchange and correlation on bulk properties of MgO, NiO, and CoO"

Brenan, R.O., J. Chem. Phys. 20 (1952), 40. "The interlayer binding in graphite"

Bromfield, T.C., Currula Ferré, D., Niemantsverdriet, J.W., Chem. Phys. Chem. 6 (2005), 254. "A DFT study of the adsorption and dissociation of CO on Fe(100): Influence of surface coverage on the nature of accessible adsorption states"

Brookes, N.B., Law, D,S-L., Warburton, D.R., Wincott, P.L., Thornton, G., J. Phys.: Cond. Matt. 1 (1989), 4267. "Transition-metal monoxides: Band or Mott insulators? Angle-resolved photoemission results for CoO"

Buffat, P., Borrel, J.-P., Phys. Rev. A 13 (1976), 2287. "Size effect on the melting temperature of gold nanoparticles"

Castell, M.R., Dudarev, S.L., Briggs, G.A.D., Sutton, A.P., Phys. Rev. B 59 (1999), 7342. "Unexpected differences in the surface electronic structure of NiO and CoO observed by STM and explained by first-principles theory"

"Catalyst Handbook", Second edition. Wolfe Pbulishing Ltd., 1970.

Ceperley, A.C., Alder, B.J., Phys. Rev. Lett. 45 (1980), 566. "Ground state of the electron gas by a stochastic method"

Charles, E., Sykes, H., Williams, F.J., Tikhov, S., Lambert, R.M., J. Phys. Chem. B 106 (2002), 5390. "Nucleation, growth, sintering, mobility and adsoprtion properties of small gold particles on polycrystalline titania"

Charlier, J.C., Gonze, X., Michenaud, J.P., Europhys. Lett. 28 (1994), 403. "Graphite Interplanar Bonding: Electronic Delocalization and Van der Waals Interaction."

Chen, J.P., Sorensen, C.M., Klabunde, K.J., Hadjipanayis, G.C., Phys. Rev. B 51 (1995), 11527. "Enhanced magnetization of nanoscale colloidal cobalt particles"

Cheng, J., Gong, X.-Q., Hu, P., Martin Lok, C., Ellis, P., French, S., J. Catal. 254 (2008) 285. "A quantitative determination of reaction mechanisms from density functional theory calculations: Fischer-Tropsch synthesis on flat and stepped cobalt surfaces"

Cinquini, F., Giordano, L., Pacchioni, G., Ferrari, A.-M., Pisani, C., Roetti, C., Phys. Rev. B 74 (2006), 165403. "Electronic structure of NiO/Ag(100) thin films from DFT+U and hybrid functional DFT approaches"

Ciobîcă, I.M., Van Santen, R.A., J. Phys. Chem. 107 (2003), 3808. "Carbon monoxide dissociation on planar and stepped Ru(0001) surfaces"

Ciobîcă, I.M., Van Santen, R.A., Van Berge, P.J., Van de Loosdrecht, J., Surf. Sci. 602 (2008), 17. "Adsorbate induced reconstruction of cobalt surfaces"

Ciobîcă, I.M., Van Santen, R.A., Van Berge, P.J., Van de Loosdrecht, J., Surf. Sci. 602 (2008), 17. "Adsorbate induced reconstruction of cobalt surfaces"

Ciobîcă, I.M., PhD Thesis, "The Molecular Basis of the Fischer-Tropsch Reaction", Technical University of Eindhoven, The Netherlands, 2002.

Cotton, F.A., Wilkinson, G,. "Advanced Inorganic Chemistry", 4th ed., Wiley, New York, (1980).

Lide, D.R., Kehiaian, H.V., "CRC Handbook of Thermophysical and Thermochemical Data", CRC Press, Inc., 1994.

Curulla-Ferré, D., Govender, A., Bromfield, T.C., Niemantsverdriet, J.W., J. Phys. Chem. B 110 (2006), 13897. "A DFT study of the adsorption and dissociation of CO on sulfur-precovered Fe(100)"

Cyrot-Lackmann, F., Surf. Sci. 15 (1969), 535. "On the calculation of surface tension in transition metals"

Da Silva, J.L.F., Stampfl, C., Scheffler, M., Phys. Rev. Lett. 90 (2003), 066104. "Adsorption of Xe atoms on metal surfaces: New insights from first-principles calculations"

Derbyshire, F.J., Carbon 13 (1975), 189. "Kinetics of the deposition of pyrolitic carbon on nickel"

Desjonquères, M.C., Spanjaard, D., J. Phys. C: Solid State Phys. 15 (1982), 4007. "A simple chemisorption theory and its application to transition adatoms on transition metals"

Dick, K., Dhanasekaran, T., Zhang, Z., Meisel, D., J. Am. Chem. Soc. 124 (2002), 2313. "Size-dependent melting of silica-encapsulated gold nanoparticles"

DiVincenzo, D.P., Mele, E.J., Holzarth, N.A.W., Phys. Rev. B 27 (1983), 2458. "Density-functional study of interplanar binding in graphite "

Dobson, J.F., Wang, J., Phys. Rev. Lett. 82 (1999), 2123. "Successful test of a seamless Van der Waals density functional"

Dry, M.E., Chapter 4, "The Fischer-Tropsch Synthesis" in "Catalyst Science and Technology", Springer Verlag, New York, 1981

Dry, M.E., Catal. Today 71 (2002), 227. "The Fischer-Tropsch process: 1950-2000"

Dudarev, S.L., Botton, G.A., Savrasov, S.Y., Humphreys, C.J., Sutton, A.P., Phys. Rev. B 57 (1998), 1505. "Electron-energy-loss spectra and the structural stability of nickel oxide: An LSDA+U study"

Efremenko, I., Sheintuch, M., Surf. Sci. 414 (1998), 148. "Quantum chemical study of small palladium clusters"

Ernzerhof, M., Scuseria, G.E., J. Chem. Phys. 110 (1999), 5029. "Assessment of the PerdewBurkeErnzerhof exchange-correlation functional"

Espinoza, R.L., Steynberg, A.P., Jager, B., Vosloo, A.C., Appl. Catal. A: Gen. 186 (1999), 13. "Low temperature Fischer-Tropsch synthesis from a Sasol perspective"

Evjen, H.M., Phys. Rev. 39 (1932), 675. "On the stability of certain heteropolar crystals"

Feibelman, P.J., Hammer, B., Nørskov, J.K., Wagner, F., Scheffler, M., Stumpf, R., Watwe, R., Dumesic, J., J. Phys. Chem. B 105 (2001), 4018. "The CO/Pt(111) puzzle"

Felton, R.C., Prutton, M., Tear, S.P., Welton-Cook, M.R., Surf. Sci. 88 (1979), 474. "A LEED analysis of the CoO(100) surface"

Feng, X., Phys. Rev. B 69 (2004), 155107. "Electronic structure of MnO and CoO from the B3LYP hybrid density functional method"

Finocchi, F., Goniakowski, J., Surf. Sci. 601 (2007), 4144. "The effects of exchange and correlation on the computed equilibrium shapes of wet MgO crystallites"

Fiorentini, V., Methfessel, M., J. Phys.: Cond. Matt. 8 (1996), 6525. "Extracting convergent surface energies from slab calculations"

Font Freide, J.J.H.M., Gamlin, T.D., Hensman, J.R., Nay, B., Sharp, C., J. Nat. Gas Chem. 13 (2004), 1. "Development of a CO_2 tolerant Fischer-Tropsch catalyst: From laboratory to commercial-scale demonstration in Alaska"

Gajdoš, M., Eichler, A., Hafner, J., J. Phys.: Cond. Matt. 16 (2004), 1141. "CO adsorption on close-packed transition and noble metal surfaces: trends from *ab-initio* calculations"

Gamo, Y., Nagashima, A., Wakabayashi, M., Terai, M., Oshima, C., Surf. Sci. 374 (1997), 61. "Atomic structure of monolayer graphite formed on Ni(111)"

Ge, Q., Neurock, M., J. Phys. Chem. B 110 (2006), 15368. "Adsorption and activation of CO over flat and stepped Co surfaces: A first principles analysis"

Geerlings, J.J.C., Wilson, J.H., Kramer, G.J., Kuipers, H.P.C.E., Hoek, A., Huisman, H.M., Appl. Catal. A: Gen. 186 (1999), 27. "Fischer-Tropsch technology - from active site to commercial process"

Gerber, I.C., Ángyán, J.G., J. Chem. Phys. 126 (2007), 44103. "London dispersion forces by range-separated hybrid density functional with second order perturbational corrections: The case of rare gas complexes"

Geus, J.W., p. 29 "Preparation and thermostability of supported metal catalysis" in Materials Science Research, Volume 10, "Sintering and Catalysis", Kuczynski, G.C., ed., Plenum Press, 1975.

Girifalco, L.A., Lad, R.A., J. Chem. Phys. 25 (1956), 693. "Energy of cohesion, compressibility, and the potential energy functions of the graphite systems"

Girifalco, L.A., Hodak, M., Phys. Rev. B 65 (2002), 125404. "Van der Waals binding energies in graphitic structures"

Golosovsky, I.V., Mirebeau, I., André, G., Tovar, M., Tobbens, D.M., Kurdyukov, D.A., Kumzerov, Y.A., Phys. of the Solid State 48 (2006), 2130. "Magnetic phase transition in a nanostructured antiferromagnet CoO embedded in porous glass"

Grinberg, I., Yourdshahyan, Y., Rappe, A.M., J. Chem. Phys. 117 (2002), 2264. "CO on Pt(111) puzzle: A possible solution"

Gruver, V., Young, J., Engman, J., Robota, H.J., Prepr. Pap. Am. Chem. Soc. Div. Pet. Chem. 50 (2005), 164. "The role of accumulated carbon in deactivating cobalt catalysts during FT synthesis in a slurry bubble-column reactor"

Guisnet, M., Magnoux, P., Appl. Catal. A: Gen. 212 (2001), 83. "Organic chemistry of coke formation"

Gunnarsson, O., Andersen, O.K., Jespen, O., Zaanen, J., Phys. Rev. B 39 (1989), 1708. "Density-Functional calculation of the parameters in Andersen model: Application to Mn in CdTe"

Hafner, J., Comp. Phys. Comm. 177 (2007), 6. "Materials simulations using VASP a quantum perspective to materials science"

Hammer, B., Norskov, J.K., Surf. Sci. 343 (1995), 211. "Electronic factors determining the reactivity of metal surfaces"

Hammer, B., Morikawa, Y., Nørskov, J.K., Phys. Rev. Lett. 76 (1996), 2141. "CO chemisorption at metal surfaces and overlayers"

Hammer, B., Hassen, L.B., Nørskov, J.K., Phys. Rev. B 59 (1999), 7413. "Improved adsorption energetics within Density-Functional Theory using revised Perdew-Burke-Ernzerhof functionals"

Hanszen, K.-J., Z. Phys. 157 (1960), 523. "Theoretische untersuchungen über den schmelzpunkt kleiner kügelchen; Ein beitrag zur thermodynamik ger grenzflächen"

Van Hardeveld, R., Hartog, F., Surf. Sci. 15 (1969), 189. "The statistics of surface atoms and surface sites on metal crystals"

Hasegawa, M., Nisidate, K., Phys. Rev. B 70 (2004), 205431. "Semi-empirical approach to the energetics of interlayer binding in graphite"

Helveg, S., Lopez-Cartes, C., Shested, J., Hansen, P.L., Clausen, B.S., Rostrup-Nielsen, J.R., Abild-Pedersen, F., Nørskov, J.K., Nature 427 (2004), 426. "Atomic-scale imaging of carbon nanofibre growth"

Henkelman, G., Arnaldsson, A., Jónsson, H., Comput. Mater. Sci. 36 (2006), 254. " A fast and robust algorithm for Bader decomposition of charge density"

Ho, S-W., Houalla, M., Hercules, D.M., J. Phys. Chem. 94 (1990), 6396. "Effect of particle size on CO hydrogenation activity of silica supported cobalt catalysts"

Hoffman, R., in "Solids and Surfaces: A Chemist's View of Bonding in Extended Structures" VCH Publishers, Inc., 1988.

Hoffmann, R., "Solids and Surfaces: A chemist's view of bonding in extended structures", VCH Publishers, Inc., 1988

Hohenberg, P., Kohn, W., Phys. Rev. 136 (1964), B864. "Inhomogeneous electron gas"

Horn, K., Scheffler, M., Eds. in "Handbook of Surface Science: Electronic Structure", Volume 2, Elsevier, 2000.

Hugosson, H.W., Eriksson, O., Jansson, U., Ruban, A.V., Souvatzis, P., Abrikosov, I.A., Surf. Sci. 557 (2004), 243. "Surface energies and work

functions of the transition metal carbides"

Hult, E., Rydberg, H., Lindqvist, B.I., Langreth, D.C., Phys. Rev. B 59 (1999), 4708. "Unified treatment of asymptotic Van der Waals forces"

Iglesia, E., Appl. Catal. A: Gen. 161 (1997), 59. "Review: Design, synthesis and use of cobalt-based Fischer-Tropsch synthesis catalysts"

Isaak, D.G., Cohen, R.E., Mehl, M.J., Singh, D.J., Phys. Rev. B 47 (1993), 7720. "Phase stability of wüstite at high pressure from first-principles linearized augmented plane-wave calculations"

Jager, B., Espinoza, R., Catal. Today 23 (1995), 17. "Advances in low temperature Fischer-Tropsch synthesis"

Janak, J.F., Phys. Rev. B 18 (1978), 7165. "Proof that $\partial E/\partial n_i = \varepsilon_i$ in density functional theory"

Jaramillo, J., Scuseria, G.E., Ernzerhof, M., J. Chem. Phys. 118 (2003), 1068. "Local hybrid functionals"

Jauch, W., Reehuis, M., Bleif, H.J., Kubanek, F., Pattison, P., Phys. Rev. B 64 (2001), 052102. "Crystallographic symmetry and magnetic structure of CoO"

Jauch, W. Reehuis, M., Phys. Rev. B 65 (2002), 125111. "Electron density distribution in paramagnetic and antiferromagnetic CoO: A γ-ray diffraction study"

Jiang, D.E., Carter, E.A., Surf. Sci. 547 (2003), 85. "Adsorption and diffusion energetics of hydrogen atoms on Fe(110) from first principles"

Kalibaeva, G., Vuilleumier, R., Meloni, S., Alavi, A., Ciccotti, G., Rosei, R., J. Phys. Chem. B 110 (2006), 3638. "*Ab-initio* simulation of carbon clustering on an Ni(111) surface: A model of the poisoning of Nickel-based catalysts"

Kernavanois, N., Ressouche, E., Brown, P.J., Henry, J.Y., Lelièvre-Berna, E., J. Phys.: Cond. Matter. 15 (2003), 3433. "Magnetization distribution in paramagnetic CoO: A polarized neutron diffraction study"

Kim, M.S., Rodriguez, N.M., Baker, R.T.K., J. Catal. 143 (1993), 449. "The interplay between sulfur adsorption and carbon deposition on cobalt

catalysts"

Kitakami, O., Sato, H., Shimada, Y., Sato, F., Tanaka, M., Phys. Rev. B 56 (1997), 1384. "Size effect on the crystal phase of cobalt fine particles"

Kohn, W. Sham, L.J., Phys. Rev. 137 (1965), 1697. "Quantum density oscillations in an inhomogeneous electron gas"

Kohn, W., Sham, L.J., Phys. Rev. 140 (1965), A1133. "Self-consistent equations including exchange and correlation effects"

Kohn, W., Meir, Y., Makarov, D.E., Phys. Rev. Lett. 80 (1998), 4153. "Van der Waals energies in Density Functional Theory"

Kohn, W., Mattsson, A.E., Phys. Rev. Lett. 81 (1998), 3487. "Edge electron gas"

Kresse, G., Furthmuller, J., Comput. Mat. Sci. 6 (1996), 6. "Efficiency of *ab-initio* total energy calculations for metals and semiconductors using a plane-wave basis set"

Kresse, G., Furthmuller, J., Phys. Rev. B 54 (1996), 11169. "Efficient iterative schemes for *ab-initio* total-energy calculations using a plane-wave basis set "

Kresse, G., Hafner, J., Phys. Rev. B 47 (1993), 558. "*Ab-Initio* molecular dynamics for liquid metals"

Kresse, G., Hafner, J., Phys. Rev. B 49 (1994), 14251. "*Ab-initio* molecular-dynamics simulation of the liquid-metal-amorphous-semiconductor transition in germanium"

Kresse, G., Hafner, J., J. Phys.: Cond. Matt. 6 (1994), 8245. "Norm-conserving and ultrasoft pseudopotentials for first-row and transition elements"

Kresse, G., Joubert, J., Phys. Rev. B 59 (1999), 1758. "From ultrasoft pseudopotentials to the projector augmented-wave method"

Kresse, G., Gil, A., Sautet, P., Phys. Rev. B 68 (2003), 073401. "Significance of single-electron energies for the description of CO on Pt(111)"

Kurth, S., Perdew, J.P., Phys. Rev. B 59 (1999), 10461. "Density-functional correction of random-phase-approximation correlation with results for jel-

lium surface energies"

Landrum, G.A., Dronskowski, R., Angew. Chem. Int. Ed. 39 (2000), 1560. "The orbital origins of magnetism: From atoms to molecules to ferromagnetic alloys"

Langreth, D.C., Perdew, J.P., Phys. Rev. B 15 (1977), 2884. "Exchange-correlation energy of a metallic surface: Wave-vector analysis"

Langreth, D.C., Dion, M., Rydberg, H., Scröder, E., Hylgaard, P., Lundqvist, B.I., J. Quantum Chem. 101 (2005), 599. "Van der Waals Density Functional theory with applications"

Lee, D., Lee, J., Ihm, S., Appl. Catal. 36 (1988), 199. "Effect of carbon deposits on carbon monoxide hydrogenation over alumina-supported cobalt catalyst"

Lee, Y.H., Kim, S.G., Tomanek, D., Phys. Rev. Lett. 78 (1997), 2393. "Catalytic growth of single-wall carbon nanotubes: An *ab-initio* study"

Lehtinen, K.E., Zacariah, M.R., Phys. Rev. B 63 (2001), 205402. "Effect of coalescence energy release on the temporal shape evolution of nanoparticles"

Leichtenstein, A.I., Anisimov, V.I., Zaanen, J., Phys. Rev. B 52 (1995), R5467. "Density-functional theory and strong interactions: Orbital ordering in Mott-Hubbard insulators"

Li, H., Jensen, J.H., Theor. Chem. Acc. 107 (2002), 211. "Partial Hessian vibrational analysis: The localization of the molecular vibrational energy and entropy"

Li, B., Michaelides, A., Scheffler, M., Phys. Rev. B 76 (2007), 075401. "Density Functional Theory study of flat and stepped NaCl(001)"

von Lilienfield, O.A., Tavernelli, I., Rothlisberger, U., Sebastiani, D., Phys. Rev. Lett. 93 (2004), 153004. "Optimization of effective atom centered potentials for London dispersion forces in Density Functional Theory"

Liu, S.-R. Zhai, H.-J., Wang, L.-S., Phys. Rev. B 64 (2001), 153402. "Electronic and structural evolution of Co_n clusters (n= 1–108) by photoelectron spectroscopy"

Liu, Z.-P., Hu, P., J. Am. Chem. Soc. 125 (2003), 1958. "General rules for predicting where a catalytic reaction should occur on metal surfaces: A

Density Functional Theory study of C–H and C–O bond breaking/making on flat, stepped and kinked metal surfaces"

Liu, W., Liu, X., Zheng, W.T., Jiang, Q., Surf. Sci. 600 (2006), 257. "Surface energies of several ceramics with NaCl structure"

Lu, H.M., Jiang, Q., J. Phys. Chem. B 108 (2004), 5617. "Size-dependent surface energies of nanocrystals"

Martínez, A. Prieto. G., J. Catal. 245 (2007), 470. "Breaking the dispersion-reducibility dependence in oxide-supported cobalt nanoparticles"

Mason, S.E., Grinberg, I., Rappe, A.M., Phys. Rev. B 69 (2004), 161401(R). "First-principles extrapolation method for accurate CO adsorption energies on metal surfaces"

Masson, A., Métois, J.J., Kern, R., Surf. Sci. 27 (1971), 463. "Migration Brownienne de cristallites sur une surface et relation avec l'épitaxie: I. Partie expérimentale"

Mattsson, A.E., Kohn, W., J. Chem. Phys. 115 (2001), 3441. "An energy functional for surfaces"

Mattsson, A.E., Jennison, D.R., Surf. Sci. 520 (2002), L611. "Computing accurate surface energies and the importance of electron self-energy in metal/metal-oxide adhesion"

Mattsson, T.R., Mattsson, A.E., Phys. Rev. B 66 (2002), 214110. "Calculating the vacancy formation energy in metals: Pt, Pd, and Mo"

Mattsson, A.E., Schultz, P.A., Desjarlais, M.P., Mattsson, T.R., Leung, K., Mod. Simul. Mater. Sci. Eng. 13 (2005), R1. "Designing meaningful density functional calculations in materials science: A primer"

Mattsson, A.E., Armiento, R., Schultz, P.A., Mattsson, T.R., Phys. Rev. B 73 (2006), 195123. "Nonequivalence of the generalized gradient approximations PBE and PW91"
http://dft.sandia.gov/functionals/webcalculator.html

Maurizio, C., Mattei, G., Canton, P., Cattaruzza, E., de Julián Fernández, C., Mazzoldi, P., D'Acapito, F., Battaglin, G., Scain, C., Vomiero, A., Mat. Sci. Eng. C 27 (2007), 193. "Thermal evolution of cobalt nanocrystals embedded in silica"

Mehl, M. J., Papaconstantopoulos, D. A., Phys. Rev. B 54 (1996), 4519. "Applications of a tight-binding total-energy method for transition and noble metals: Elastic constants, vacancies and surfaces of monoatomic metals"

Menon, P.G., J. Mol. Catal. 59 (1990), 207. "Coke on catalysts - harmful, harmless, invisible and beneficial types"

Methfessel, M., Paxton, A.T., Phys. Rev. B 40 (1989), 3516. "High precision sampling for Brillouin-zone integration in metals"

Methfessel, M., Hennig, D., Scheffler, M., Phys. Rev. B 46 (1992), 4816. "Trends of the surface relaxations, surface energies and work functions of the 4d transition metals"

Methfessel, M., Paxton, A.T., Phys. Rev. B 40 (1989), 3516. "High precision sampling for Brillouin-zone integration in metals"

Michaelson, H.B., J. Appl. Phys. 48 (1977), 4729. "The work function of the elements and its periodicity"

Milman, V., Winkler, B., White, J. A., Pickard, C. J., Payne, M.C., Akhmatskaya, E. V., Nobes, R. H., Int. J. Quant. Chem. 77 (2000), 895. "Electronic structure, properties and phase stability of inorganic crystals: A pseudopotential plane-wave study"

Monkhorst, H.J. Pack, J.D., Phys. Rev. B 13 (1976), 5188. "Special points for Brillouin-zone integration"

Mott, N.F., Zinamon, Z., Rep. Prog. Phys. 33 (1970), 881. "The metal-nonmetal transition"

Moulijn, J.A., Van Diepen, A.E., Kapteijn, F., Appl. Catal. A: Gen. 212 (2001), 3. "Catalyst deactivation: Is it predictable? What to do?"

Nagashima, A., Tejima, N., Oshima, C., Phys. Rev. B 50 (1994), 17487. "Electronic structure of the pristine and alkali-metal-intercalated monolayer graphite/Ni(111) systems"

Nanda, K.K., Maisels, A., Kruis, F.E., Fissan, H., Stappert, S., Phys. Rev. Lett. 91 (2003), 16102. "Higher surface energy of free nanoparticles"

Noguera, C., J. Phys. Cond. Matt. 12 (2000), R367. "Polar oxide surfaces"

Oliver, P.M., Parker, S.C., Mackrodt, W.C., Mod. Simul. Mater. Sci. Eng. 1 (1993), 751. "Computer simulation of the crystal morphology of NiO"

Ooi, N., Rairkar, A., Adams, J.B., Carbon 44 (2006), 231. "Density Functional study of graphite bulk and surface properties"

Overbury, S.A., Bertrand, P.A., Somorjai, G.A., Chem. Rev. 75 (1975), 547. "The Surface Composition of Binary Systems. Prediction of Surface Phase Diagrams of Solid Solutions"

Parr, R.G., Yang, W., in "Density Functional Theory of Atoms and Molecules", Oxford Science Publications, 1989.

Perdew, J.P., Zunger, A., Phys. Rev. B 23 (1981), 5048. "Self-interaction corrections to density functional approximations for many-electron systems"

Perdew, J.P., Phys. Rev. B 33 (1986), 8822. "Density-functional approximation for the correlaction energy of the inhomogeneous electron gas"

Perdew, J.P., Chevary, J.A., Vosko, S.H., Jackson, K.A., Pederson, M.R., Singh, D.J., Fiolhais, C., Phys. Rev. B 46 (1992), 6671. "Atoms, molecules, solids and surfaces: Applications of the generalized gradient approximation for exchange and correlation"

Perdew, J.P., Burke, K., Ernzerhof, M., Phys. Rev. Lett. 77 (1996), 3865. "Generalized gradient approxiamation made simple"

Perdew, J.P., Kurth, S., Zupan, A., Blaha, P., Phys. Rev. Lett. 82 (1999), 2544. "Accurate Density Functional with correct formal properties: A step beyond the Generalized Gradient Approximation"

Perdew, J.P., Ruzsinszky, A., Tao, J., Staroverov, V.N., Scuseria, G.E., Csonka, G.I., J. Chem. Phys. 123 (2005), 062201. "Prescription for the design and selection of density functional approximations: More constraint satisfaction with fewer fits"

Phala, N.S., Van Steen, E., Gold Bulletin 40 (2007), 150. "Intrinsic reactivity of gold nanoparticles: Classical, semi-empirical and DFT studies"

Presland, A.E.B., Walker, P.L., Jr., Carbon 7 (1969), 1. "Growth of single-crystal graphite by pyrolysis of acetylene over metals"

Prutton, M., Walker, J.A., Welton-Cook, M.R., Felton, R.C., Ramsey, J.A., Surf. Sci. 89 (1979), 95. "LEED studies of the structures of the (100) sur-

faces of divalent metal oxides"

Ram, S., Mat. Sci. Eng. A 304-306 (2001), 923. "Allotropic phase transformations in HCP, FCC and BCC metastable structures in Co-nanoparticles"

Reddy, B.V., Khanna, S.N., Dunlap, B.I., Phys. Rev. Lett. 70 (1993), 3323. "Giant magnetic moments in 4d clusters"

Reuter, K., Scheffler, M., Phys. Rev. B 65 (2001), 035406. "Composition, structure, and stability of $RuO_2(110)$ as a function of oxygen pressure"

Riedel, T., Schulz, H., Schaub, G., Jun, K.-W., Hwang, J.-S., Lee, K.-W., Topics in Catal. 26 (2003), 41. "Fischer-Tropsch on iron with H_2/CO and H_2/CO_2 as synthesis gases: The episodes of formation of the Fischer-Tropsch regime and construction of the catalyst"

Robertson, I.J., Heine, V., Payne, M.C., Phys. Rev. Lett. 70 (1993), 1944. "Cohesion in aluminium systems: A first-principles assessment of "glue" schemes"

Rohrbach, A., Hafner, J., Kresse, G., J. Phys.: Cond. Matt. 15 (2003), 979. "Electronic correlation effects in transition-metal sulfides"

Rohrbach, A., Hafner, J., Kresse, G., Phys. Rev. B 69 (2004), 075413. "Molecular adsorption on the surface of strongly correlated transition-metal oxides: A case study for CO/NiO(100)"

Romanowski, W., Surf. Sci. 18 (1969), 373. "Equilibrium forms of very small metallic crystals"

Rosei, R., De Crescenzi, M., Sette, F., Quaresima, C., Savoia, A., Perfetti, P., Phys. Rev. B 28 (1983), 1161. "Structure of graphitic carbon on Ni(111): A surface extended-energy-loss fine-structure study"

Rosei, R., Modesti, S., Sette, F., Quaresima, C., Savoia, A., Perfetti, P., Phys. Rev. B 29 (1984), 3416. "Electronic structure of carbidic and graphitic carbon on Ni(111)"

Rosenfeld, G., Morgenstern, K., Esser, M., Comsa, G., Appl. Phys. A 69 (1999), 489. "Dynamics and stability of nanostructures on metal surfaces"

Rostrup-Nielsen, J., Trimm, D.L., J. Catal. 48 (1977), 155. "Mechanisms of carbon formation on nickel-containing catalysts"

Rostrup-Nielsen, J.R., J. Catal. 85 (1984), 31. "Sulfur-passivated nickel catalysts for carbon-free steam reforming of methane"

Rusanov, A.I., Surf. Sci. Rep. 23 (1996), 173. "Thermodynamics of solid surfaces"

Rusanov, A.I., Surf. Sci. Rep. 58 (2005), 111. "Surface thermodynamics revisited"

Rydberg, H., Lundqvist, B.I., Langreth, D.C., Dion, M., Phys. Rev. B 62 (2000), 6997. "Tractable nonlocal correlation density functionals for flat surfaces and slabs"

Rydberg, H., Dion, M., Jacobson, N., Scrö der, E., Hyldgaard, P., Simak, S.I., Langreth, D.C., Lundqvist, B.I., Phys. Rev. Lett. 91 (2003), 126402. "Van der Waals density functional for layered structures"

Dion, M., Rydberg, H., Schröder, E., Langreth , D.C., Lundqvist, B.I., Phys. Rev. Lett. 92 (2004), 246402. "Van der Waals density functional for general geometries"

Sanville, E., Kenny, S.D., Smith, R., Henkelman G., J. Comp. Chem. 28 (2007), 899. " Improved grid-based algorithm for Bader charge allocation"

Sasaki, S., Fujino, K., Takeuchi, Y., Proc. Japan Acad. 55 Ser. B (1979), 43. "X-ray determination of electron density distributions in oxides, MgO, MnO, CoO, and NiO, and atomic scattering factors of their constituent atoms"

Sato, H., Kitakami, O., Shimada, Y., Otani, Y., Fukamichi, K., J. Appl. Phys. 81 (1997), 1858. "Structure and magnetism of hcp-Co fine particles"

Sault, A.G., Datye, A.K., J. Catal. 140 (1993), 136. "An Auger electron spectroscopy study of the activation of iron Fischer-Tropsch catalysts"

Sawatzky, G.A., Allen, J.W., Phys. Rev. Lett. 53 (1984), 2339. "Magnitude and Origin of the Band Gap in NiO"

Schabel, M.C., Martins, J.L., Phys. Rev. B 46 (1992), 1785. "Energetics of interplanar binding in graphene"

Schanke, D., Hilmen, A.M., Bergene, E., Kinnari, K., Rytter, E., Ådanes, E., Holmen, A., Catal. Lett. 34 (1995), 269. "Study of the deactivation

mechanism of Al_2O_3-supported cobalt Fischer-Tropsch catalysis"

Schultz, H., Schaub, G., Claeys, M., Riedel, T., Appl. Catal. A: Gen. 186 (1999), 215. "Transient initial kinetic regimes of Fischer-Tropsch synthesis"

Schultz, H., Appl. Catal. A: Gen. 186 (1999), 3. "Short history and present trends of Fischer-Tropsch synthesis"

Schultz, H., Nie, Z., Ousmanov, F., Catalysis Today 71 (2002), 351. "Construction of the Fischer-Tropsch regime with cobalt catalysts"

Shelton, J.C., Patil, H.R., Blakely, J.M., Surf. Sci. 43 (1974), 493. "Equilibrium segregation of carbon to a Nickel (111) surface: A surface phase transition"

Sherman, J., Chem. Rev. 11 (1932), 93. "Crystal energies of ionic compounds and thermochemical applications"

Shi, F.G., J. Mater. Res. 9 (1994), 1307. "Size dependent thermal vibrations and melting in nanocrystals"

Shroff, M.D., Kalakkad, D., Coulter, K.E., Köhler, S.D., Harrington, M.S., Jackson, N.B., Sault, A.G., Datye, A.K., J. Catal. 156 (1995), 185. "Activation of precipitated iron Fischer-Tropsch synthesis catalysts"

Shull, C.G., Strauser, W.A., Wollan, E.O., Phys. Rev. 83 (1951), 333. "Neutron diffraction by paramagnetic and antiferromagnetic substances"

Skriver, H.L., Rosengaard, N.M., Phys. Rev. B 46 (1992), 7157. "Surface energy and work function of elemental metals"

Smart, J.S., Greenwald, S., Phys. Rev. 82 (1951), 113. "Crystal structure transitions in antiferromagnetic compounds at the Curie temperature"

Somorjai, G.A., Van Hove, M.A., Acta. Cryst. B51 (1995), 502. "Restructuring of metal surfaces and adsorbed monolayers during chemisorption and catalytic reaction"

Somorjai, G.A., Hwang, K.S., Parker, J.S., Topics in Catal. 26 (2003), 87. "Restructuring of hydrogenation metal catalysts under the influence of CO and H_2"

Souzu, Y., Tsukada, M., Surf. Sci., 326 (1995), 42. "Electronic states and scanning tunneling spectroscopy image of monolayer graphite on a nickel

(111) surface by the DV-X α method"

Spanjaard, D., Desjonquères, M.C., Phys. Rev. B 30 (1984), 4822. "Comment on universal features of bonding in metals"

Staroverov, V.N., Scuseria, G.E., Tao, J., Perdew, J.P., J. Chem. Phys. 119 (2003), 12129. "Comparative assessment of a new nonempirical density functional: Molecules and hydrogen-bonded complexes"

Stephens,P.J., Devlin, F.J., Chabalowski, C.F., Frisch, M.J., J. Phys. Chem. 98 (1994), 11623. "*Ab-Initio* calculation of vibrational adsorption and circular dichroism spectra using density functional force fields."

Steynberg, A.P., Espinoza, R.L., Jager, B., Vosloo, A.C., Appl. Catal. A: Gen. 186 (1999), 41. "High temperature Fischer-Tropsch synthesis in commercial practice"

Stroppa, A., Termentzidis, K., Paier, J., Kresse, G., Hafner, J., Phys. Rev. B 76 (2007), 195440. "CO adsorption on metal surfaces: A hybrid functional study with plane-wave basis set"

Sun, Q., Reuter, K., Scheffler, M., Phys. Rev. B 67 (2003), 205424. "Effect of a humid environment on the surface structure of RuO_2(110)"

Sung, S.-S., Hoffmann, R., J. Am. Chem. Soc. 107 (1985), 578. "How carbon monoxide bonds to metal surfaces"

Swart, J.C.W., Van Helden, P., Van Steen, E., J. Phys. Chem. C 111 (2007), 4998. "Surface Energy Estimation of Catalytically Relevant fcc Transition Metals Using DFT Calculations on Nanorods"

Szotek, Z., Temmerman, W.M., Winter, H., Phys. Rev. B 47 (1993), 4029. "Application of the self-interaction correction to transition-metal oxides"

Takahashi, T., Tokailin, H., Sagawa, T., Phys. Rev. B 32 (1985), 8317. "Angle resolved ultraviolet spectroscopy of the unoccupied band structure of graphite"

Tao, J., Perdew, J.P., Staroverov, V.N., Scuseria, G.E., Phys. Rev. Lett. 91 (2003), 146401. "Climbing the Density Functional ladder: Nonempirical metaGeneralized Gradient Approximation designed for molecules and solids"

Tao, J., Perdew, J.P., J. Chem. Phys. 122 (2005), 114102. "Test of a

nonempirical density functional: Short-range part of the Van der Waals interaction in rare-gas dimers"

Tasker, P.W., J. Phys. C Solid State Phys. 12 (1979), 4977. "The stability of ionic crystal surfaces"

Terakura, K., Oguchi, T., Williams, A.R., Kübler, J., Phys. Rev. B 30 (1984), 4734. "Band theory of insulating transition-metal monoxides: Band-structure calculations"

Terakura, K., Williams, A.R., Oguchi, T., Kübler, J., Phys. Rev. Lett. 52 (1984), 1830. "Transition-metal monoxides: Band or Mott insulators"

The Catalyst Review Newsletter, April 2005, 4. "Gas-to-Liquids: Peering into the Crystal Ball"

Tran, F., Blaha, P. Schwarz, K.,Novák, P., Phys. Rev. B 74 (2006), 155108. "Hybrid exchange-correlation energy functionals for strongly correlated electrons: Applications to transition-metal monoxides"

Twigg, M.V. Eds. "Catalyst Handbook", Second edition. Wolfe Pbulishing Ltd., 1989.

Tyson, W.R., Miller, W.A., Surf. Sci. 62 (1977), 267. "Surface free energies of solid metals: Estimation from liquid surface tension measurements"

Van Berge, P.J., Everson, R.C., Stud. Surf. Sci. Catal. 107 (1997), 207. "Cobalt as an alternative Fischer-Tropsch catalyst to iron for the production of middle distillates."

Van Berge, P.J., Van de Loosdrecht, J., Barradas, S., Van der Kraan, A.M., Catal. Today 58 (2000), 321. "Oxidation of cobalt based Fischer-Tropsch catalysts as a deactivation mechanism"

Van de Loosdrecht, J., Balzhinimaev, B., Dalmon, J.-A., Niemantsverdriet, J.W., Tsybulya, S.V., Saib, A.M., Van Berge, P.J., Visagie, J.L., Catal. Today 123 (2007), 293. "Cobalt Fischer-Tropsch synthesis: Deactivation by oxidation?"

Van Elp, J., Wieland, J.L., Eskes, H., Kuiper, P., Sawatzky, G.A., de Groot, F.M.F., Turner, T.S., Phys. Rev. B 44 (1991), 6090. "Electronic structure of CoO, Li doped CoO and $LiCoO_2$"

Van Laar, B., Phys. Rev. 138 (1965), A584. "Multi-spin-axis for CoO"

Van Steen, E., Claeys, M., Dry, M.E., Van de Loosdrecht, J., Viljoen, E.L., Visagie, J.L., J. Phys. Chem. B 109 (2005), 3575. "Stability of nanocrystals: Thermodynamic analysis of oxidation and re-reduction of cobalt in water/hydrogen mixtures"

Vanderbilt, D., Phys. Rev. B 41 (1990), 7892. "Soft self-consistent pseudopotentials in a generalized eigenvalue formalism"

Van Hardeveld, R., Hartog, F., Surf. Sci. 15 (1969), 189. "The statistics of surface atoms and surface sites on metal crystals"

Vannice, M.A., J. Catal. 37 (1975), 449. "The catalytic synthesis of hydrocarbons from H_2/CO mixtures over the group VIII metals: I. Specific activities and product distributions of supported metals"

Van Santen, R.A., Neurock, M., in "Molecular Heterogeneous Catalysis", Wiley-VCH Verlag GmbH & Co. KGaA, Weinheim, 2006.

Varma, C.M., Wilson, A.J., Phys. Rev. B 22 (1980), 3795. "Systematics of the binding energy of oxygen and hydrogen on transition metal surfaces"

Vitos, L., Ruban, A.V., Skriver, H.L., Kollár, J., Surf. Sci. 411 (1998), 186. "The surface energy of metals"

Vosko, S.H., Wilk, L., Nusair, M., Can. J. Phys. 58 (1980), 1200. "Accurate spin-dependent electron liquid correlation energies for local spin density calculations: A critical analysis"

Vydrov, O.A., Scuseria, G.E., Perdew, J.P., Ruzsinszky, A., Csonka, G.I., J. Phys. Chem. 124 (2006), 094108. "Scaling down the Perdew-Zunger self interaction correction in many electron regions"

Wang, X.-G., Weiss, W., Shaikhutdinov, Sh.K., Ritter, M., Petersen, M., Wagner, F., Schögl, R., Scheffler, M., Phys. Rev. Lett. 81 (1998), 1038. "The hematite (α-Fe_2O_3) (0001) surface: Evidence for domains of distinct chemistry"

Wang, S.G., Tian, E.K., Lung, C.W., J. Phys. Chem. Solids 61 (2000), 1295. "Surface energy of arbitrary crystal plane of bcc and fcc metals"

Wang, X.-G., Chaka, A., Scheffler, M., Phys. Rev. Lett., 84 (2000), 3650. "Effect of the environment on α-Al_2O_3(0001)"

Wang, L., Maxisch,T., Ceder, G., Phys. Rev. B 73 (2006), 195107. "Oxidation energies of transition metal oxides within the GGA+U framework"

Wang, S.G., Liao, X.Y., Cau, C.B., Li. Y.W., Wang, J., Jiao, H., J. Phys. Chem. 111 (2007), 10894. "Formation of carbon species on Ni(111): Structure and stability"

Weller, S., J. Am. Chem. Soc. 69 (1947), 2432. "Kinetics of carbiding and hydrocarbon synthesis with cobalt Fischer-Tropsch catalysts"

Weller, S., Hofer, L.J.E., Anderson, A.B., J. Am. Chem. Soc. 70 (1948), 799. "The role of bulk cobalt carbide in the Fischer-Tropsch Synthesis"

West, A. R., "Basic Solid State Chemistry", 2nd ed., Wiley & Sons Ltd., New York, 1999.

Williams, F.J., Malikova, N., Lambert, R.M., Catal. Lett. 90 (2003), 177. "An AFM study of the genesis and sintering in hydrogen of a realistic Cu/amporphous silica planar model catalyst"

Wilson, J., de Groot, C., J. Phys. Chem. 99 (1995), 7860. "Atomic-scale restructuring in high-pressure catalysis"

Wodiunig, S., Keel, J.M., Wilson, T.S.E., Zemichael, F.W., Lambert, R.M., Catal. Lett. 87 (2003), 1. "AFM and XPS study of the sintering of realistic Ag/{0001}α-Al_2O_3 model catalysts under conditions of ethene epoxidation"

Wood, D.M., Phys. Rev. Lett. 46 (1981), 749. "Classical size dependence of the work function of small metallic spheres"

Wu, M.C., Xu, Q., Goodman, D.W., J. Phys. Chem. 98 (1994), 5104. "Investigations of graphitic overlayers formed from methane decomposition on Ru(0001) and Ru(11$\bar{2}$0) catalysts with scanning tunneling microscopy and high-resolution electron energy loss spectroscopy"

Wu. Q., Yang, W., J. Chem. Phys. 116 (2002), 515. "Empirical correction to density functional theory for Van der Waals interactions"

Wynblatt, P., Ahn, T-A., p. 83 "Crystallite Sintering and Growth in Supported Catalysts" in Materials Science Research, Volume 10, "Sintering and Catalysis", Kuczynski, G.C., ed., Plenum Press, 1975.

Xu, L., Xiao, H.Y., Zu, X.T., Chem. Phys. Lett. 315 (2005), 155. "Hydrogen adsorption on Ru(0001) surface from density-functional periodic calculations"

José-Yacamán, M., Gutierez-Wing, C., Miki, M., Yang, D.-Q., Piyakis, K.N., Sacher, E., J. Phys. Chem. B 109 (2005), 9703. "Surface diffusion and coalescence of mobile metal nanoparticles"

Yan, Z., Perdew, J.P., Kurth, S., Phys. Rev. B 61 (2000), 16430. "Density functional for short-range correlation: Accuracy of the random-phase approximation for isoelectronic energy changes"

Yang, D.-Q., Sacher, E., J. Appl. Phys. 90 (2001), 4768. "Coalescence kinetics of copper clusters on highly oriented pyrolytic graphite and Dow Cyclotene, as determined by x-ray photoelectron spectroscopy"

Yang, D.-Q., Sacher, E., Surf. Sci. 516 (2002), 43. "Ar^+-induced surface defects on HOPG and their effect on the nucleation, coalescence and growth of evaporated copper."

Yates, I.C., Satterfield, C.N., Energy & Fuels 5 (1991), 168. "Intrinsic kinetics of the Fischer-Tropsch Synthesis on a cobalt catalyst"

Yoshizawa, K., Kato, T., Yamabe, T., J. Chem. Phys. 105 (1996), 2099. "Interlayer interactions in two-dimensional systems: Second-order effects causing ABAB stacking of layers in graphite"

Yoshizawa, K., Yumura, T., Yamabe, T., Bandow, S., J. Am. Chem. Soc. 122 (2000), 11871. "The role of orbital interactions in determining the interlayer spacing in graphite slabs"

Zaanen, J., Sawatzky, G.A., Allen, J.W., Phys. Rev. Lett. 55 (1985), 418. "Band gaps and electronic structure of transition-metal compounds"

Zacharia, R, Ulbricht, H., Hertel, T., Phys. Rev. B 69 (2004), 155406. "Interlayer coohesive energy of graphite from thermal desorption of polyaromatic hydrocarbons"

Zhang, Y., Yang, W., Phys. Rev. Lett. 80 (1998), 890. Comment on "Generalized gradient approximation made simple"

Zhao, J-C., Notis, M.R., Scripta Metall. Mater. 32 (1995), 1671. "Kinetics of the FCC to HCP phase transformation and the formation of martensite in pure cobalt"

Zheng, C., Apeloig, Y., Hoffmann, R., J. Am. Chem. Soc. 110 (1988), 749. "Bonding and coupling of C1 fragments on metal surfaces"